

**ANALYSIS OF THE FORMABILITY OF METALS**

**A THESIS SUBMITTED TO  
THE GRADUATE SCHOOL OF NATURAL AND APPLIED SCIENCES  
OF  
THE MIDDLE EAST TECHNICAL UNIVERSITY**

**BY**

**ÖZGÜR KOÇAK**

**IN PARTIAL FULFILLMENT OF THE REQUIREMENTS FOR THE DEGREE OF  
MASTER OF SCIENCE  
IN  
THE DEPARTMENT OF MECHANICAL ENGINEERING**

**JULY 2003**

Approval of the Graduate School of Natural and Applied Sciences.

---

Prof. Dr. Canan ÖZGEN  
Director

I certify that this thesis satisfies all the requirements as a thesis for the degree of Master of Science.

---

Prof. Dr. Eres SÖYLEMEZ  
Head of the Department

This is to certify that we have read this thesis and that in our opinion it is fully adequate, in scope and quality, as a thesis for the degree of Master of Science.

---

Prof. Dr. A. Erman TEKKAYA  
Supervisor

Examining Committee in Charge:

Prof. Dr. Ö. Gündüz Bilir (Chairperson)

---

Prof. Dr. A. Erman TEKKAYA (Supervisor)

---

Assoc. Prof. Dr. Suat KADIOĞLU

---

Dipl.-Ing. Achim RUF

---

Assoc. Prof. Dr. C. Hakan GÜR

---

## ABSTRACT

### ANALYSIS OF FORMABILITY OF METALS

Koçak, Özgür

M.S., Department of Mechanical Engineering

Supervisor: Prof. Dr.-Ing. A. Erman Tekkaya

July 2003, 153 pages

Workpieces during cold forging fail basically due to ductile fracture. Ductile fracture can be predicted by damage models. In this study, various damage models such as Cockcroft & Latham, McClintock, Freudenthal, Rice & Tracy, Oyane, Ayada, Brozzo are investigated for their applicability to three workpiece materials: bearing steel (100Cr6), stainless steel (X5CrNiMo1810) and brass (CuZn39). The damage material parameters have been obtained by various tests such as tensile, standard compression, ring compression, compression with flanges and conical compression tests. The characterization has been assisted by finite element simulation of the various tests. It has been shown that the available damage models can predict the location of failure satisfactorily but are no able to predict the onset of failure quantitatively.

Keywords: Formability Limit, Failure Criteria, Cold Forming, Surface Cracks, Finite Element Analysis

## ÖZ

### METALLERİN ŞEKİLLENDİRİLEBİLME ANALİZLERİ

Koçak, Özgür

Yüksek Lisans, Makina Mühendisliği Bölümü

Tez Yöneticisi: Prof. Dr. A. Erman Tekkaya

Temmuz 2003, 153 sayfa

Soğuk şekillendirilen malzemelerde oluşan kusurlardaki temel neden sünek kırılmalardır. Sünek kırılmalar hasar modelleri ile tahmin edilebilir. Bu çalışmada Cockcroft & Latham, McClintock, Freudenthal, Rice & Tracy, Oyane, Ayada, Brozzo modelleri gibi çeşitli modellerin rulman çeliği (100Cr6), paslanmaz çelik (X5CrNiMo1810) ve pirinçten (CuZn39) oluşan toplam üç malzemeye uygulanabilirliği araştırılmıştır. Malzeme hasar parametrelerinin elde edilmesinde çekme, standart basma, halka basma, flanşlı parça basma ve konik parça basma testleri kullanılmıştır. Bu testlerin incelenmesinde sonlu elemanlar yöntemiyle yapılan simulasyonlardan yararlanılmıştır. Mevcut hasar modellerinin malzemedeki kusur yerlerini tesbit edebildiği, ancak kusur başlangıcını sayısal anlamda tespit edemediği gösterilmiştir.

Anahtar Kelimeler: Şekillendirilebilme Limiti, Kusur Kriterleri, Soğuk Dövme, Yüzey Çatlakları, Sonlu Eleman Analizleri

## ACKNOWLEDGEMENT

I would like to express my deepest gratitude and appreciation to my supervisor Prof. Tekkaya who inspired, encouraged and supported me at all levels of this study.

I would like to thank to my colleague Bahadır Koçaker, whose friendship, support and suggestions made great contributions to this work.

This study was carried out at METU and also at company HILTI as a cooperative research project. The support provided by HILTI is greatly acknowledged. I am very grateful to Achim Ruf and Günter Domani for their support to organize the tests in HILTI, and their suggestions to the study. Also I would like to thank to ORS Bearing Company (Ankara) for their support.

I would like to thank to Prof. Dr. Bilgehan Ögel from METU Metallurgical Engineering Department for his help and suggestions. I sincerely thank to the technicians of METU Mechanical Engineering Department, especially to Saim Seloğlu, Necati Güner, Yusuf Papur, Yılmaz Öztürk, Muhlis Baharlı for their help in manufacturing of test specimens and applications of tests.

I send my best wishes to previous and current Femlab members Muhsin Öcal, Mete Egemen, Ahmet Kurt, Kürşad Kayatürk, Ömer Music, Özgür Ekici, Bülent Yavuz, Celalettin Karadoğan, Halil Bil, Oya Okman, Murat Özmen, Erge Koray, Nagihan Topçu, Canderim Önder, İsmail Erkan Önder, Çağrı Kaya and Çağlar Sönmez.

I want to thank to Kerem Önal, Serdar Dünder, Gökhan Ceylan, Serdar İnce, Emre Güriş, Bora Yeşiltepe and also to Viktoria and the members of METU Couple Dances Club, who have always injected happiness and excitement to my life.

The greatest thanks go to my family members for their infinite support.

## TABLE OF CONTENTS

ABSTRACT.....	iii
ÖZ.....	iv
ACKNOWLEDGEMENT.....	v
TABLE OF CONTENTS.....	vi
LIST OF TABLES.....	viii
LIST OF FIGURES.....	x
CHAPTER	
1 INTRODUCTION.....	1
1.1 Necessity for Formability Analysis.....	1
1.2 Failure Criteria and Their Generalization Problems.....	3
1.3 Aim and Scope of the Thesis.....	3
2 LITERATURE SURVEY.....	5
2.1 Introduction.....	5
2.2 Bulk Metal Forming Defects.....	5
2.2.1 Type of Defects.....	5
2.2.2 Effecting Factors.....	7
2.2.3 Brittle and Ductile Fractures.....	8
2.3 Criteria for Formability Analysis.....	9
2.3.1 Damage Criteria using Empirical and Semiempirical Models.....	10
2.3.2 Damage Criteria using Theoretical Void Coalescence and Growth.....	12
2.3.3 Damage Criteria in FEM Applications.....	20
2.4 Obtaining Material Flow Curves.....	21
2.4.1 Tension Test.....	21
2.4.2 Compression Test.....	26
2.5 Friction Analysis.....	30
2.5.1 Friction Models in Metal Forming.....	31
2.5.1.1 Coulomb (Amonton) Friction Model.....	31
2.5.1.2 Shear Friction Model.....	32
2.5.2 Effect of Friction on Formability.....	33
2.5.3 Ring Compression Test.....	33
3 FORMABILITY ANALYSIS OF BEARING STEEL 100Cr6.....	36
3.1 Introduction.....	36
3.2 Obtaining Material Flow Curves.....	36
3.2.1 Tension Flow Curve.....	38
3.2.2 Compression Flow Curve.....	41
3.3 Performed Failure Experiments.....	47
3.3.1 Tensile Test.....	47

3.3.2	Various Compression Tests.....	49
3.4	Modeling of Experiments.....	53
3.4.1	Friction Factor Prediction.....	55
3.4.2	Failure Experiments.....	58
3.4.2.1	Tension Test Modeling.....	59
3.4.2.2	Compression Test Modeling.....	61
3.4.3	Stress Paths for Critical Regions.....	66
3.5	Discussions and Conclusions.....	69
4	FORMABILITY ANALYSIS OF STAINLESS STEEL X5 CrNiMo1810.....	70
4.1	Introduction.....	70
4.2	Obtaining Material Flow Curves.....	70
4.2.1	Tension Flow Curve.....	70
4.2.2	Compression Flow Curve.....	73
4.3	Performed Failure Experiments.....	76
4.3.1	Tensile Test.....	76
4.3.2	Various Compression Tests.....	77
4.4	Modeling of Experiments.....	82
4.4.1	Friction Factor Prediction.....	85
4.4.2	Failure Experiments.....	90
4.4.2.1	Tension Test Modeling.....	90
4.4.2.2	Compression Test Modeling.....	91
4.4.3	An Industrial Case Study.....	100
4.5	Discussions and Conclusions.....	102
5	FORMABILITY ANALYSIS OF BRASS.....	104
5.1	Introduction.....	104
5.2	Obtaining Material Flow Curves.....	104
5.2.1	Tension Flow Curve.....	104
5.2.2	Compression Flow Curve.....	108
5.3	Performed Failure Experiments.....	113
5.3.1	Tensile Test.....	114
5.3.2	Various Compression Tests.....	115
5.4	Modeling of Experiments.....	118
5.4.1	Friction Factor Prediction.....	120
5.4.2	Failure Experiments.....	122
5.4.2.1	Tension Test Modeling.....	123
5.4.2.2	Compression Test Modeling.....	124
5.4.3	Stress Paths for Critical Regions.....	130
5.5	Discussions and Conclusions.....	135
6	DISCUSSIONS AND CONCLUSIONS.....	137
7	FURTHER RECOMMENDATIONS.....	145
	REFERENCES.....	147
	APPENDIX A.....	150

## LIST OF TABLES

TABLE	
3.1 Dimensions of tension test specimens in mm.....	48
3.2 Dimensions of standard compression specimens in mm.....	50
3.3 Dimensions of flanged specimens in mm.....	52
3.4 Dimensions of ring specimens in mm.....	53
3.5 Parameters used in FEM simulations .....	54
3.6 Dimensions of ring test specimens in mm.....	55
3.7 Various criteria and their critical values, which become maximum at the center of fracture diameter.....	61
3.8 Various criteria and their critical values at crack regions.....	62
3.9 Various criteria and their critical values at crack regions.....	63
3.10 Various criteria and their critical values at crack regions.....	64
4.1 Dimensions of tension test specimens in mm.....	77
4.2 Dimensions of standard compression specimens in mm.....	79
4.3 Dimensions of flanged specimens in mm.....	79
4.4 Dimensions of ring specimens in mm.....	80
4.5 Dimensions of tapered specimens in mm.....	81
4.6 Parameters used in FEM simulations .....	84
4.7 Dimensions of ring test specimens in mm.....	85
4.8 Various criteria and their critical values, which become maximum at the center of fracture diameter.....	91
4.9 Various criteria and their critical values at critical regions of given standard compression specimens.....	93
4.10 Various criteria and their critical values at critical regions of given flanged specimens.....	94
4.11 Various criteria and their critical values at critical regions of given ring specimens.....	96

4.12 Various criteria and their critical values at critical regions of given tapered specimens.....	97
4.13 Various criteria and their critical values at crack regions.....	100
5.1 Dimensions of tension test specimens in mm.....	114
5.2 Dimensions of standard compression specimens in mm.....	115
5.3 Dimensions of flanged specimens in mm.....	116
5.4 Dimensions of ring specimens in mm.....	117
5.5 Parameters used in FEM simulations .....	119
5.6 Dimensions of ring test specimens in mm.....	120
5.7 Various criteria and their critical values, which become maximum at the center of fracture diameter.....	123
5.8 Various criteria and their critical values at crack regions of given standard compression specimens.....	124
5.9 Various criteria and their critical values at crack regions of given flanged specimens.....	127
5.10 Various criteria and their critical values at crack regions of given ring specimens.....	128
6.1 Average critical damage values of material 100Cr6.....	140
6.2 Critical damage values of stainless steel.....	142
6.3 Critical damage values of brass flanged specimens.....	143
A.1 Cockcroft & Latham damage values and maximum punch force at the simulated compressions (to final height of 2mm) of stainless steel tapered specimens at various initial dimensions.....	150
A.2 Brozzo damage values and maximum punch force at the simulated compressions (to final height of 2mm) of stainless steel tapered specimens at various initial dimensions (Deform 2D version 7.1).....	151
A.3 Freudenthal damage values and maximum punch force at the simulated compressions (to final height of 2mm) of stainless steel tapered specimens at various initial dimensions (Deform 2D version 7.1).....	152

## LIST OF FIGURES

FIGURE	
2.1 a) Free surface crack b) crack originating from the die / workpiece interface during heading process c) chevron type internal crack.....	7
2.2 Fractured tension specimens made of two different materials .....	8
2.3 Damaged RVE in a damaged body (J. Lemaitre,1996).....	13
2.4 Damaged RVE in a damaged body (J. Lemaitre, 1996).....	14
2.5 Tension test specimen and related dimensions .....	22
2.6 Schematic representation of $a$ and $R$ values.....	25
2.7 Schematic representation of compression test without any friction (Koçaker, 2003) .....	26
2.8 Variation of sliding-contact shear stress with normal contact stress (Avitzur, 1983) .....	32
2.9 Effect of friction magnitude on metal flow during the ring compression test (H.Sofuoglu, 1999).....	34
2.10 Friction calibration curves in terms of $\mu$ .....	35
3.1 Tension test specimen and related dimensions .....	37
3.2 Tension test load-stroke curve.....	37
3.3 Stress and strain curve of material 100Cr6 obtained from tension test.....	38
3.4 Tensile flow curve of 100Cr6.....	39
3.5 Determination of $n$ and $K$ from the log-log plot of tensile flow curve.....	40
3.6 Extrapolated tension 100Cr6 flow curve.....	41
3.7 Load-stroke curve of 100Cr6 obtained from standard compression test....	42
3.8 Stress and strain curve of 100Cr6 obtained from standard compression test.....	43
3.9 Experimental flow curve of 100Cr6 obtained from standard compression test and smooth power curve fit to it.....	43
3.10 Application of iterative FEM (correction factor) method for first, second and third iterations.....	44

3.11 Determination of n and K from the log-log plot of compressive flow curve.....	45
3.12 Experimental compression flow curve and corrected & extrapolated final compression flow curve.....	46
3.13 Extrapolated flow curves of 100 Cr6 obtained from tension and compression tests.....	47
3.14 Tension test specimens and related dimensions.....	48
3.15 Compression test specimens .....	49
3.16 Designations for dimensions of a standard compression test specimen...	50
3.17 Free surface crack examples from experiments.....	51
3.18 Designations for dimensions of a flanged test specimen.....	51
3.19 Designations for dimensions of a ring test specimen.....	52
3.20 Calibration curves by using experimental flow curve.....	56
3.21 Calibration curves by using corrected flow curve.....	58
3.22 Modeled part of tension test specimen.....	59
3.23 Representative mesh and critical damage region.....	59
3.24 Cockroft-Latham damage distribution at the middle section of gage length.....	60
3.25 Modeled parts of specimens.....	61
3.26 Critical damage region for standard compression.....	62
3.27 Critical damage region for flange specimen.....	63
3.28 Critical damage region for ring specimen.....	64
3.29 Oyane criterion constant and critical value calculation.....	65
3.30 Application for Oyane damage criteria.....	66
3.31 $\sigma_1$ vs. $\sigma_2$ stress path for critical points.....	67
3.32 $\sigma_m$ vs. $\sigma_2$ stress path for critical points.....	68
4. 1 Stainless steel tension test specimens.....	71
4.2 Stress and strain curve of stainless steel obtained from tension test (Koçaker, 2003).....	71
4.3 Extrapolation for tension flow curve (Koçaker, 2003).....	72
4.4 Stress and strain curve of stainless steel from standard compression test	

(Koçaker, 2003).....	73
4.5 Application of iterative FEM (correction factor) method for first and second iterations (Koçaker, 2003).....	74
4.6 Extrapolated flow curves of stainless steel obtained from tension and compression tests (Koçaker, 2003).....	75
4.7 Stainless steel specimen geometries used in compression tests and examples of compressed specimens having no visible cracks.....	78
4.8 Designations for dimensions of a tapered specimen.....	81
4.9 Convergence study (w.r.t. element number) in flanged specimen models ..	82
4.10 Convergence study (w.r.t. element number) in ring specimen models ....	83
4.11 Convergence study (w.r.t. element number) in tapered specimen models	83
4.12 Ring compression specimens used for friction factor estimation in lubricant-free compressions.....	86
4.13 Calibration curves for Table 4.6 specimens by using corrected flow curve.....	87
4.14 Ring compression specimens used for friction factor estimation in lubricated compressions on the Zwick press .....	88
4.15 Calibration curves by using experimental flow curve.....	89
4.16 Calibration curves by using corrected flow curve.....	90
4.17 Critical damage region for tapered specimen (Deform 2D Version 7.1)..	92
4.18 Effect of flanged specimen dimensions on damage values of Brozzo criterion.....	95
4.19 The effect of flanged specimen dimensions on damage values of Cockroft&Latham criterion.....	95
4.20 Preparation of a flanged specimen from the necked region of a drawn tensile test specimen.....	98
4.21 Brozzo damage for the compression of flanged and ring specimens from necked region.....	99
4.22 Cracked material in a heading process (HILTI Corp., Liechtenstein).....	100
4.23 Modeling of heading process (Deform 2D Version 7.1).....	103
5. 1 Tension test specimen, gripped by the press .....	105

5.2 Stress and strain curve of brass obtained from tension test.....	106
5.3 Determination of n and K from log-log plot of tension flow data.....	107
5.4 Extrapolation for tension flow curve.....	108
5.5 Stress and strain curve of brass from standard compression test.....	109
5.6 Experimental flow curve of brass from standard compression test and smooth polynomial curve fit to it.....	110
5.7 Application of iterative FEM (correction factor) method for first and second iterations.....	111
5.8 Determination of n and K from the log-log plot of compressive flow curve.....	112
5.9 Extrapolated flow curves of brass obtained from tension and compression tests.....	113
5.10 Free surface crack examples from experiments.....	118
5.11 Calibration curves by using experimental flow curve.....	121
5.12 Calibration curves by using corrected flow curve.....	122
5.13 Standard compression specimens deviations.....	126
5.14 Flanged specimens deviations.....	127
5.15 Oyane criterion constant and critical value calculation.....	129
5.16 Application for Oyane damage criteria.....	130
5.17 $\sigma_1$ vs. $\sigma_2$ stress path for critical points.....	131
5.18 $\sigma_m$ vs. $\sigma_2$ stress path for critical points.....	132
5.19 Designations of certain dimensions to be used in Figures 5.20, 5.21 .....	133
5.20 Maximum shear stress analysis for the ‘standard compression 6’ specimen.....	134
5.21 Maximum shear stress analysis for the ‘Ring 3’ specimen.....	134
5.22 Maximum shear stress analysis for the ‘Flanged 5’ specimen.....	135
6.1 Repeatability of damage values among specimens of different geometries	139
6.2 Comparison between 100Cr6 and stainless steel critical damage values..	141
7.1 An example for the geometry of punch that may increase damage.....	146
A.1 Designations of tapered specimen used in the parameter study represented in Tables A.1, A.2, A.3.....	153

# CHAPTER 1

## INTRODUCTION

### 1.1 Necessity for Formability Analysis

Metal forming is a group of manufacturing methods by which the given form of a workpiece is plastically converted to another form without any change in the mass or the composition of the workpiece.

In metal forming processes, large plastic deformations are achieved. Metal forming processes achieve shape changes by either plastic deformation or a combination of plastic deformation and cracking. Examples of the first category are extrusion, drawing, rolling, and forging, and the examples of processes involving cracking are blanking and shearing (Abdel-Rahman, 1993).

One of the most severe restrictions of metal forming (especially cold metal forming) is limited plasticity of the material. Defects are common in the material due to the extensive deformation. Therefore fracture must be avoided (except for the processes requiring cracking as blanking and shearing), as the process is desired to be successful. However, in the design of new components, defects are common and these defects disappear as the process is optimized.

Solution of these problems is normally dependent on the experience and trial-and-error procedures of the die designer, but such empirical approaches are time consuming and rarely lead to generalization that would aid solution of future defect

problems. An engineering approach based on principles of metal forming is clearly needed (N.N., 1996).

Formability (workability) is investigating the limits of a material under forming without the occurrence of a ductile fracture or any other defect in a forming process. Formability criteria are required for the estimation of workability of the metals without expensive trials.

The ability to predict ductile failure leads to the reduction of failure in existing metal forming processes, provide the full utilization of materials in forming operations and allows for early modification of the production process.

The knowledge on critical damage value in a workpiece can be used in two ways:

1. Evaluating alternatives in process design:

For a process in which the material is known to fracture, or in analyzing a process where ductile fracture is known to be a risk, several alternatives can be analyzed. The alternative with the lowest critical damage value, obtained from a single or various fracture criteria, is the best alternative for minimizing the initiation of fracture.

2. Comparing a design to a known critical value of damage:

Critical damage values, created by a process in a workpiece, can be estimated from prior experience with a given material on a part that is known to fracture. Analyzing a process known to cause cracking in the part will give an upper bound value. And analyzing a part made of the same material that is known not to crack will give a lower bound value. If the peak damage value from the analysis corresponds with the fracture point on the part, this will give a good estimate of the critical value. Designs with a damage value below this value (10% to 20% or more) should be safe

from fracture, if material and annealing conditions are the same (Deform Users Manual, 2000).

## **1.2 Failure Criteria and Their Generalization Problems**

Workability depends on the ductility of the material being worked and also stress, strain-rate and temperature distributions in the workpiece. In turn, these factors are dependent on process variables such as the geometry of the tooling and the workpiece as well as the lubrication.

On the other hand, orientation, shape, and volume fraction of inclusions and other inhomogeneities have a dominant effect on the fracture process.

There are a number of damage criteria in the literature, which will be introduced in Chapter 2. The basic idea of many ductile fracture criteria is that fracture occurs when the value of a damage parameter reaches a critical value. However, no general theoretical means of ductile fracture criteria exists. The critical damage values, which can be defined as the total accumulated damage until failure at a critical point of the material, differs according to the process and material used. There are no generally suggested values for materials and the conditions requiring the usage of certain criteria do not appear in literature.

Difficulties arise in attempting to establish generalized deformation limits of materials, since the void nucleation (the starting point of crack formation) and growth depend on stress and strain history; the process is usually path-dependent.

## **1.3 Aim and Scope of the Thesis**

The aim of the study is to investigate the applicability of various failure criteria to predict damage in cold forging of various metals.

The investigated materials are bearing steel 100Cr6, stainless steel X5CrNiMo1810 and brass CuZn39.

Following damage criteria are analyzed: Cockcroft & Latham, McClintock, Freudenthal, Rice & Tracy, Oyane, Ayada, Brozzo, maximum effective stress / ultimate tensile strength.

The characterization of the damage material parameters is done by means of the standard compression, ring compression, compression with flanges and conical compression tests. Failure limits will be searched by these experiments where specimens of different geometries will be compressed on hydraulic presses at room temperature. Compression of the specimen is stopped when a surface crack initiation is visible, since the propagation of cracks is of little interest.

The deformation process during these tests is modeled by Finite Element Method (FEM). For this purpose, tensile and compressive flow curves of the materials are obtained experimentally and the certain corrections are done on the experimental flow curves. Friction conditions at the experimental media are determined by the ring tests initially.

The thesis report can be divided into mainly seven overwhelming chapters: After this chapter, the upcoming chapter will be about the previous studies known in the literature in this area, which can give an insight about the defects, damage criteria, determination of material flow curves and friction. Chapters 3, 4 and 5 are dedicated to the analysis of the formability of bearing steel, stainless steel and brass, respectively. Chapter 6 is for the representation of general discussions and conclusions about the study and finally, in Chapter 7 further recommendations are suggested.

## **CHAPTER 2**

### **LITERATURE SURVEY**

#### **2.1 Introduction**

In this chapter the previous literature related to the current study will be discussed. First, the defects that may be seen in metal forming processes will be introduced. Then the criteria for formability analysis and methods to obtain material flow curves will be explained. The literature survey will then conclude with the discussions on friction.

#### **2.2 Bulk Metal Forming Defects**

A defect occurs when the properties of a component do not conform to the design specifications.

In the forth-coming sections, types of defects in bulk metal forming will be introduced, factors that effect the formation of defects will be explained and the differences between ductile and brittle fractures will be given.

##### **2.2.1 Types of Defects**

Defects in cold forging products can be classified in six groups. These are folds, shear defects, cracks, surface defects, form defects and structural defects. Each group is divided into several sub-groups (Arentoft, 1995).

Folds are defined as forging defects with the appearance of material contact without fusion between the surface material and internal or surface material.

Shear defect is characterized by a localization of deformation into some narrow shear band without any fracture. Later in the process, these shear bands can turn into a crack initiated by a shear defect. Some typical shear defects appear when the material flows by passing a dead-zone, as in the formation of internal shear defect when upsetting a cylindrical workpiece under high friction conditions.

Surface defects include defects, which influence the properties of the surface. They don't have to result in useless components but they influence the tool life or require some machining. Orange peel defect is an example for this type of defects.

Form defects include mainly large geometrical defects such as incomplete filling of die cavity or misaligned components. Another example of this defect could be too large components caused by wear of the tool.

Structural defects are related to the material. Poor mechanical properties and poor formability characteristics are examples for this group.

Cracks, tears and bursts are defined as local macroscopic fractures, that can be divided into three groups for bulk forming operations: free surface cracks, cracks originating from the die-workpiece interface and internal cracks (Figure 2.1).

The free surface region experiences bi-axial state of stress while the other regions experience tri-axial state of stress. The advantage of dividing the cracks according to the position of the cracks can also be utilized when equipment for identifying these defects has to be chosen; since the methods for all surface cracks will be mainly optical, whereas the methods for internal cracks detection have to be more advanced. Devedzic (1986) had made a similar classification including the defects of sheet metals and failure of dies.

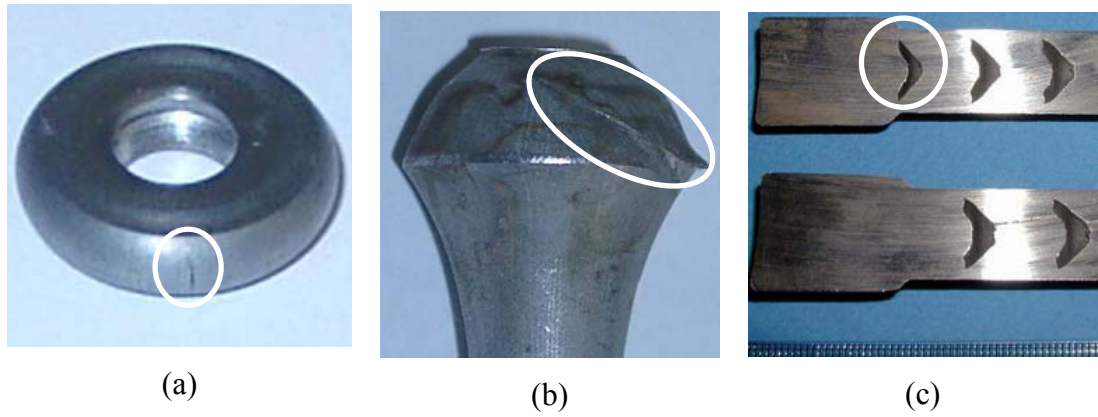


**Figure 2.1** a) Free surface crack b) crack originating from the die/workpiece interface during heading process c) chevron type internal crack

The scope of current study covers analysis mainly on free surface cracks.

### 2.2.2 Effecting Factors

The material plays an obvious role in determining workability, as orientation, shape, and volume fraction of inclusions and other inhomogeneities have a dominant effect on the fracture process. On the other hand, the process is an equally important factor. Workability depends on stress, strain rate and temperature distribution in the workpiece (Abdel-Rahman, 1993).

Deviatoric stresses are responsible for the shape change in the workpiece, while the hydrostatic stress influences the material ductility or formability. A high hydrostatic pressure increases material ductility by suppression of void nucleation and growth and conversely a tensile hydrostatic stress promotes material fracture.

Therefore, stress paths followed by each point of the material are important in crack analysis and these paths are dependent on process variables such as the geometry of the tooling and the workpiece, as well as lubrication.

### 2.2.3 Brittle and Ductile Fractures

The terms ductile and brittle are used to indicate the elongation at fracture. The quantities as the elongation at fracture and the presence of necking indicate whether the material is ductile or brittle. A difficulty here is to decide how much ductility is required to place the material in a ductile class; there is no common value to be used (Figure 2.2).

In ductile fractures,

- A relatively large amount of plastic deformation precedes the fracture.
- The fracture surface may appear to be fibrous or may have a matte or silky texture, depending on the material.
- The cross section at the fracture is usually reduced by necking.
- Crack growth is slow.

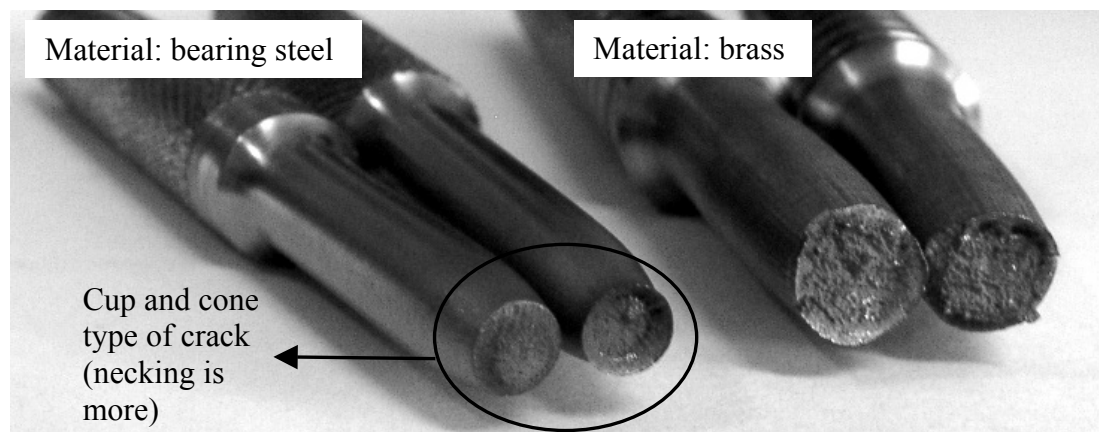


**Figure 2.2** Fractured tension specimens made of two different materials

However it is possible to have cracks occurring with no obvious or little macroscopic plastic deformation. On this basis, the fracture would be categorized as brittle. In brittle fractures,

- Little or no visible plastic deformation precedes the fracture.
- The fracture is generally flat and perpendicular to the surface of the component.

- The fracture may appear granular or crystalline and is often highly reflective to light.
- Cracks grow rapidly, often accompanied by a loud noise.

In most cold metal forming processes, workability is determined by the occurrence of ductile fracture and therefore limitations are set by the onset of surface or internal cracks within the regions that are highly strained due to extensive material flow. On the other hand, the occurrence of ductile fracture can be a natural part of metalworking operations such as blanking and machining that concern the separation of parts by the initiation and propagation of cracks. In terms of metalforming, the propagation of cracks is of little interest, since main issue is to avoid their initiation (Gouveia, 1999).

### **2.3 Criteria for Formability Analysis**

The damage of materials is the progressive physical process by which they break and the mechanics of damage is the study of the following mechanisms when materials are subjected to loading (Lemaitre, 1996):

- a) The accumulation of micro stresses in the neighborhood of defects or interfaces and the breaking of bonds, which both damage the material at the microscale level,
- b) The growth and the coalescence of micro cracks or micro voids which together initiate one crack at the mesoscale level of the representative volume element (RVE), and finally,
- c) The growth of that crack at the macroscale level.

The first two stages may be studied by means of damage variables of the mechanics of continuous media. The third stage is usually studied using fracture mechanics.

In literature, there exist several criteria suggesting various ways of calculating critical damage values to detect crack initiations. The basic idea of many ductile fracture criteria is that fracture occurs when the value of a damage parameter reaches a critical value. The critical value at which fracture initiates varies substantially from material to material, and can even vary for a given material with different annealing treatments.

Damage criteria can be divided into two:

a) Instantaneous Fracture Criteria

They look for a certain critical value of one of the process parameters for detecting fracture initiation.

b) Integral Fracture Criteria

They are developed to take the history of the material into account. Most of these criteria integrate the particular value with respect to strain.

And another classification is done as the damage criteria using empirical and semiempirical models and the damage criteria using theoretical void coalescence and growth (Shabara, 1996).

### **2.3.1 Damage Criteria using Empirical and Semiempirical Models**

Typical criteria for ductile fracture are usually based on combinations of stress with strain or strain rate, rather than on either of these quantities separately.

All the integrated stress–strain criteria based on empirical and semiempirical approach are versions of Freudenthal’s critical plastic work per unit of volume,

$$\int_0^{\bar{\varepsilon}_f} \bar{\sigma} d\bar{\varepsilon} = C_1 \quad (2.1)$$

where  $\bar{\sigma}$  is the effective stress,  $d\bar{\varepsilon}$  is effective strain increment and  $\bar{\varepsilon}_f$  is the effective strain at fracture (Freudenthal, 1950).

$C_i$ , where  $i : 1, 2, \dots$  are critical values, calculated by using these criteria.

In view of the importance of the largest tensile stress, Cockcroft and Latham have suggested an alternative fracture criterion based on a critical value of the tensile strain energy per unit of volume (Cockcroft, 1968).

$$\int_0^{\bar{\varepsilon}_f} \sigma_1 d\bar{\varepsilon} = C_2 \quad (2.2)$$

where  $\sigma_1$  is the largest (tensile) principal stress.

The normalized version of this criterion can be written as:

$$\int_0^{\bar{\varepsilon}_f} \frac{\sigma_1}{\bar{\sigma}} d\bar{\varepsilon} = C_3 \quad (2.3)$$

Explicit dependence on the level of both the largest (tensile) principal stress,  $\sigma_1$ , and the hydrostatic stress,  $\sigma_m$ , was proposed by Brozzo by means of an empirical modification of the above-mentioned criterion (Brozzo, 1972):

$$\int_0^{\bar{\varepsilon}_f} \frac{2\sigma_1}{3(\sigma_1 - \sigma_m)} d\bar{\varepsilon} = C_4 \quad (2.4)$$

Finally, the damage criterion suggested by Ayada is,

$$\int_0^{\bar{\varepsilon}_f} \frac{\sigma_m}{\bar{\sigma}} d\bar{\varepsilon} = C_5 \quad (2.5)$$

### 2.3.2 Damage Criteria using Theoretical Void Coalescence and Growth

Metals are organized in crystals or grains, a regular array of atoms except on many lines of dislocations where atoms are missing. If a shear stress is applied, the dislocations may move by the displacement of bonds, thus creating a plastic strain by slip.

Debonding is the beginning of the damage process. If the dislocation is stopped by a micro defect concentration, it creates a constrained zone in which another dislocation may be stopped. This process occurs with debonding, where several arrests of dislocations nucleate a micro crack. Other damage mechanisms in metals are intergranular debonding and decohesion between inclusions. (Lemaitre, 1996)

Elasticity is directly influenced by the damage, since the number of atomic bonds responsible for elasticity decreases with damage.

Plasticity is directly related to slips. In metals, slips occur by movement of dislocations. Damage influences plastic strains because the decrease in the elementary area of resistance, resulting from the decrease in the number of bonds, increases the effective stress.

Damage may be interpreted at the microscale as the creation of microsurfaces of discontinuities: breaking of atomic bonds and plastic enlargement of microcavities. Mesoscale is the scale in which Representative Volume Element (RVE) is defined (RVE is small enough to avoid smoothing of high gradients but large enough to represent an average of the microprocesses. At the mesoscale, the number of broken bonds or the pattern of microcavities may be approximated in any plane by the area of the intersections of all the flaws with that plane. This area is scaled by the size of

the representative volume element, showing the effect of micro defects over the mesoscale volume element.

As cited in Lemaitre (1996), Kachanov explained the ‘one-dimensional surface damage variable’ by considering a damaged body and a representative volume element (RVE) at a point  $M$  oriented by a plane defined by its normal  $\vec{n}$  and its abscissa  $x$  along the direction  $\vec{n}$ . (Figure 2.3)

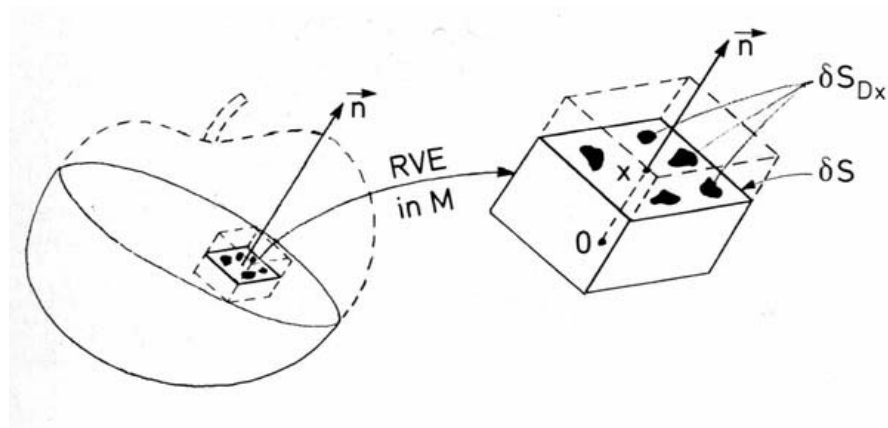


**Figure 2.3** Damaged RVE in a damaged body (Lemaitre, 1996)

The value of the damage  $D(M, \vec{n}, x)$  attached to the point  $M$  in the direction  $\vec{n}$  and the abscissa  $x$  is:

$$D(M, \vec{n}, x) = \frac{\delta S_{Dx}}{\delta S} \quad (2.6)$$

where,  $\delta S_{Dx}$  is the area of intersection of all the flaws with the plane defined by the normal  $\vec{n}$  and abscissa  $x$ ;  $\delta S$  is the total area at the intersection plane.

One must look at all the planes varying  $x$  and consider the one which is most damaged:

$$D(M, \vec{n}) = \text{Max}_{(x)} [D(M, \vec{n}, x)] \quad (2.7)$$

Then the coordinate  $x$  disappears, and:

$$D(M, \vec{n}) = \frac{\delta S_D}{\delta S} \quad (2.8)$$

For a simple one-dimensional case of homogeneous damage distribution of Figure 2.4, simple definition of damage as the effective surface density of microdefects is:

$$D = \frac{S_D}{S} \quad (2.9)$$

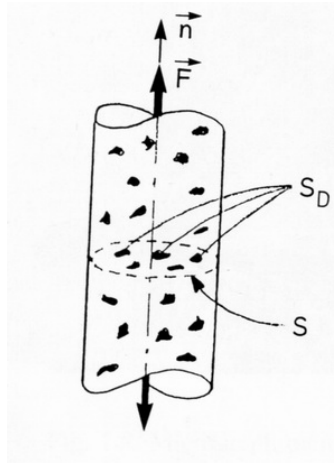


**Figure 2.4** Damaged RVE in a damaged body (Lemaitre, 1996)

Damage  $D$  is bounded as:

$$0 \leq D \leq 1 \quad (2.10)$$

Where  $D = 0$  represents the undamaged RVE material and  $D = 1$  represents fully broken RVE material in two parts. In fact, the failure occurs for  $D < 1$  through a process of instability, which suddenly induces the decohesion of atoms in the remaining resisting area. This rupture corresponds to a critical value of damage  $D_C$ , which depends upon the material and the conditions of loading.

$$0 \leq D \leq D_C \quad (2.11)$$

The methods to measure damage are classified as follows:

- a) Direct measurements: This is done by observing microcrack pictures.
- b) Variation of the elasticity modulus: This is an indirect measurement based on the influence of damage on elasticity:

$$\varepsilon_{el.} = \frac{\sigma}{E(1-D)} \quad (2.16)$$

This method requires accurate strain measurements. Strain gauges are commonly used and  $\bar{E}$  is most accurately measured during unloading. If  $\bar{E} = E(1-D)$  is considered as the effective elasticity modulus of the damaged material, the value of damage may be derived as:

$$D = 1 - \frac{\bar{E}}{E} \quad (2.17)$$

- c) Variation of the microhardness: This is an indirect measurement based on the influence of damage on plasticity.
- d) Variation of density: In case of pure ductile damage, the defects are cavities which can be assumed to be roughly spherical; this means that the volume increases with damage. The corresponding decrease of density can be measured to calculate damage.
- e) Variation of electrical resistance
- f) Acoustic emission: The location of the damaged zone is detected, but the results remain qualitative when the values of  $D$  are concerned.

Rabotnov introduced the effective stress concept in 1968 as follows (Lemaitre, 1996): If the RVE of Figure 2.3 is loaded by a force  $\vec{F} = F \vec{n}$ , the effective stress is:

$$\bar{\sigma} = \frac{F}{S} \quad (2.12)$$

If all microcracks or microcavities are represented by  $S_D$ , it is convenient to introduce a definition for effective stress in tension state,  $\bar{\sigma}_t$ , related to the surface that effectively resists the load:

$$\bar{\sigma}_t = \frac{F}{S - S_D} \quad (2.13)$$

Introducing the damage variable  $D = S_D/S$ ,

$$\bar{\sigma}_t = \frac{F}{S(1 - \frac{S_D}{S})} \quad \text{or} \quad \bar{\sigma}_t = \frac{\sigma}{1 - D} \quad (2.14)$$

This definition is for the effective stress in tension state. In compression state, if some defects close, the surface that effectively resists the load becomes larger than  $S - S_D$ . If all the defects close, the effective stress in compression becomes equal to the effective stress  $\bar{\sigma}$ .

Lemaitre has introduced the strain equivalence principle in 1971:

Any strain constitutive equation for a damaged material may be derived in the same way as for an undamaged material except that the effective stress is replaced by the effective stress defined for damaged materials.

$$\begin{aligned} D = 0 & \quad \rightarrow \varepsilon = f(\sigma, \dots) \\ 0 < D < D_C & \quad \rightarrow \varepsilon = f\left(\frac{\sigma}{1 - D}, \dots\right) \end{aligned} \quad (2.15)$$

The fracture of ductile solids has been observed to result from the large growth and coalescence of microscopic voids. This dependence guided McClintock to assume that fracture is reached when the spacing between voids in a material reaches a critical value. The fracture criterion derived from this assumption can be written as follows (McClintock, 1968):

$$\int_0^{\bar{\varepsilon}_f} \left[ \frac{\sqrt{3}}{2(n-1)} \sinh \left\{ \frac{\sqrt{3}(1-n)}{2} \frac{\sigma_a + \sigma_b}{\bar{\sigma}} \right\} + \frac{3}{4} \frac{\sigma_a - \sigma_b}{\bar{\sigma}} \right] d\bar{\varepsilon} = C_6 \quad (2.18)$$

where the symbol  $n$  represents the strain-hardening coefficient of the Ludwik-Holomon stress-strain relationship and  $\sigma_a$ ,  $\sigma_b$  are the principal stresses in the direction of the greatest and smallest void deformation.

Rice (1969) established a variational principle to characterize the flow field in an elastically rigid and incompressible plastic material containing an internal void or voids. The void enlargement rate is amplified over the strain rate by a factor rising exponentially with the ratio of mean normal stress to yield stress.

$$\int_0^{\bar{\varepsilon}_f} e^{\left( \frac{A\sigma_m}{\bar{\sigma}} \right)} d\bar{\varepsilon} = C_7 \quad (2.19)$$

where  $A$  is a material constant to be determined by experiments.

As mentioned before, metal forming processes involve various stress-strain paths; in other words, various paths of hydrostatic stress component. Hydrostatic stress has a great influence on fracture strain. Therefore, the fracture strain in one process differs from that in another (Oyane, 1980).

When the material is deformed, voids will be initiated in the material at a certain strain  $\varepsilon_i$ , the mechanical properties of the material are not necessarily worsened. Whether or not the fracture occurs in service depends on the conditions in which the products are used. For these reasons, it is not possible to determine the working limit exactly. For simplicity, the fracture strain  $\varepsilon_f$  is determined from noting the point when the crack is observable by the naked eye.

A criterion for the ductile fracture of pore-free materials is derived by Oyane from the equations of plasticity theory for porous materials. In order to apply the criterion to the ductile fracture of porous materials, it is so arranged that it includes a relative density term.

For calculation of the strain at fracture, it is desirable that the criterion is expressed in terms of strains. While the voids grow in size and number during plastic deformation, the density of the material decreases; finally the growth and coalescence of voids leads to the fracture of the material. The change in density, or volumetric strain, can thus be a good measure for describing ductile fracture. It is assumed that when the volumetric strain reaches a certain value  $\varepsilon_{vf}$ , which depends on the particular material, the material fractures. Assuming that after the initiation of fracture the material also obeys the equation of porous metals, the following criterion of ductile fracture is obtained:

$$\int_0^{\varepsilon_{vf}} f^2 \rho^{2n-1} d\varepsilon_v = \int_{\bar{\varepsilon}_i}^{\bar{\varepsilon}_f} \left( A + \frac{\sigma_m}{\bar{\sigma}} \right) d\bar{\varepsilon} \quad (2.20)$$

where  $f$  is a function of the relative density  $\rho$  (defined by the ratio of the apparent density of the porous material to the density of its pore-free matrix),  $n$  is a material constant,  $\bar{\sigma}$  is the equivalent stress,  $\sigma_m$  is the hydrostatic component of stress,  $\bar{\varepsilon}_i$  is the equivalent strain at which voids are initiated,  $\bar{\varepsilon}_f$  is the equivalent strain at which fracture occurs and  $A$  is a material constant. The quantity of the left hand side of Eq. (2.20) is dependent only on the material. Therefore Eq. (2.20) reduces to the following form:

$$\int_{\bar{\varepsilon}_i}^{\bar{\varepsilon}_f} \left( 1 + \frac{\sigma_m}{A\bar{\sigma}} \right) d\bar{\varepsilon} = C \quad (2.21)$$

where  $C$  is a material constant, i.e.,

$$C = \frac{1}{A} \int_0^{\varepsilon_{vf}} f^2 \rho^{2n-1} d\varepsilon_v \quad (2.22)$$

Strain at which the voids are initiated depends on the pressure. If it is assumed that  $\varepsilon_{eq,i} = 0$ , Eqn (2) reduces to a very simple form:

$$\int_0^{\bar{\varepsilon}_f} \left( 1 + \frac{\sigma_m}{A \bar{\sigma}} \right) d\bar{\varepsilon} = C \quad (2.23)$$

The material constants are estimated by upsetting of cylindrical specimen. Axial and circumferential strains can be measured at the equator of the bulged surface of upset cylinders and the stresses can be calculated. When a surface crack is observable by the naked eye, the specimen is unloaded, and therefore  $\bar{\varepsilon}_f$  is obtained.

Eq. (2.23) is rewritten as:

$$\bar{\varepsilon}_f = -\frac{1}{A} \int_0^{\bar{\varepsilon}_f} \frac{\sigma_m}{\bar{\sigma}} d\bar{\varepsilon} + C \quad (2.24)$$

Integral term of Eq. (2.24) is calculated and then plotted against  $\bar{\varepsilon}_f$  for various specimen (various initial height to diameter ratios  $H_0/D_0$ ). This plot represents a linear relationship of  $y = mx + n$ . Therefore, material constant  $A$  can be obtained from the slope of the straight line,

$$m = -\frac{1}{A} \quad (2.25)$$

and material constant  $C$  from the intersection of the ordinate and this line,

$$C = n \quad (2.26)$$

### 2.3.3 Damage Criteria in FEM Applications

In FEM simulations, the modeled process is analyzed in several steps. For each step the strain-rate, strain, stress and other parameters as damage are calculated.

If the distortion of the elements gets too large, a new mesh must be generated and the data from the old mesh is interpolated to the new mesh. Since some of the data may be lost during remeshing due to volume loss or rounding effects, the goal is to control these changes and use necessary number of remeshing steps.

In this study, FEM simulation program DEFORM 2D version 7.1 has been used throughout the modeling of experiments, including failure and friction analysis. DEFORM is one of the commercial Finite Element Method (FEM) applications, in which some of the damage models are implemented.

There are different damage models implemented in DEFORM. It is also possible to write a user subroutine, which can be used for the own damage model. The damage models of DEFORM used in this study are:

- Cockcroft & Latham
- Cockcroft & Latham normalized
- McClintock
- Freudenthal
- Rice & Tracy
- Oyane
- Ayada
- Brozzo
- Maximum effective stress / ultimate tensile strength

These criteria are used in modeling of several experiments to calculate critical damage values for crack initiation.

## 2.4 Obtaining Material Flow Curves

Flow curves will be used in FEM simulations of the performed failure experiments as the material data. The final dimensions and stress-strain distribution of the specimens have to be obtained from the modeling of experiments very close to reality. Therefore it is very important to obtain flow curves correctly. Tension and compression tests are the most popular material flow characterization tests in metal forming. Tension test is the best-described test, but supplies a flow curve for lower strain values than the compression test does. The tension and compression tests are explained in following sections in detail.

### 2.4.1 Tension Test

A tension test consists of pulling a sample of material with a tensile load until it breaks into two parts. The test specimen usually has circular cross section. The ends of tensile specimens are usually enlarged to provide extra area for gripping and to avoid having the sample break where it is being gripped.

The pulling load  $P$  may be divided by the initial cross-sectional area  $A_0$ , to obtain engineering stress in the specimen at any time during the test.

$$\sigma_{eng} = \frac{P}{A_0} \quad (2.27)$$

Axial displacement of the specimen is measured within a straight central portion of constant cross section over a gage length  $L_0$ . Engineering strain  $\epsilon_{eng}$  may be computed from the change of this length,  $\Delta L$ .

$$\epsilon_{eng} = \frac{\Delta L}{L_0} \quad (2.28)$$

It is reasonable to assume that all of the grip parts and the specimen ends are nearly rigid. In this case, virtually all of the change in length is due to deformation within the straight section of the test specimen (Figure 2.5).

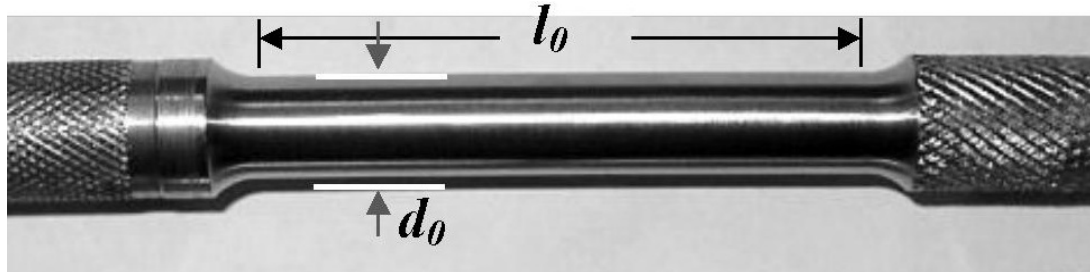


**Figure 2.5** Tension test specimen and related dimensions

The ultimate tensile strength,  $\sigma_u$ , also called simply the tensile strength, is the highest engineering stress reached prior to fracture. If the behavior is brittle, the ultimate strength occurs at the point of fracture. However, in ductile metals, engineering stress reaches a maximum and then decreases prior to fracture. The highest load reached at any point during the test,  $P_{max}$ , is used to obtain the ultimate strength by dividing with the initial cross-sectional area.

$$\sigma_u = \frac{P_{max}}{A_0} \quad (2.29)$$

The departure from linear-elastic behavior is called yielding. This is simply because the stresses that cause yielding result in rapidly increasing deformation due to the contribution of plastic strain. The yielding event can be characterized by several methods. The simplest is to identify the stress where the first departure from linearity occurs. This is called the proportional limit,  $\sigma_p$ . Some materials may exhibit a stress-strain curve with a gradually decreasing slope and no proportional limit. Even where there is a definite linear region, it is difficult to precisely locate where this ends. Hence, the value of proportional limit depends on judgment, so that this is a poorly defined quantity. Another quantity sometimes defined is the elastic limit, which is the highest stress that does not cause plastic deformation. Determination of

this quantity is difficult, as periodic unloading to check for permanent deformation is necessary. A third approach is the offset method. A straight line is drawn parallel to the elastic slope,  $E$  or  $E_t$ , but offset by an arbitrary amount. The intersection of this line with the engineering stress-strain curve is a well-defined point that is not affected by judgment. This is called the offset yield strength,  $\sigma_{0.2\%}$ . The most widely used and standardized offset for engineering metals is a strain of 0.002, that is 0.2%.

True stress in a simple tension test is simply the load  $P$  divided by the current cross-sectional area  $A$ , rather than the original area  $A_0$ .

$$\sigma_{true} = \frac{P}{A} \quad (2.30)$$

Hence, true and engineering stress are related by,

$$\sigma_{true} = \sigma_{eng} \left( \frac{A_0}{A} \right) \quad (2.31)$$

Total true strain can be defined with below integral.

$$\epsilon_{true} = \int_{L_0}^L \frac{dL}{L} = \ln \frac{L}{L_0} \quad (2.32)$$

where  $L = L_0 + \Delta L$  is the final length. Noting that  $\epsilon_{eng} = \Delta L / L_0$  is the engineering strain, this leads to a relationship between  $\epsilon_{eng}$  and  $\epsilon_{true}$ .

$$\epsilon_{true} = \ln \frac{L_0 + \Delta L}{L_0} = \ln \left( 1 + \frac{\Delta L}{L_0} \right) = \ln(1 + \epsilon_{eng}) \quad (2.33)$$

Once the strains have increased substantially beyond the yield region, most of the strain that has accumulated is inelastic strain for materials that behave in a ductile manner. The volume change in a tension test is limited to the small change associated with elastic strains; plastic strains do not contribute to volume change. It is therefore reasonable to take the volume as constant.

$$A_0 L_0 = AL \quad (2.34)$$

This gives,

$$\frac{A_0}{A} = \frac{L}{L_0} = \frac{L_0 + \Delta L}{L_0} = 1 + \varepsilon_{eng} \quad (2.35)$$

Substitution of the above equation into Eq. (2.33) gives:

$$\varepsilon_{true} = \ln\left(\frac{A_0}{A}\right) = \ln(1 + \varepsilon_{eng}) \quad (2.36)$$

If the behavior in a tension test is ductile, a phenomenon called necking usually occurs. The deformation is uniform along the gage length early in the test, but later begins to concentrate in one region, resulting in the diameter there decreasing more than elsewhere. In ductile metals, necking begins at the ultimate strength point, and the decrease in load beyond this point is a sequence of the cross-sectional area rapidly decreasing.

A complication arises in interpreting tensile results near the end of a test where there is a large amount of necking. As pointed out by Bridgman (1944), large amounts of necking result in a tensile hoop stress being generated around the circumference in the necked region (Bridgman, 1944). Thus, the state of stress is no longer uniaxial as assumed and the axial stress is increased above what it should be. A correction in order to have the uniaxial state can be made by using the stress correction factor

$\left(1 + 2\frac{R}{a}\right) \ln\left(1 + \frac{1}{2}\frac{a}{R}\right)$  that is given by Bridgman. The inverse of this factor, may be called the correction factor, since it is the factor by which the uncorrected true stress is to be multiplied to obtain the corrected true stress (Figure 2.6).

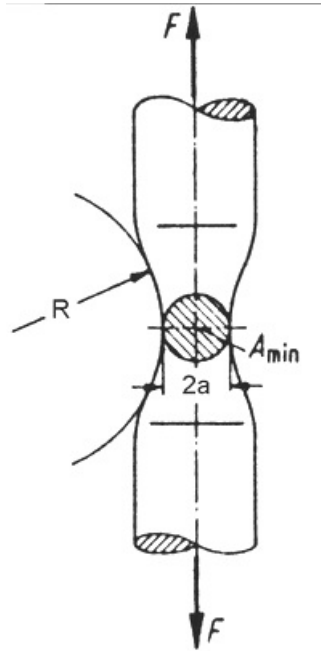


**Figure 2.6** Schematic representation of  $a$  and  $R$  values (Lange, 1985)

$$\tilde{\sigma}_B = \frac{1}{\left(1 + 2\frac{R}{a}\right) \ln\left(1 + \frac{1}{2}\frac{a}{R}\right)} \tilde{\sigma} \quad (2.37)$$

where,  $\tilde{\sigma}$  is the uncorrected true stress ( $\tilde{\sigma} = F/A_{\min}$ ) and  $\tilde{\sigma}_B$  is the corrected true stress.

The corresponding equivalent strain is given by:

$$\bar{\epsilon} = \ln\left(\frac{A_0}{A_{\min}}\right) \quad (2.38)$$

where  $A_{min}$  is the minimum cross-section in the necking zone at a given force. By this method the flow curve can be determined up to strains of order of unity.

If the flow curve shall only be determined for low strains, tensile test provides sufficient information. Low strains can be extrapolated to higher ones by using Ludwik's equation:

$$\sigma = K \bar{\varepsilon}_{pl}^n \quad (2.39)$$

where  $n$  is called the strain hardening coefficient, and  $K$  is the strength coefficient. Still Ludwik's equation should only be used for rough estimations.

#### 2.4.2 Compression Test

Since metals generally exhibit their lowest formability under tensile stress, compression test is performed to attain higher strain values (Lange, 1985).

The conventional upsetting test of circular cylinders can be described as the compression of a cylindrical test piece between plane parallel dies with lubricated or dry surface (Figure 2.7).

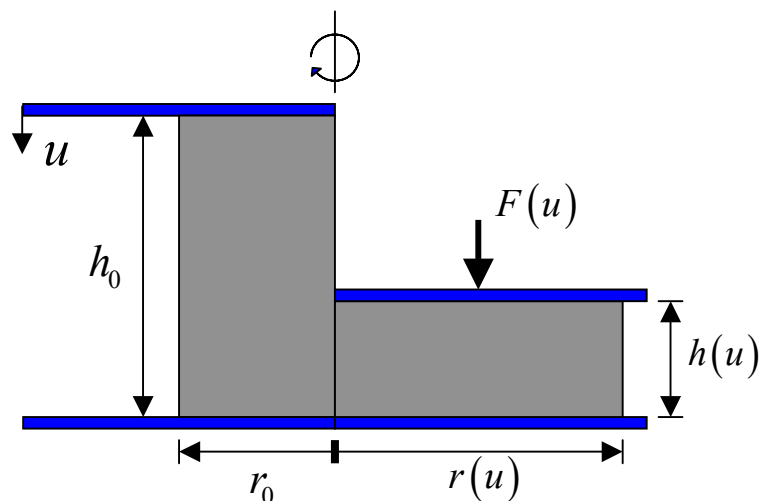


**Figure 2.7** Schematic representation of compression test without any friction (Koçaker, 2003)

True strain is obtained by using the equation,

$$\varepsilon(u) = \ln \frac{h(u)}{h_0} < 0 \quad (2.40)$$

where,  $h(u)$  is the actual height of the specimen corresponding to applied force  $F$ . So it can be written as:

$$h(u) = h_0 - u \quad (2.41)$$

where  $u$  is the measured reduction of height.

True stress value can be calculated from the measured force  $F$  and the reduction of height  $u$  of the specimen.

$$\sigma_f(u) \approx \frac{F(u)}{\pi r^2(u)} \quad (2.42)$$

One major source of error is the friction between the end of the specimen and the dies. Friction has two effects:

1. An additional force is required for attaining a given strain. According to Siebel, Eq. (2.42) has to be replaced by

$$\frac{F(\bar{\varepsilon})}{\pi r^2(\bar{\varepsilon})} \approx \sigma(\bar{\varepsilon}) \left\{ 1 + \frac{2\mu r(\bar{\varepsilon})}{3h(\bar{\varepsilon})} \right\} \quad (2.43)$$

where  $\mu$  is the Coulomb coefficient of friction. In order to minimize the correction term in Eq. (2.43) which describes the influence of friction, the slenderness ratio of the specimen should be as high as possible. However, because of the danger of instability, it has to be confined to certain limits.

2. Friction causes barreling of the specimen.

Flow curve obtained from standard compression test data contains some errors due to the nonhomogeneous deformation (barreling), introduced as a result of the friction between compression specimen and dies.

Correction of the flow data can be done by Siebel correction function and iterative FEM method. For both methods value of friction coefficient is required.

According to the Siebel's correction, corrected stress can be written as:

$$\sigma_{siebel}(\varepsilon) = \frac{\sigma_{exp}(\varepsilon)}{c_{siebel}(\varepsilon)} \quad (2.44)$$

where

$$\sigma_{exp}(\varepsilon) = \frac{F(\varepsilon)}{\pi r^2(\varepsilon)} \quad (2.45)$$

and

$$c_{siebel}(\varepsilon) = \left( 1 + \frac{2\mu r(\varepsilon)}{2h(\varepsilon)} \right) \quad (2.46)$$

Siebel's correction is very easy to apply; for low strain and friction coefficients it gives reliable results.

Parteder & Bünthen successfully applied iterative FEM method to obtain flow curve from a compression test under sticking friction conditions and called this method as iterative finite-element procedure. Friction free flow curve can be obtained even in the first iteration with enough accuracy (Parteder, 1998).

The process to determine the friction free flow curve by iterative FEM method is carried out as follows:

1. The load-stroke curves of compressed specimen are determined by compression test and experimental flow curve  $\sigma_{\text{exp}}(\varepsilon)$  is obtained as described in Eq (2.45).
2.  $\sigma_{\text{exp}}(\varepsilon)$  is input to the FEM program, then, two simulations of the experimental compression test are modeled with the same number of steps. One of the simulations uses the coefficient of friction obtained by ring test and the other uses zero-friction. Load-stroke data are taken as output from both FEM simulations and converted to the true stress – strain curve.

$$\begin{aligned}\sigma_{FEM}^{i+1}(\varepsilon) &: FEM(\sigma_{\text{exp}}(\varepsilon))^{\text{with friction}} \\ \sigma_{input}^i(\varepsilon) &: FEM(\sigma_{\text{exp}}(\varepsilon))^{\text{zero friction}}\end{aligned}\quad (2.47)$$

where  $i$  is the number of iterations ( $i = 0, 1, 2, \dots$ ) to correct the flow curve.

Zero-friction model is used in order to be able to compare the stresses at the same strain values, as the simulations with the same number of steps supply the same displacements and therefore the strains at each step.

3. Calculation of correction function is done by dividing true stress values calculated from the simulation with non-zero friction coefficient by those calculated from the simulation with zero-friction at the same strain values.

$$c_{FEM}^{i+1}(\varepsilon) = \frac{\sigma_{FEM}^{i+1}(\varepsilon)}{\sigma_{input}^i(\varepsilon)} \quad (2.48)$$

The data representing the value of correction factor for different strain values in experimental range of flow curve is then fitted to a polynomial in order to apply it on the experimental flow curve.

4.  $\sigma_{input}^{i+1}(\varepsilon)$  is calculated by dividing  $\sigma_{exp}(\varepsilon)$  by the correction function. This flow curve can be assumed as the friction free flow curve if almost the same flow curve is obtained from next iteration.

$$\sigma_{input}^{i+1}(\varepsilon) = \frac{\sigma_{exp}(\varepsilon)}{c_{FEM}^{i+1}(\varepsilon)} \quad (2.49)$$

If this is not the case it will be input flow curve for FEM simulation for the next iteration (steps (2), (3) and (4) will be repeated).

## 2.5 Friction Analysis

Friction analysis is required both in order to eliminate the effect of friction on compression flow curve as mentioned in 2.4.2 and in order to model the experiments correctly.

Whenever two solid surfaces are in contact and in relative motion, resistance to this motion arises. This resistance is called friction. Friction exists in any metal forming process.

In metal forming processes, friction plays a significant role. It affects the deformation load, formability of the material and product surface quality that also determines the life of the tool. Excessive friction leads to heat generation and wear of the tool surface. Friction can increase the inhomogeneity of the deformation, leading to defects in the finished product. Understanding of the friction phenomenon is, therefore, significant for understanding what actually happens at the die-workpiece interface under many different conditions and deformation processes.

Application of a suitable lubricant may reduce friction, but will never eliminate it completely. A good lubricant will minimize metal-to-metal contact by wetting both surfaces and adhering to them. It may form a bond or a very soft chemical compound with these surfaces, so that the shear stress needed to separate the two surfaces will then be no higher than the shear strength of the weak compound (Avitzur, 1983).

After obtaining the friction condition between the material and the dies of the hydraulic press used in experiments, the experiments can be modeled correctly in FEM.

### **2.5.1 Friction Models in Metal Forming**

Three friction models will be explained in this section. First one is Coulomb friction model, second one is shear friction model, and third one is Bay's friction model.

#### **2.5.1.1 Coulomb (Amonton) Friction Model**

Figure 2.8 represents the typical real behavior of the shear stress between the tool and material with respect to normal pressure (Avitzur, 1983). For low pressures, an approximation can be made, where the shear stress is proportional to the pressure. This friction law is called Coulomb's law or Amonton's law of friction, and the constant proportionality factor is called the coefficient of friction and denoted by  $\mu$ . This constant is independent of the pressure, however, is a function of the two mating surfaces, the lubricant used and the temperature.

According to Coulomb, friction force is directly proportional to normal force, as

$$F_{friction} = \mu \cdot F_{Normal} \quad (2.50)$$

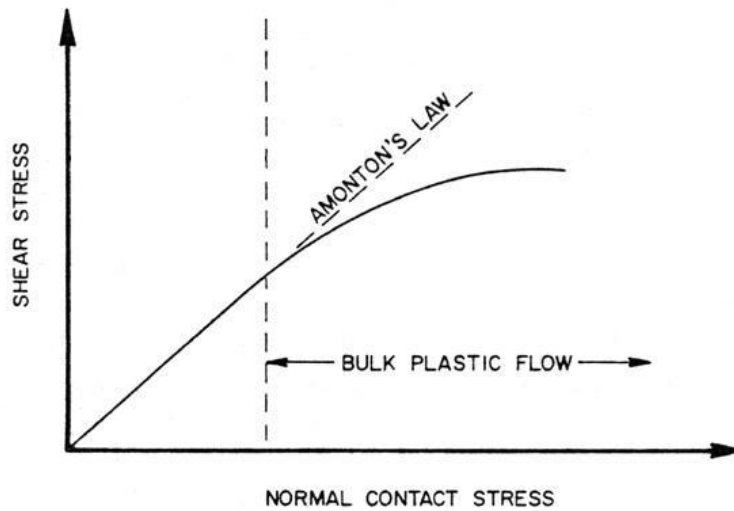


**Figure 2.8** Variation of sliding-contact shear stress with normal contact stress  
(Avitzur, 1983)

and by dividing both sides by the contact area:

$$\tau_{friction} = \mu \cdot \sigma_{Normal} \quad (2.51)$$

### 2.5.1.2 Shear Friction Model

Being an alternative to the Coulomb (Amonton) friction model, for high pressures, it has been suggested that shear stress is proportional to the flow stress of the material, and is not proportional to the pressure. The proportionality factor  $m$  is called the constant shear factor. It is dependent on the two mating surfaces, on the lubricant and therefore on the temperature.

Frictional shear stress is constant and equal to a factor of maximum shear stress.

$$\tau_{friction} = m \cdot k \quad (2.52)$$

where,  $k$  is maximum shear stress and  $m$  is friction factor that can have values between 0 and 1.

### **2.5.2 Effect of Friction on Formability**

The upsetting of a small cylinder at room temperature is one of the most widely used workability tests. As it is compressed in the presence of friction, it usually tends to barrel, and a biaxial stress state, which consists of a circumferential tensile stress and an axial compressive stress, develops at the equator of the cylinder.

In the absence of friction, the tensile strain is equal to one-half of the compressive strain. Bulging, which is caused by friction, increases the circumferential tensile strain. Axial compressive stress may also turn into axial tensile stress depending on the degree of barreling.

A stress state that is composed of tensile components increases the material tendency to create cracks. Variation of the friction conditions and of the upset cylinder's aspect ratio make changes on barrel curvature and on the equatorial stress state. This creates some flexibility on formability testing by upsetting. Therefore friction and barreling, which is a disadvantage for flow stress measurements, has a preferable effect for formability testing.

Determination of friction coefficient is important for formability testing because of the expectations given above. It is also important to know about the friction conditions when obtaining flow curves for the material under formability investigations. As mentioned before, friction effect should be erased from the experimentally obtained stresses of upsetting test, in order to have the friction-free flow stress.

Therefore, estimation of the friction condition is needed for this study.

### **2.5.3 Ring Compression Test**

Several methods have been developed for quantitative evaluation of friction in metal forming processes. The ring compression test was originated by Kunogi (Kunogi,

1956) and later improved and presented in a usable way by Male & Cockcroft (Male, 1965). The most accepted one for quantitative characterization of friction is to define a coefficient of friction,  $\mu$ , at the die-workpiece interface. In the present study, the Coulomb law of friction is used to model the interface friction.

In the ring test, a ring-shaped specimen is compressed to a known reduction. The change in the internal and the external diameters of the forged ring is very much dependent on the friction at the tool-specimen interface.

The internal diameter of the ring is reduced if the friction is high, and is increased if the friction is low. When a flat ring specimen is plastically compressed between two flat platens, increasing friction results in an inward flow of the material, while decreasing friction results in an outward flow of the material as schematically shown in Figure 2.9.

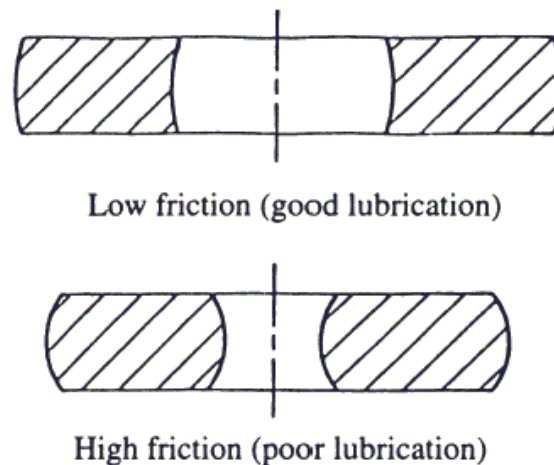


**Figure 2.9** Effect of friction magnitude on metal flow during the ring compression test. (Sofuoglu, 1999)

For a given percentage of height reduction during compression tests, the corresponding measurement of the internal diameter of the test specimen provides a quantitative knowledge of the magnitude of the prevailing friction coefficient at the die/workpiece interface. Generally, the results of theoretical analysis and

experimental work are presented in the form of calibration curves, relating the percentage reduction in the internal diameter of the test specimen to its reduction in height for varying degrees of the coefficient of friction as shown in Figure 2.10.

Although the ring compression test is an effective method for determining the friction coefficient during large deformation processes, the use of a generalized friction calibration chart regardless of the material type and test conditions must be avoided. It is therefore recommended that for obtaining reliable data regarding the coefficient of friction, the results of ring compression tests be used in conjunction with calibration curves generated specifically for the material under investigation and under the specific test conditions.

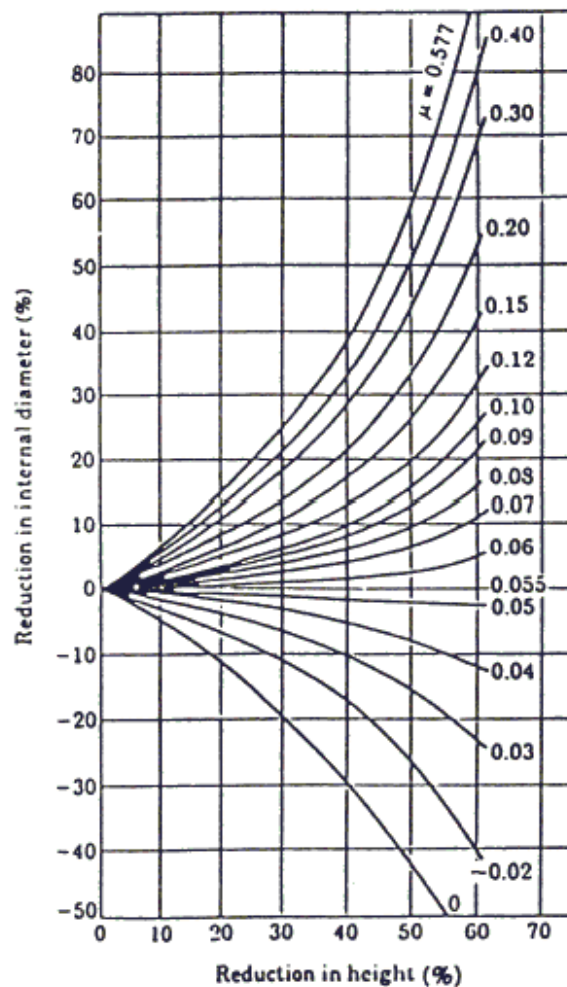


**Figure 2.10** Friction calibration curves in terms of  $\mu$ . (Male, 1965)

## CHAPTER 3

### FORMABILITY ANALYSIS OF STEEL 100Cr6

#### 3.1 Introduction

In this chapter, the formability limits of material 100Cr6 will be examined. This bearing steel is supplied from ORS Bearing Company (Ankara, Turkey) in annealed condition. First, the material flow curve is obtained. Then the results on failure experiments are given in detail. The modeling of these experiments is explained and the conclusions on the success of various failure criteria are presented.

#### 3.2 Obtaining Material Flow Curves

Tension and standard compression tests have been conducted in order to obtain the flow curve of material 100Cr6. These flow curves have been used in FEM simulations of the performed failure tests. The procedure and calculation methods for tension and compression tests are explained in Section 2.4.

##### 3.2.1 Tension Flow Curve

Tension test specimens (Figure 3.1) of 8 mm gage diameter ( $d_0$ ) and 50 mm gauge length ( $l_0$ ) were tested using a Mohr&Federhaff hydraulic testing machine. This machine has an approximate punch velocity of 0.08 mm/sec and 40 tons of loading capacity. Tests were repeated three times to ensure repeatability.

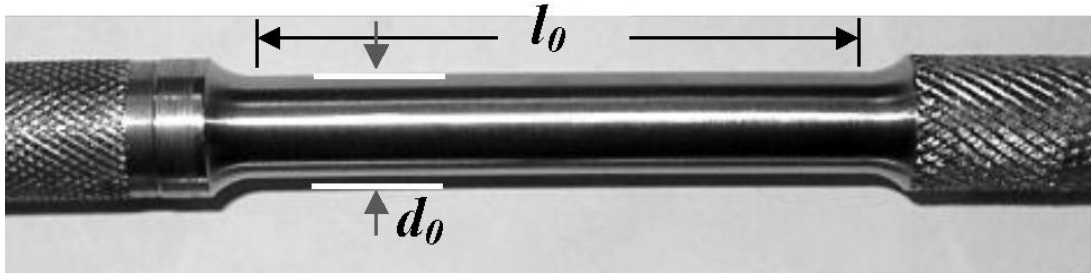


**Figure 3.1** Tension test specimen and related dimensions

Experimental output has been taken as a load-displacement curve, drawn by the testing machine on a graphic paper. This paper has been scanned first and then several points that can represent the details of this curve are selected. The  $x$  and  $y$  coordinates of these points, which are load in pixels and stroke in pixels respectively, are noted by taking the origin as the reference and the starting point of the curve. The pixels are then calibrated to represent load (in N) and stroke (in mm) curve as given in Figure 3.2.

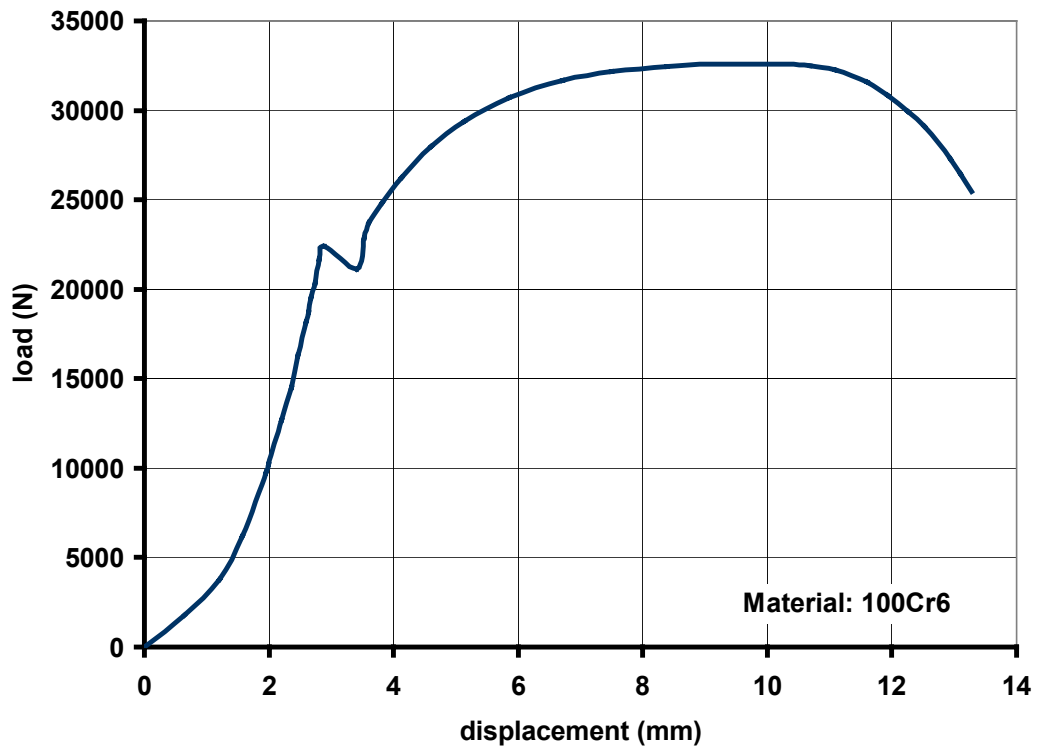


**Figure 3.2** Tension test load-stroke curve

Load stroke data can easily be converted to engineering stress – engineering strain data with the help of Eqs. (2.27), (2.28) and to true stress – true strain data with the help of Eqs. (2.32), (2.36). Maximum point on engineering stress – strain curve gives the point where the necking starts and the ultimate tensile strength,  $\sigma_u$  as shown in Figure 3.3. For the 100Cr6 specimen, ultimate tensile strength can be taken as  $\sigma_u = 643\text{MPa}$ , and necking strain as  $\varepsilon_{eng}^{necking} = 0.198$ .

Material response is clear at the yielding region; therefore 0.002 offset strain method is not used to define the yield stress for this material. It is shown to be  $\sigma_0 = 444\text{MPa}$  on Figure 3.3.

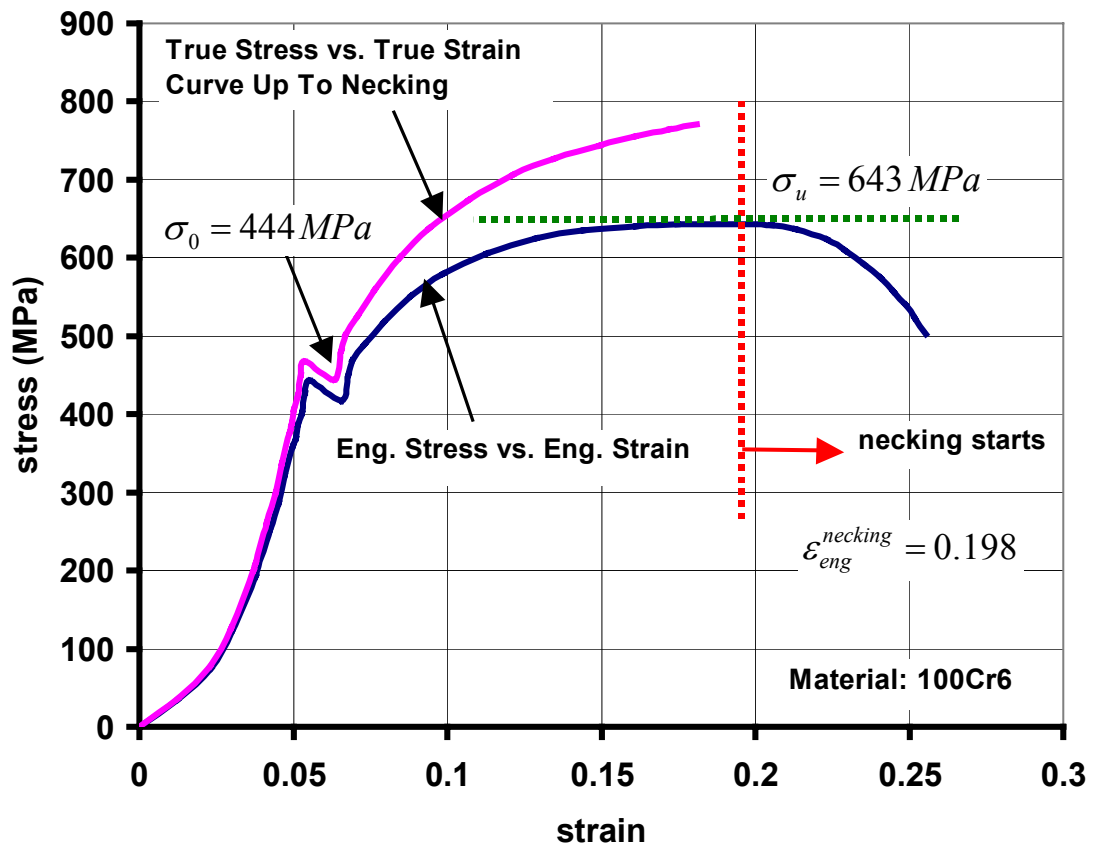


**Figure 3.3** Stress and strain curve of material 100Cr6 obtained from tension test

From Figure 3.3 it can be seen that tension data is only available up to true strain  $\varepsilon_{true}$  of 0.18. After this point, non-uniform elongation starts.

The flow curve can be obtained by plotting true stress values against corresponding equivalent true plastic strain values determined by the Eq. (3.1).

$$\varepsilon_{pl} = \varepsilon_{true} - \varepsilon_{el} = \varepsilon_{true} - \varepsilon_0 - \left( \frac{\sigma_{true} - \sigma_0}{E} \right) \quad (3.1)$$

In this equation,  $\varepsilon_{pl}$  denotes the total equivalent plastic strain,  $\varepsilon_{el}$  is the total elastic strain,  $\sigma_0$  is the initial yield stress,  $\varepsilon_0$  is the true strain at initial yield point and  $E$  is the modulus of elasticity. Figure 3.4 shows the flow curve of 100Cr6 obtained from tension test without any extrapolation.

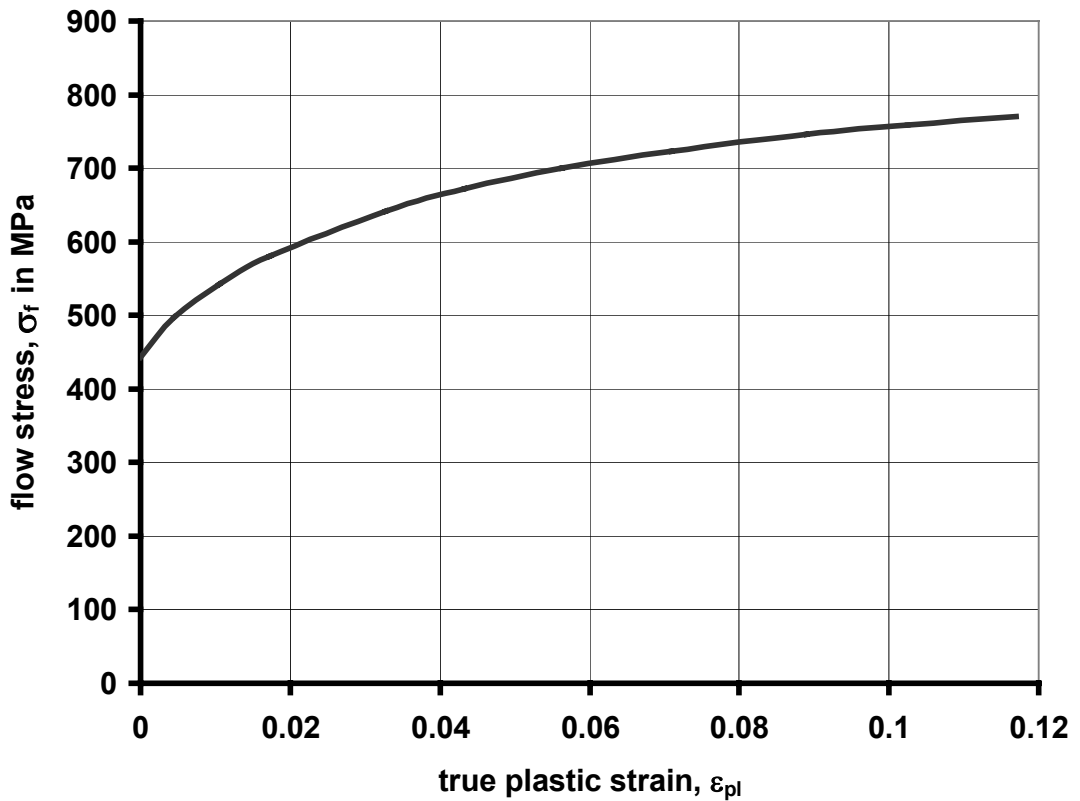


**Figure 3.4** Tensile flow curve of 100Cr6

The flow stress for higher strain values can be obtained from the extrapolation of the experimental flow curves by using Ludwik's law, given in Eq. (2.39). Eq. (2.39) can be written as:

$$\ln(\sigma) = \ln(K) + n \ln(\varepsilon_{pl}) \quad (3.2)$$

which can usually be fit to a straight line on an  $x$ - $y$  plot having the equation,

$$y = mx + b \quad (3.3)$$

where  $y = \ln(\sigma)$ ,  $x = \ln(\varepsilon_{pl})$ ,  $m = n$ ,  $b = \ln(K)$  and therefore  $K = e^b$ .

Equation of the straight trend line given in Figure 3.5 is used for calculating  $n$  and  $K$  values.

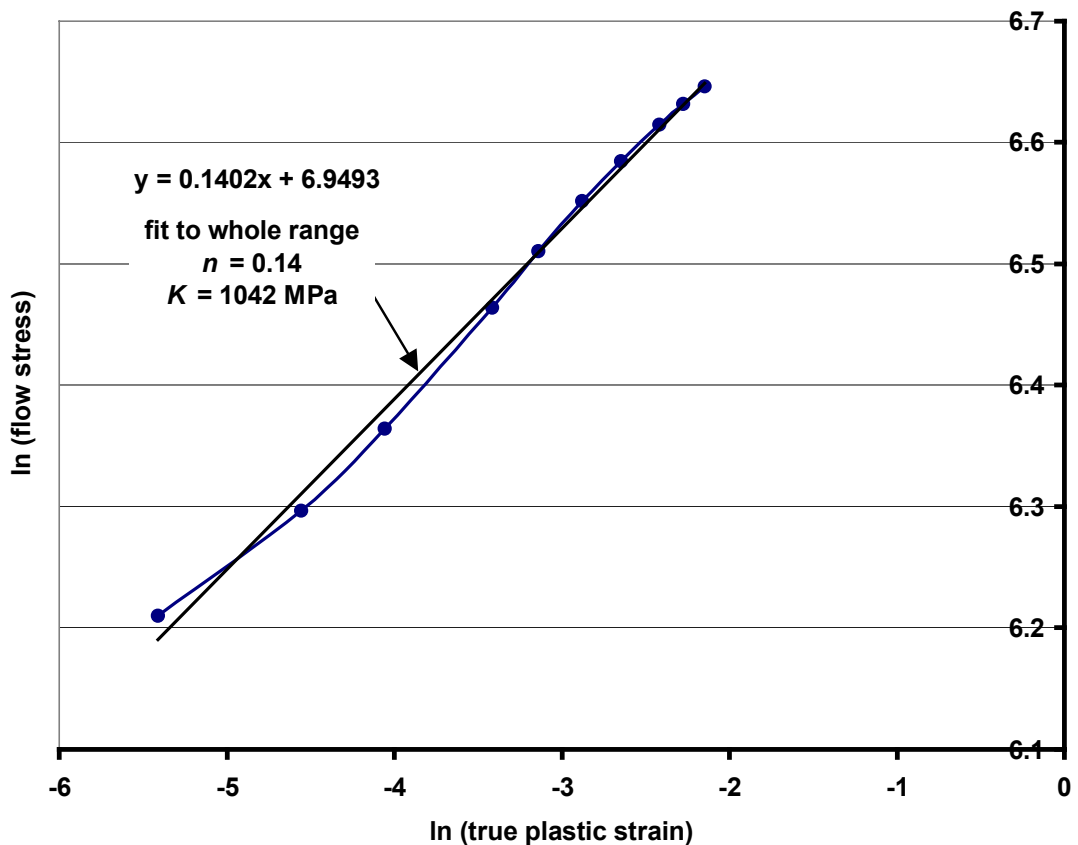


**Figure 3.5** Determination of  $n$  and  $K$  from the  $\log$ - $\log$  plot of tensile flow curve

Both experimental and extrapolated tensile flow curves are shown in Figure 3.6. The flow curve with  $n$  and  $K$  values from the whole range data of flow curve fits very fine to the experimental flow curve, although poorly represents the starting part of experimental flow curve, where  $\varepsilon_{pl} \approx 0$ . Therefore, the method to extrapolate the flow curve is to take the experimental flow curve and extrapolate the rest with  $n$  and  $K$  values obtained from the whole range of flow data.

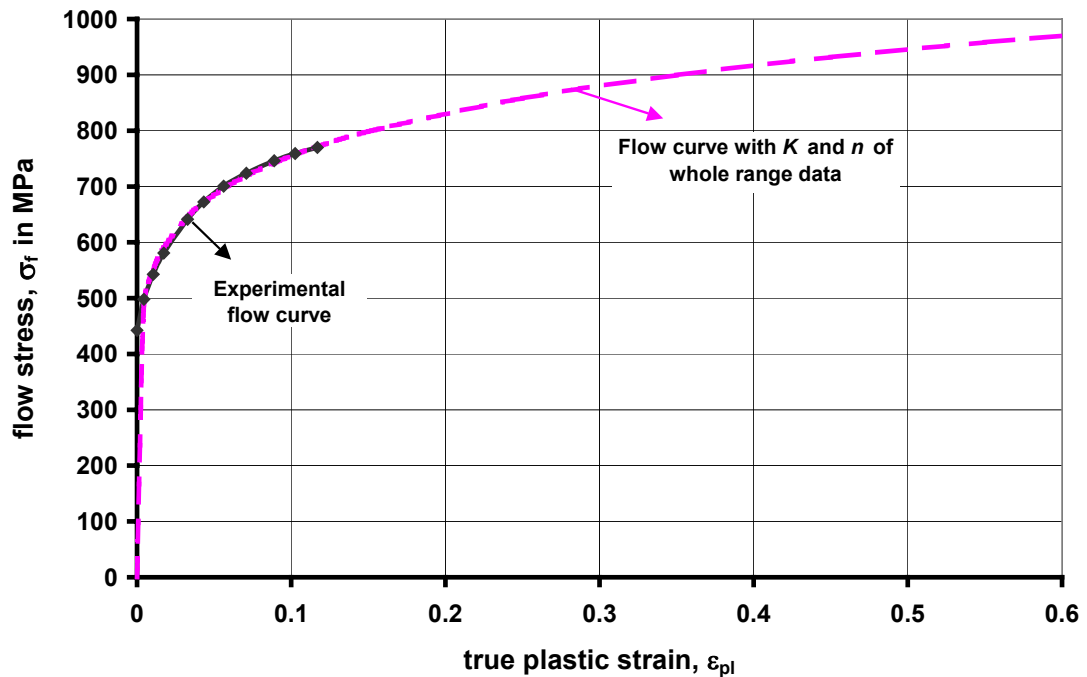


**Figure 3.6** Extrapolated tension 100Cr6 flow curve

### 3.2.2 Compression Flow Curve

Cylindrical specimens of 10 mm diameter and 15 mm height were compressed by using 40 tons Mohr&Federhaff hydraulic testing machine. Load-stroke curve of such a test is obtained by the same procedure mentioned in Section 3.2.1 and the resulting curve is shown in Figure 3.7.

Load stroke data can easily be converted to engineering stress – engineering strain data and to true stress – true strain data with the help of Eqs. (2.40), (2.42). These curves are represented in Figure 3.8.

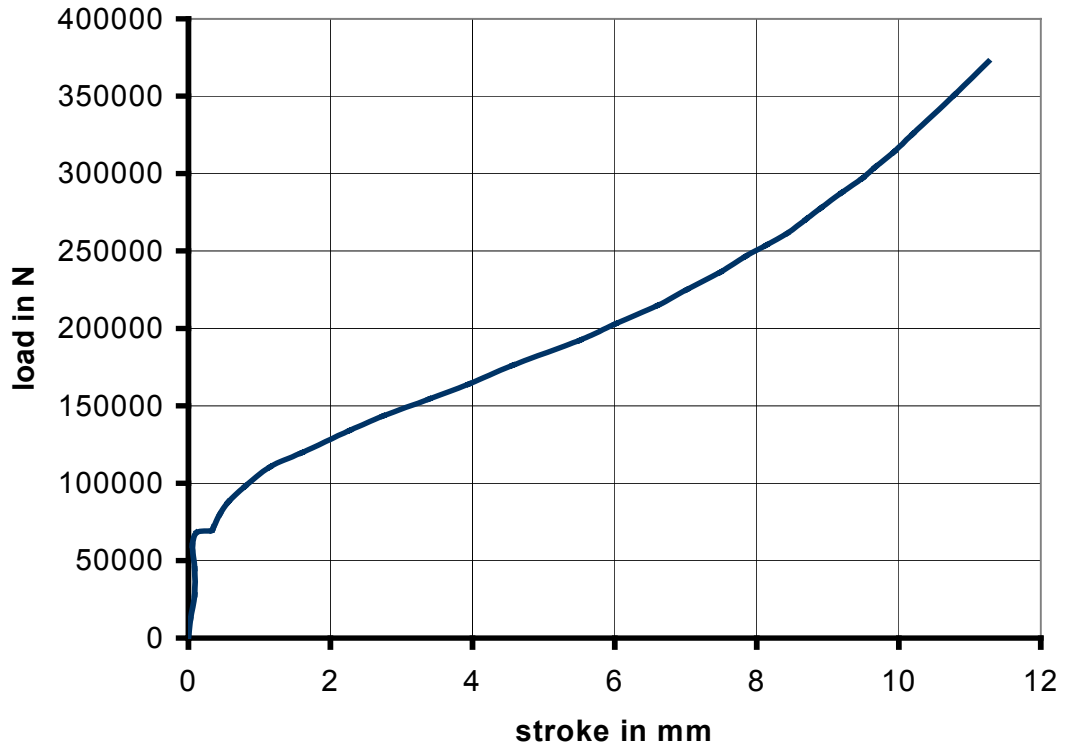


**Figure 3.7** Load-stroke curve of material 100Cr6 obtained from standard compression test

Material response is clear at the yielding region; therefore 0.002 offset strain method is not used to define the yield stress for this material. It is shown to be  $\sigma_0 = 443 \text{ MPa}$  on Figure 3.8.

From Figure 3.8 it can be seen that compression data is available up to  $\epsilon_{true} = 0.75$  due to the dimensions of the manufactured specimens and the loading capacity of the hydraulic press. Flow curve can be fitted to a power equation, in order to represent a smooth flow curve, instead of the wavy appearance of experimental curve (Figure 3.9).

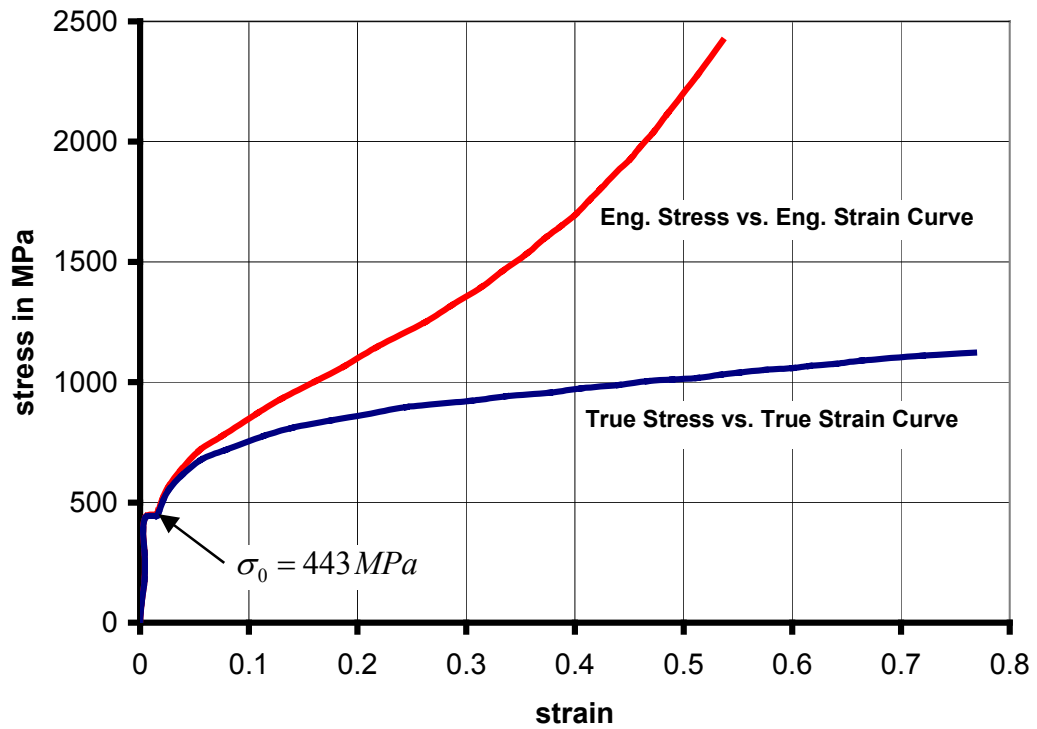


Figure 3.8 Stress and strain curve of material 100Cr6 obtained from standard compression test

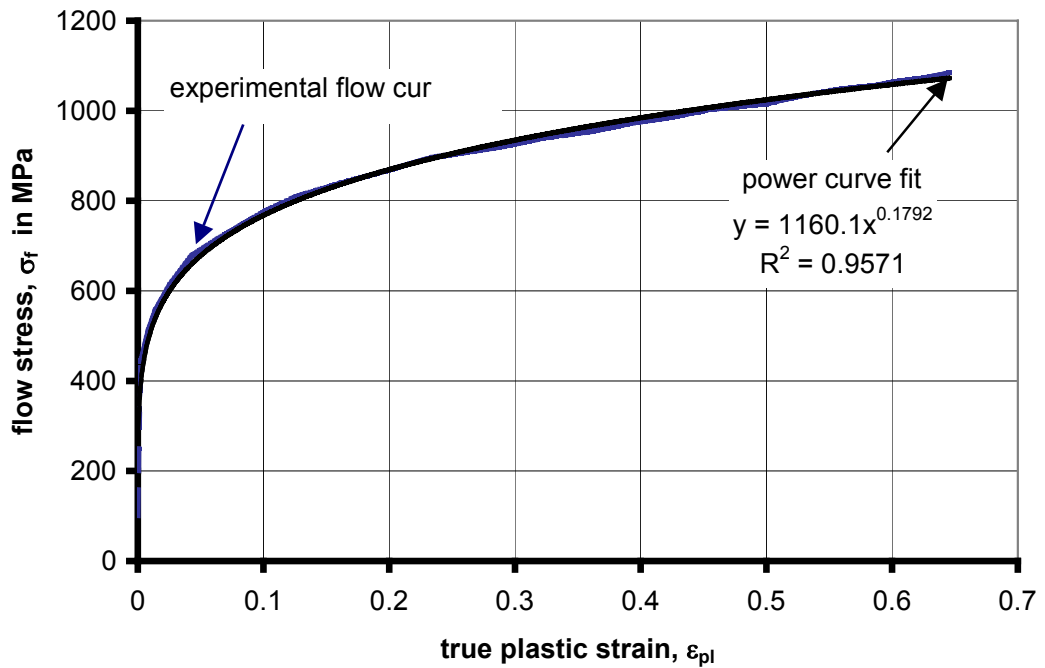
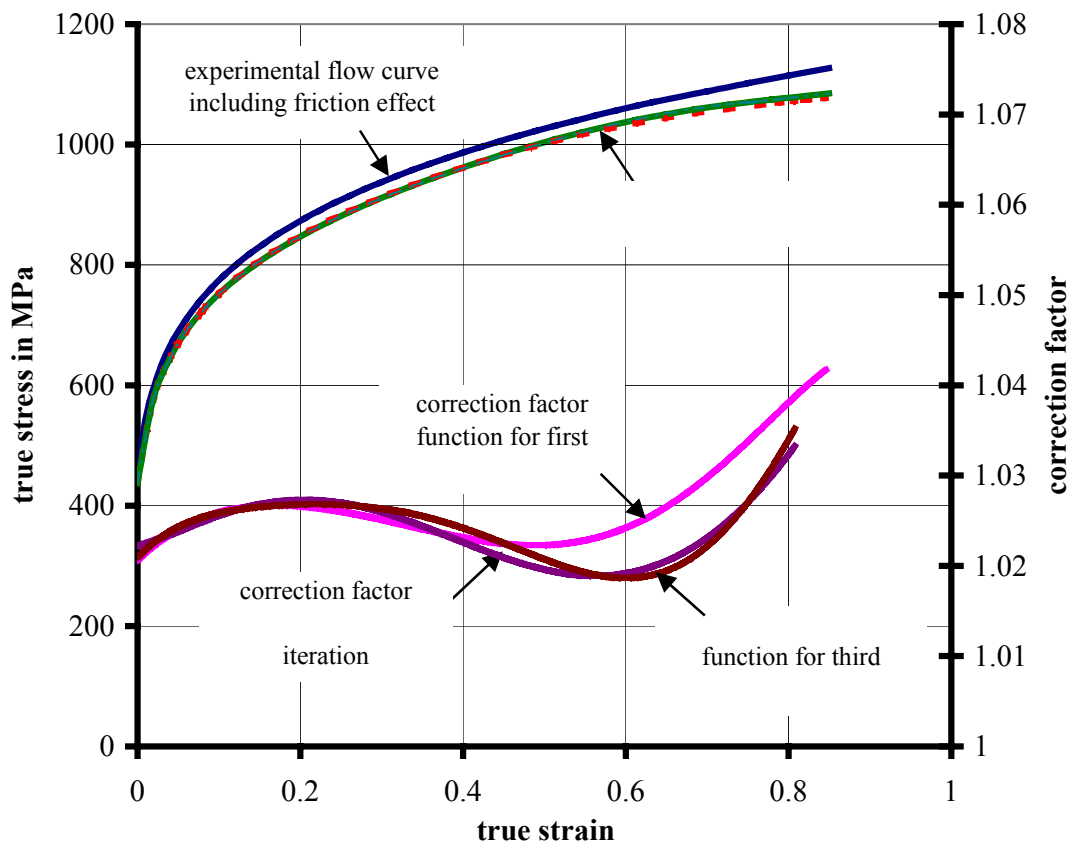


Figure 3.9 Experimental flow curve of 100Cr6 obtained from standard compression test and smooth power curve fit to it

Experimental compression flow curve includes the effect of friction and this effect can be subtracted by using iterative FEM method, for which detailed explanation is given in Section 2.4.2. Correction function of iterative FEM method is used to correct experimental flow curve up to maximum compression strain (about 0.75).

Iterative FEM method, which is explained in Section 2.4.2, is used in order to eliminate the effect of friction from the experimental flow curve.

For this method, the knowledge on the value of friction coefficient is required. Coulomb friction coefficient is accepted as  $\mu = 0.13$  from Section 3.4.1, in which ring experiments and FEM simulations are used to determine the friction coefficient.



**Figure 3.10** Application of iterative FEM (correction factor) method for first, second and third iterations

The correction factors for three iterations and corresponding corrected flow curves are shown in Figure 3.10 with the curve fit to experimental flow curve. It can be seen that even one iteration may be enough to have the corrected flow curve, as all three iterations result in very similar flow curves.

The flow stresses for the higher strain values can be obtained from the extrapolation of the corrected flow curve again by using Ludwik's equation. By fitting this equation in the whole range of flow data  $K$  and  $n$  values can be found 0.176 and 1229 MPa respectively as shown in Figure 3.11.

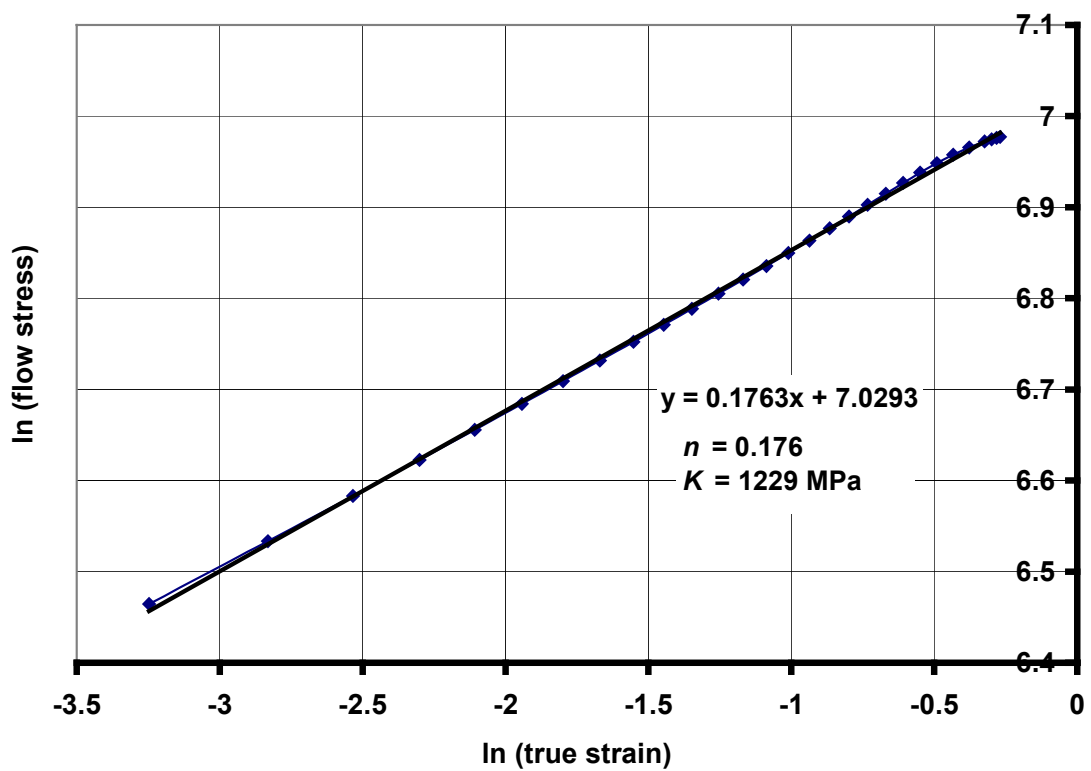


**Figure 3.11** Determination of  $n$  and  $K$  from the log-log plot of compressive flow curve

Corrected and extrapolated flow curve is shown in Figure 3.12 and can be compared with the experimental flow curve. It is seen that there exists approximately 5 % drop in flow stress when the correction is completed.

As a summary, final flow curves from tension and compression tests are shown in Figure 3.13. The reason of the difference in tensile and compressive flow curves may be the variation of material response to the loading in opposite directions. Another reason may be the extrapolation scheme used for both flow curves.

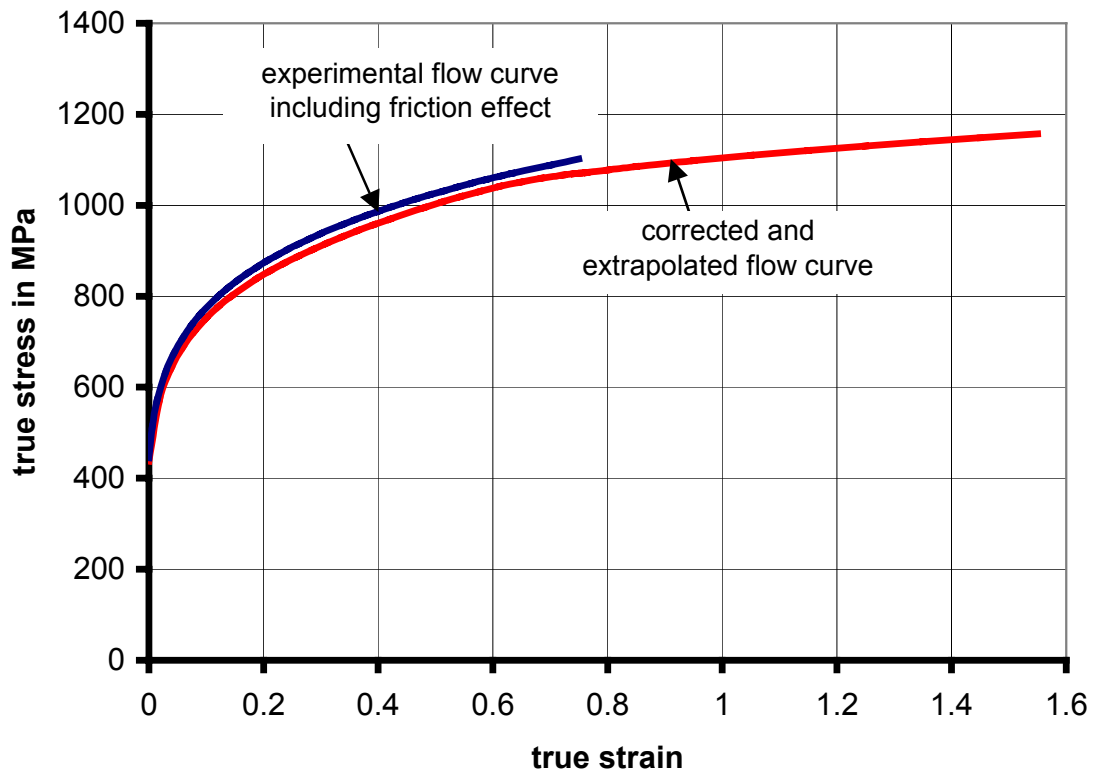


**Figure 3.12** Experimental compression flow curve and corrected & extrapolated final compression flow curve.

The tensile flow curve is used in tension test modeling, and the compressive flow curve is used in the modeling of various compression tests. As an input for FEM simulations, the flow curves are extrapolated to higher strains according to the maximum total effective strain induced by the various loading types of the modeled process.

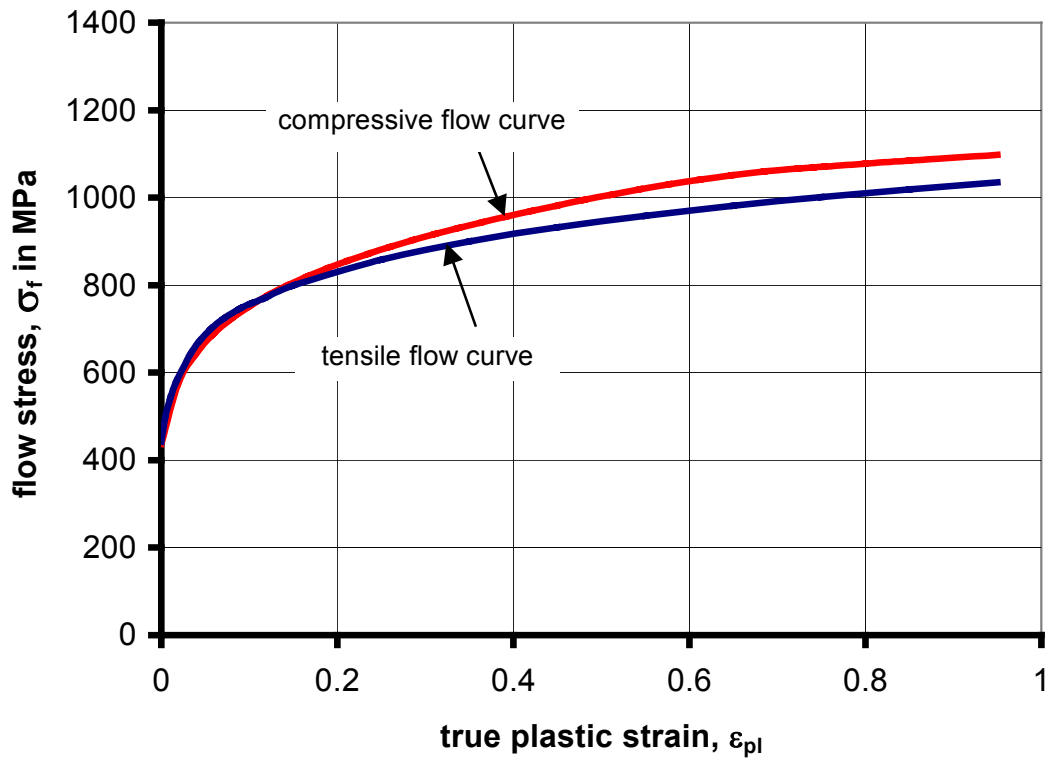


**Figure 3.13** Extrapolated flow curves of 100 Cr6 obtained from tension and compression tests

### 3.3 Performed Failure Experiments

Different forming processes create different stress paths in the workpiece. Loading type, workpiece and tooling dimensions, and other process parameters like the friction condition on the contact surfaces result differences on stress and strain path in the workpiece. The experiments must cover different load cases, ideally as much as possible. Tension and various compression tests are handled during the experimental study.

#### 3.3.1 Tensile Test

Tension tests specimens of 8 mm diameter and 50 mm gauge length were tested, using 40 tons Mohr&Federhaff hydraulic testing machine. Tests were repeated three times to obtain reliable results.

These results from the tension test are used both in obtaining tensile flow curve and in obtaining the minimum diameter of the neck region  $(d_{neck})_{min}$  when the specimen is fractured into two parts.

Designations for dimensions of initial and final geometries of a tension test specimen is given in Figures 3.1 and 3.14, where  $l_0$  is the initial gage length,  $d_0$  is the initial gage diameter,  $(d_{neck})_{min}$  is the minimum neck diameter at the fracture zone,  $l_f$  is the final gage length.

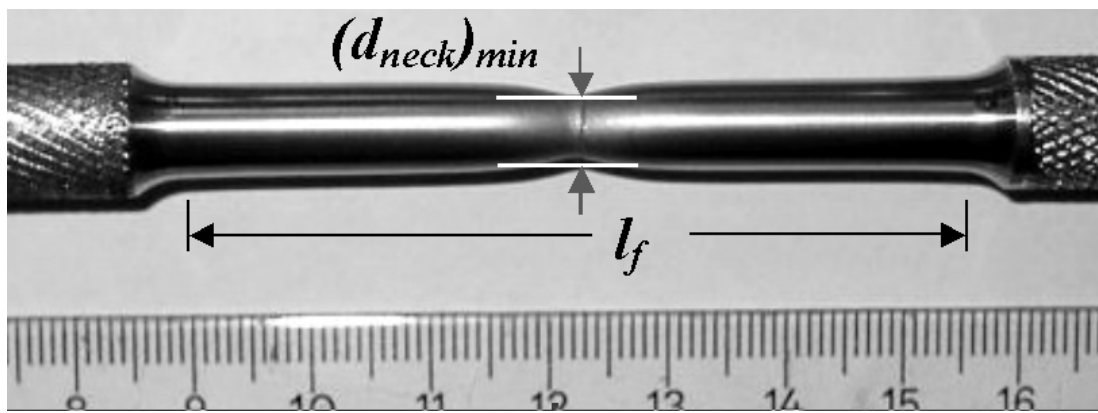


**Figure 3.14** Tension test specimens and related dimensions

Related dimensions of tension test specimens are given in Table 3.1.

**Table 3.1** Dimensions of tension test specimens in mm

	Specimen 1	Specimen 2	Specimen 3
$d_0$	8.03	8.04	7.99
$l_0$	52.02	52.14	51.9
$l_f$	65.3	65.2	65.5
$\Delta l$	13.28	13.06	13.6
$(d_{neck})_{min}$	5.1	5.12	5.08

### 3.3.2 Various Compression Tests

Specimens having different geometries are used for compression tests in order to create different stress states. Lubrication is not used in order to increase the barreling of the compressed specimens, so that the tensile stresses increase on the equator of the specimens, which accelerates the formation of surface cracks.

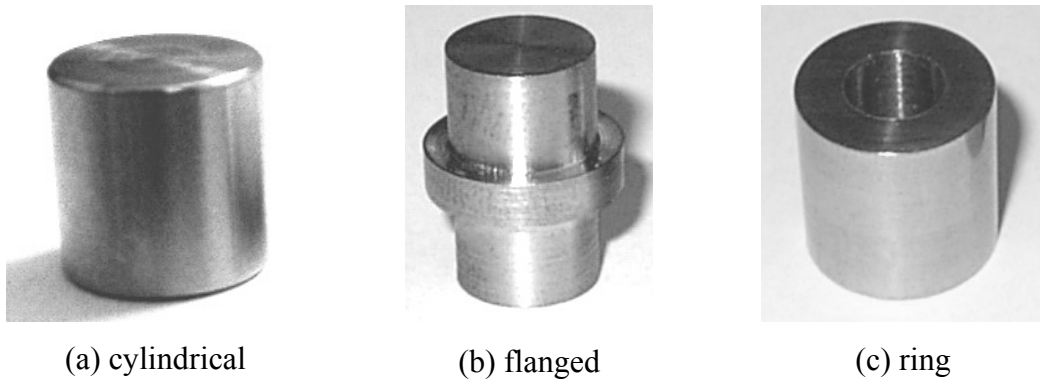


**Figure 3.15** Compression test specimens

Cylindrical, flanged and ring specimens (Figure 3.15) are compressed by using 40 tons Mohr&Federhaff hydraulic testing machine. Specimens are compressed until:

- A crack is visible with naked eyes or,
- The 40 tons loading limit of the hydraulic press is exceeded without any cracks of the specimen.

One of the problems arising during experimental investigations of ductile material failure is the exact determination of the time and the location of the possible damage. The exact detection of material damage with optical methods is time consuming. Stepwise compression tests must be carried out in order to determine visible cracks.

During the experiments, the press operator has usually felt the crack initiation time as a small change in load, but this change could not have been detected graphically on a press without digital output. In order to decrease the error on obtaining the

change in length of the specimen when the crack has just been visible, the press has been loaded as slow as possible.

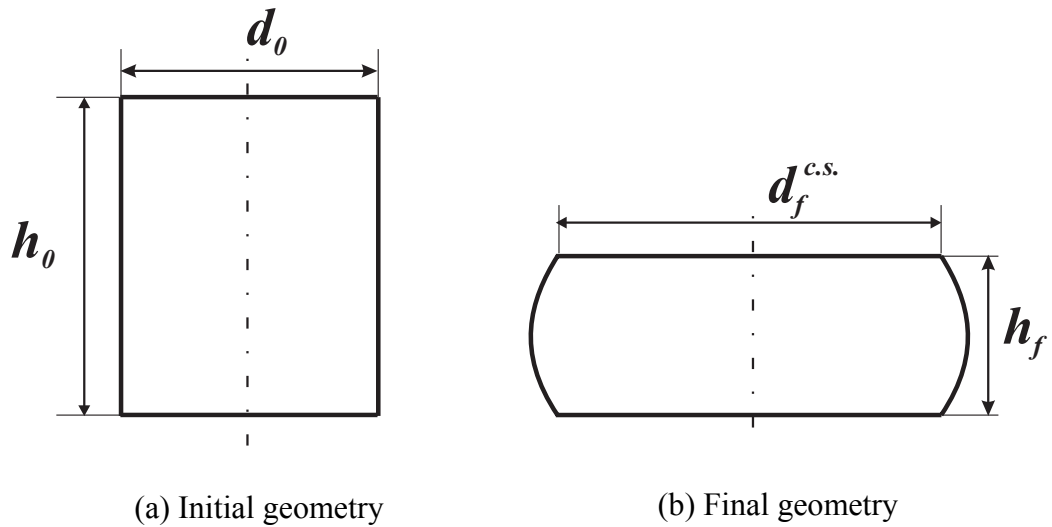


**Figure 3.16** Designations for dimensions of a standard compression test specimen

Designations for various dimensions of initial and final geometries of a standard compression test specimen is given in Figure 3.16, where  $h_0$  is the initial height,  $d_0$  is the initial diameter,  $h_f$  is the final height and  $d_f^{c.s.}$  is the final diameter of the both cracked and non-cracked specimens at die-workpiece contact surface. Related dimensions of standard compression specimens are given in Table 3.2.

**Table 3.2** Dimensions of standard compression specimens in mm

	Standard Comp. 1 (cracked)	Standard Comp. 2 (cracked)	Standard Comp. 3 (cracked)	Standard Comp. 4 (cracked)	Standard Comp. 5 (cracked)
$h_0$	12.04	10.06	10	12.04	10.48
$d_0$	8.08	8.06	6	7.06	7.04
$h_f$	3.12	2.42	2.3	2.94	2.16
$d_f^{c.s.}$	15.6	16.22	12.4	13.8	15.5

Dimensions are selected according to the loading capacity of the hydraulic press used. Specimen dimensions are decreased whenever more deformation is needed in order to observe a possible crack initiation (Figure 3.17).

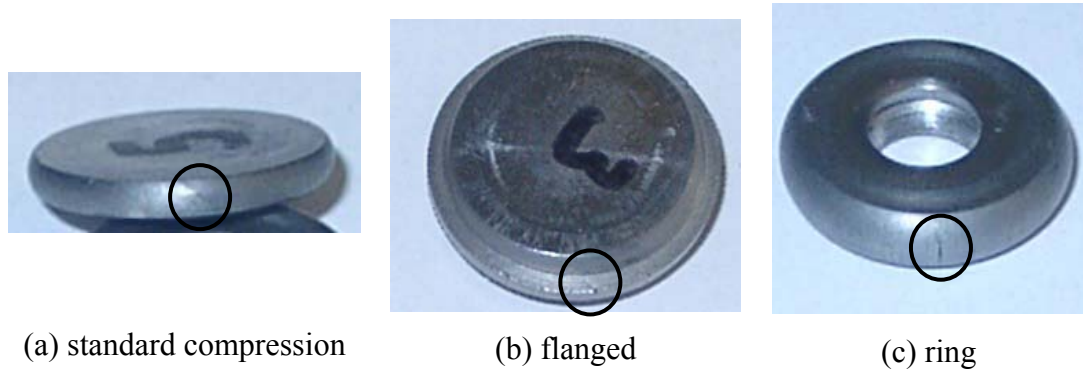


**Figure 3.17** Free surface crack examples from experiments

Designations for various dimensions of initial and final geometries of a flanged test specimen is given in Figure 3.18, where  $h_0$  is the initial height,  $d_0$  is the initial diameter,  $d_0^{flange}$  is the initial flange diameter,  $t_0^{flange}$  is the initial flange thickness,  $h_f$  is the final height and  $d_f^{c.s.}$  is the final diameter of the specimen at die-workpiece contact surface.

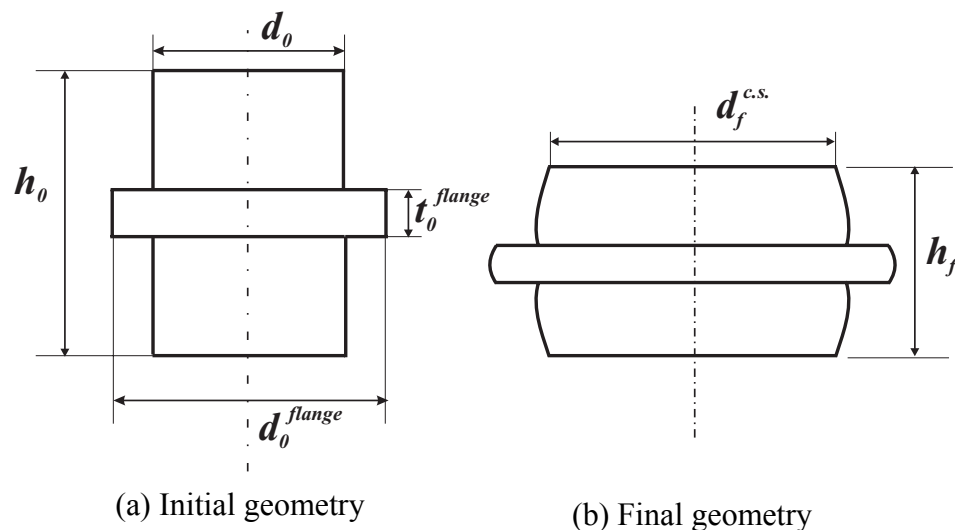


**Figure 3.18** Designations for dimensions of a flanged test specimen

Related dimensions of flanged specimens are given in Table 3.3.

**Table 3.3** Dimensions of flanged specimens in mm

Specimens:	Flanged 1	Flanged 2	Flanged 3
$h_0$	16.04	15.94	16
$d_0$	9.98	10	9.96
$d_0^{flange}$	13.12	13	12.06
$t_0^{flange}$	2.02	1.48	1.55
$h_f$	5.28	4.72	4.7
$d_f^{c.s.}$	16.64	17.6	17.8

Designations for various dimensions of initial and final geometries of a ring compression specimen is given in Figure 3.19, where  $h_0$  is the initial height,  $d_0^{out}$  is the initial outside diameter,  $d_0^{in}$  is the initial hole diameter,  $h_f$  is the final height and  $(d_f^{out})^{c.s.}$  is the final outside diameter of the specimen at die-workpiece contact surface.

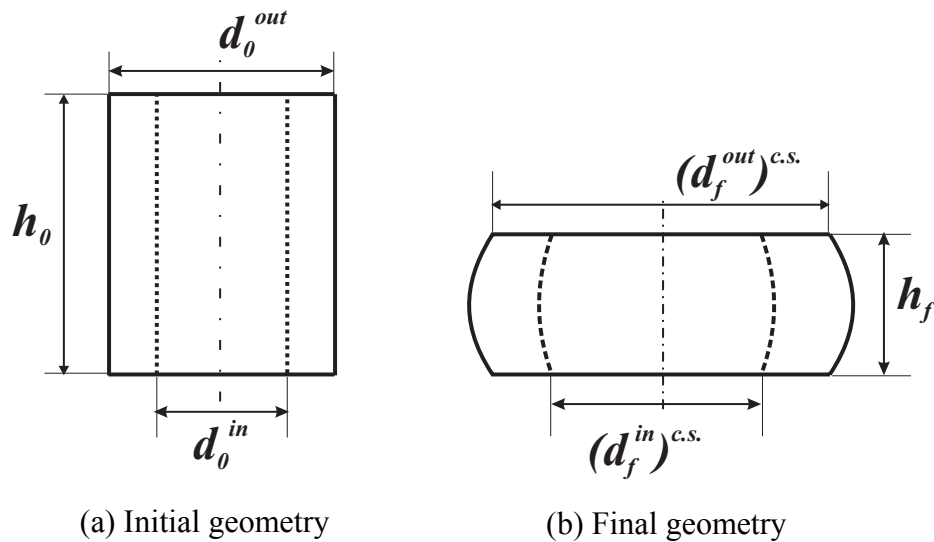


**Figure 3.19** Designations for dimensions of a ring test specimen

Related dimensions of ring specimens are given in Table 3.4.

**Table 3.4** Dimensions of ring specimens in mm

Specimen:	Ring 1	Ring 2	Ring 3	Ring 4
$h_0$	12.98	14.88	13.96	13.06
$d_0^{out.}$	13	15.02	10.84	10.82
$d_0^{in.}$	9	9	7	6.98
$h_f$	5.5	5.24	4.06	4.1
$(d_f^{out})^{c.s.}$	15.1	20.5	15.5	14.8

### 3.4 Modeling of Experiments

Modeling of the experiments by using finite element analysis is performed as a next step after the experiments. Friction factor prediction, iterative correction of compression flow curve and calculation of damage values at the critical regions of failure experiments require the outputs of finite element analysis.

FEM simulation program Deform 2D version 7.1 has been used throughout the modeling of experiments, including failure and friction analysis.

Due to the geometry of specimens, axisymmetric analyses are handled in all simulations.

Parameters and details of FEM simulations are tabulated in Table 3.5.

**Table 3.5** Parameters used in FEM simulations

<b>Bearing Steel</b>	<b>Analysis Options</b>	FEM Program	Deform 2D version 7.1		
		Iteration Method	Newton Raphson		
		Workpiece Material Type	Elastic-Plastic		
		Die Material Type	Rigid		
		Convergence Ratio	Force Error Limit: 0.01		
			Velocity Error Limit: 0.001		
		Penalty Factor	1e+12		
		Symmetry	Axisymmetric		
		Number of Elements	Tension	2000-3500	
			Standard	1500-3500	
			Flanged	1500-3500	
			Ring	1000-2500	
		Remeshing	Automatic & Performed when the distortion on an element is severe and also forced at each 20-30 steps		
		Number of Steps	100 – 500		
	Time per step	0.01-0.03 s			
	Punch velocity	1 mm/s			
	<b>Contact Control</b>	Friction Model	Coulomb		
		Friction Coefficient	0.13 (Mohr&Federhaff press)		
		Relative Sliding Velocity	Default		
	<b>Material</b>	Tension Test Modeling	Tension flow curve		
		Standard Flanged Ring	} Compression Modeling	Corrected (friction effect eliminated) compression flow curve	
		Modulus of Elasticity			210,000 MPa
		Poisson's Ratio	0.3		

### 3.4.1 Friction Factor Prediction

In the present study, the Coulomb friction coefficient, obtained from the ring test, is used to model the interface friction. In the ring test, ring-shaped specimens having the same dimensions are compressed down to different reductions.

Then, FEM simulations are done, using the same geometry with the experiments and selecting different values of Coulomb friction coefficients in the program.

The dimensions of ring test specimens, which are used for friction factor prediction, are given in millimeters in Table 3.6. Designations for ring specimens are given in Figure 3.19.

**Table 3.6** Dimensions of ring test specimens in mm

	Specimen 1	Specimen 2	Specimen 3
$h_0$	14.24	14.24	14.24
$d_0^{out.}$	14.02	14.02	14.02
$d_0^{in.}$	6.96	6.96	6.96
$h_f$	12.24	10.02	8.22
$(d_f^{in.})^{c.s.}$	7.00	7.00	6.99

It is explained in Section 2.5.3 that for a given height reduction during compression tests, the corresponding change of the internal diameter of the test specimen provides a quantitative knowledge of the magnitude of the friction coefficient at the die-workpiece interface. The results of FEM simulations are presented in the form of calibration curves, relating the reduction in the internal diameter of the test specimen to its reduction in height for varying values of the coefficient of friction. The

experimental data, each of which belongs to a specific height reduction, are represented as points on this graph. The nearest curve to the points of experimental data is selected to be representing the frictional behavior.

The friction condition obtained from the ring test is used for different purposes, one of which is to obtain the friction-free compression flow curve of the material, and other one is to add the friction effect correctly into a process modeled with the friction-free compression flow curve.

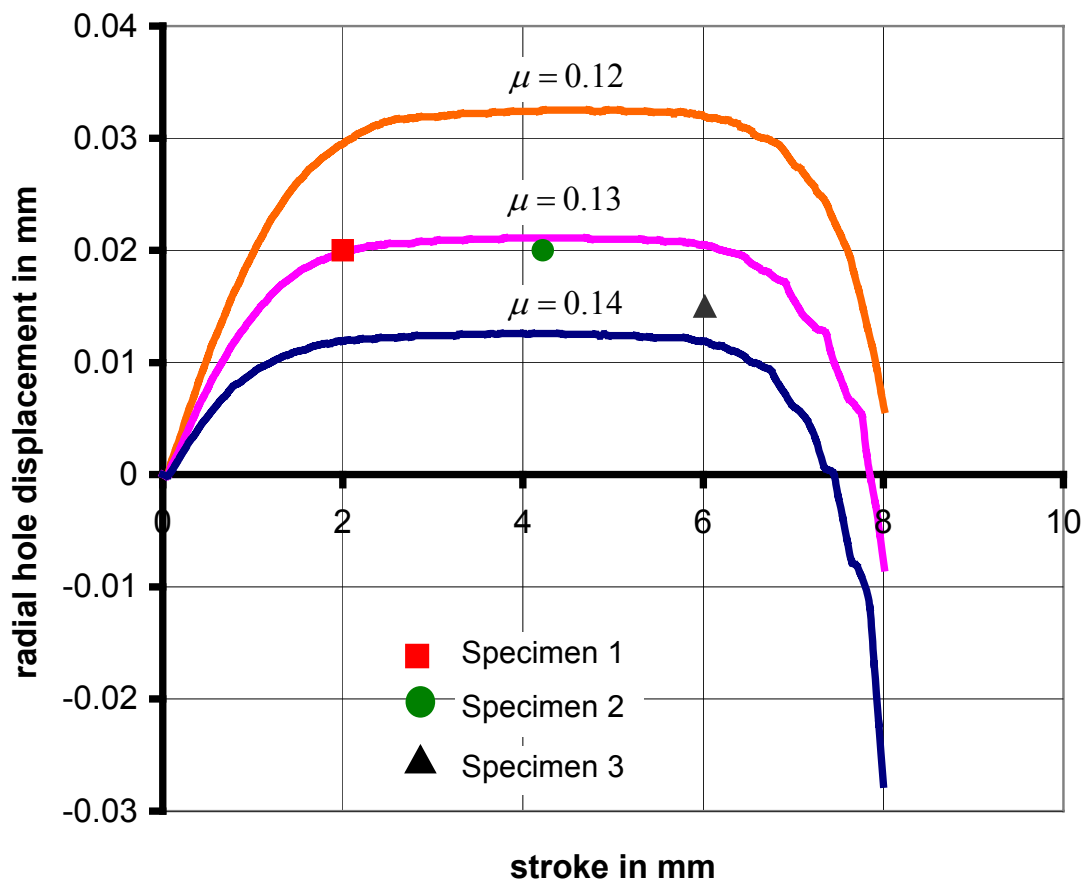


**Figure 3.20** Calibration curves by using experimental flow curve

In order to convert the experimental and friction-included compression flow curve to the friction-free compression flow curve, the friction effect to be deducted must be known. First, the friction coefficient is derived by using the experimental friction-

included flow curve. This method supplies us a pre-guess on the value of friction coefficient.

FEM simulations with different Coulomb friction coefficients supply the calibration curves, showing the radial hole displacement with respect to the stroke of the punch (Figure 3.20). Three ring test specimens, given in Table 3.6, represent the three experimental points of Figure 3.20. They show similar characteristics with the calibration curve of  $\mu = 0.13$ .

For the case represented in Figure 3.20, radial hole displacement is positive for all three specimens. This means that the hole diameter is getting larger with the applied compression stroke. By looking at the position of specimen 3, a friction coefficient greater than  $\mu = 0.13$  could have been found. The increase in friction for the case of specimen 3 may be caused by the folding of the material at die-workpiece interface.

Hole diameters are measured by using toolmaker's microscope with 0.001 mm accuracy and specimen heights are measured by using calipers with 0.02 mm accuracy. Since the change in hole radius of the specimens is used in Figure 4.10, the error in measurements is decreased to half. Although the measurements may still have small errors, they can be accepted accurate enough to decide on the friction coefficient with an accuracy of 0.01 in the value of the Coulomb friction coefficient.

Using this pre-guess value, FEM iteration method (correction factor method), which is explained in Section 2.4.2 and 3.2.2, is handled to obtain the friction-free compression curve. Then using this friction-free (corrected) flow curve, the ring test simulations are repeated to obtain the new calibration curve.

As the friction coefficient seems to be almost the same as the pre-guess value, this iteration method is accepted to be successful (Figure 3.21).

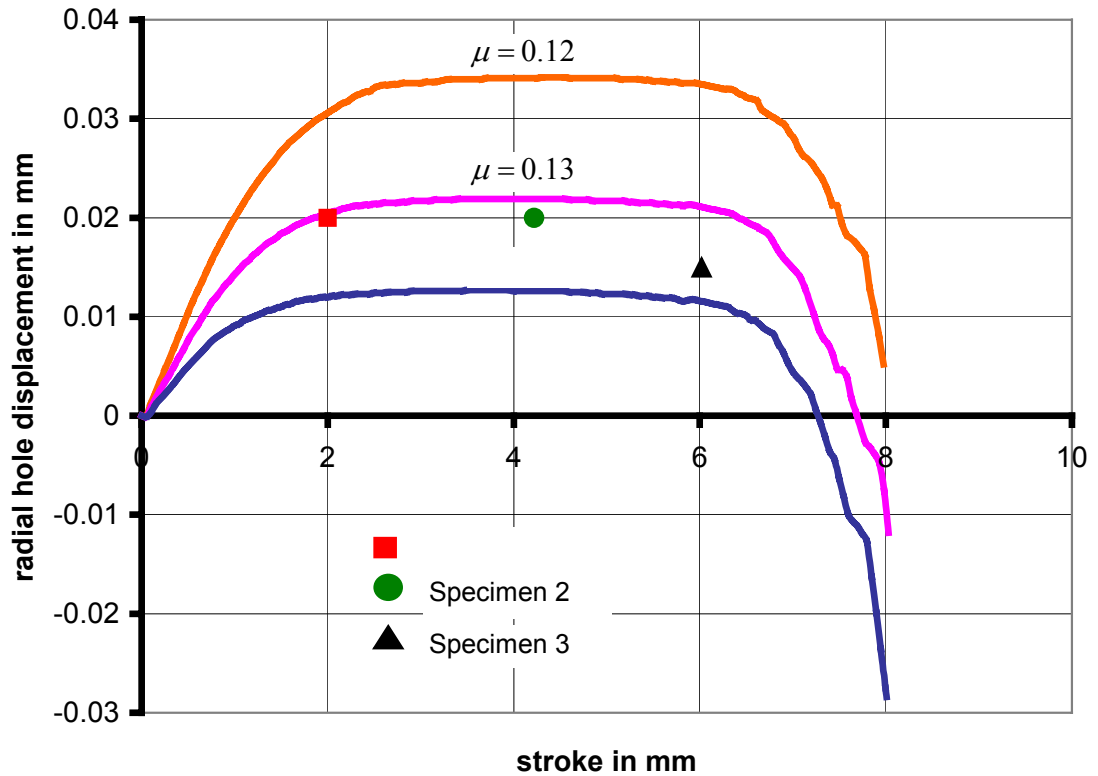


**Figure 3.21** Calibration curves by using corrected flow curve

### 3.4.2 Failure Experiments

In this section, FEM simulation results of failure experiments will be explained. Simulations are performed until the final dimensions of cracked or non-cracked specimens in experiments are arrived. Several criteria, explained in Sections 2.3.1, 2.3.2, 2.3.3 are used.

The correct prediction of the location and the first formation of a measurable crack are sought in the calculated results of the used criterion.

### 3.4.2.1 Tension Test Modeling

The modeled part of the tension test specimens, which is the quarter of axial cross-section, is shown in Figure 3.22.

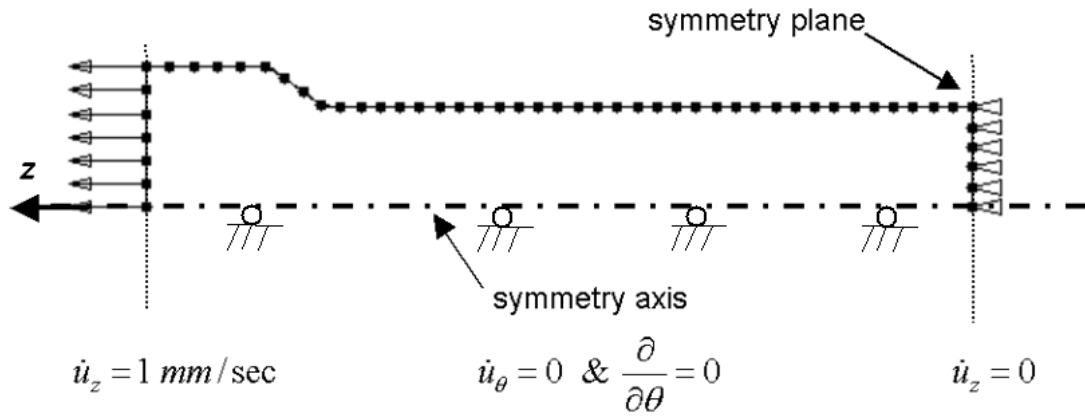


**Figure 3.22** Modeled part of tension test specimen

The simulation continues until the minimum neck diameter at the fracture zone, which was tabulated in Table 3.1, is reached. (Figure 3.23)

Crack initiation starts at the center of tension test specimens. This critical region, where the maximum damage values are sought, is also marked in Figure 3.23.

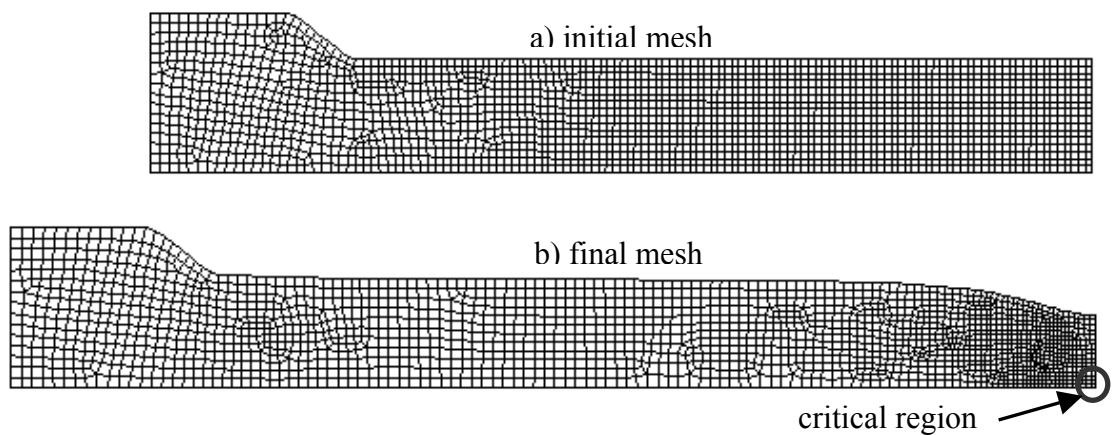


**Figure 3.23** Representative mesh and critical damage region

(Deform 2D version 7.1)

Figure 3.24 shows an example of the damage distribution for Cockroft-Latham criterion after tensile test. It can be seen that this criterion criticizes the center portion, where the crack initiates.

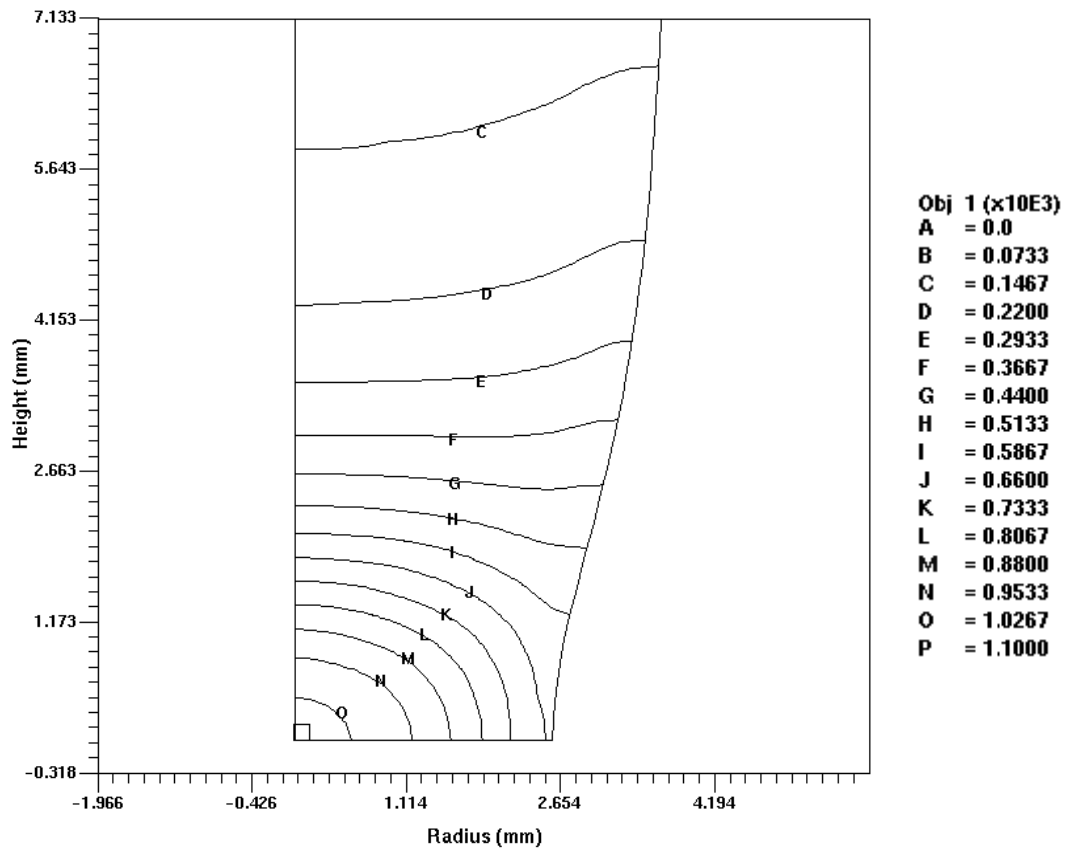


**Figure 3.24** Cockroft-Latham damage distribution at the middle section of gage length

The point where the damage value becomes maximum should be included in the region cracked in the experiment. Such criteria are said to be successful for detecting the critical region.

Damage calculations are done for all criteria used and the central critical damage values are noted in Table 3.7.

When the ‘maximum effective stress / ultimate tensile strength model’ was selected, the ultimate tensile strength has been defined as a constant, taken from the tensile engineering stress-strain data as  $\sigma_u = 647 \text{ MPa}$ .

**Table 3.7** Various criteria and their critical values, which become maximum at the center of fracture diameter

Criteria	Damage	Criteria	Damage
Freudenthal	855 MPa	Rice-Tracey	1.17
Cockroft-Latham	1050 MPa	McClintock	2.76
Normalized Cockroft-Latham	1.18	Effective stress/ UTS	2.23
Brozzo	1.18	Ayada	0.54

### 3.4.2.2 Compression Test Modeling

Due to the symmetry axis and symmetry plane of the compressed specimens, quarter parts of cross-sections are modeled in FEM analysis. The modeled parts of standard compression, ring and flanged specimens are shown in Figure 3.25.

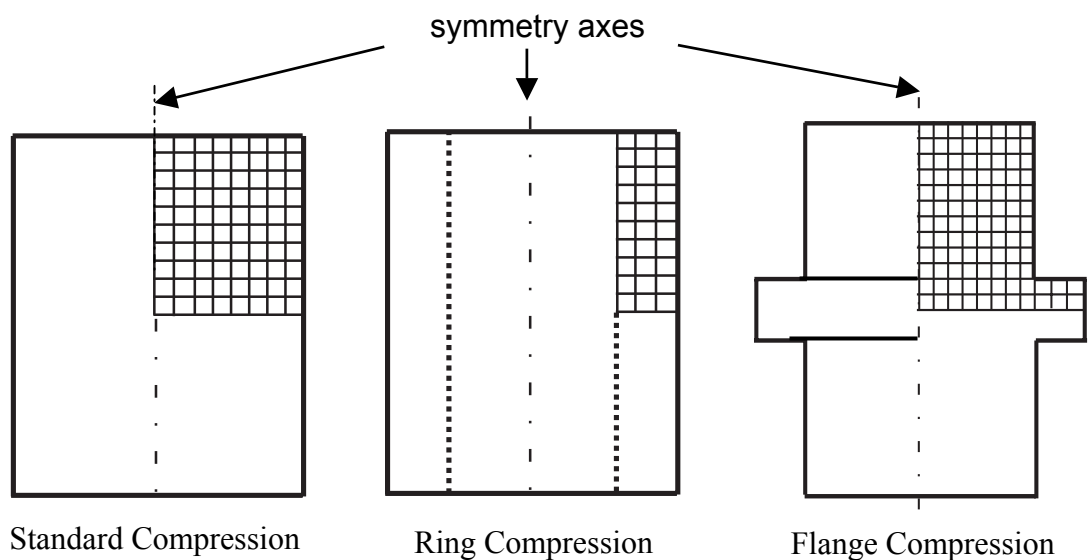


**Figure 3.25** Modeled parts of specimens

Each specimen, whose dimensions are given in Tables 3.2, 3.3, 3.4 and 3.6, is modeled and the displacement of the punch is limited according to the change of height,  $(h_0 - h_f)$ , of that specimen.

Cracked critical region for a standard compression specimen, for which the maximum value of damage is sought from the simulations, are shown in Figure 3.26.

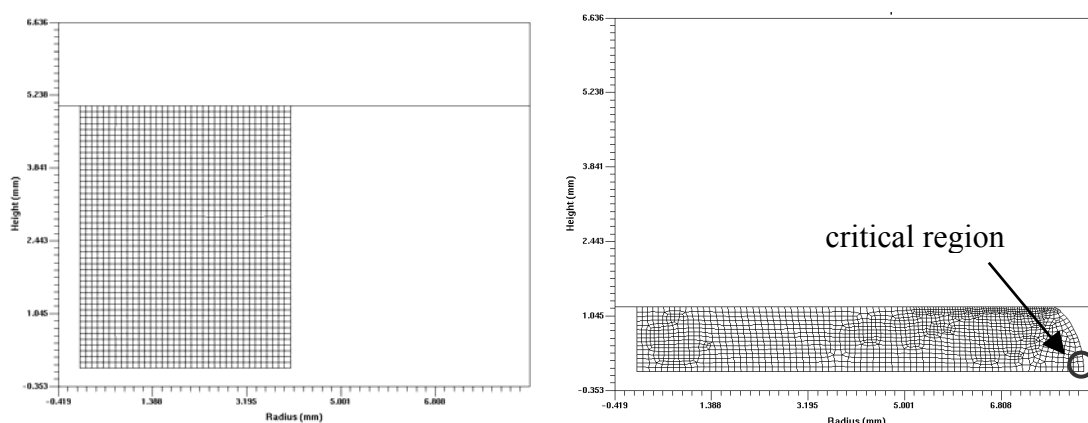


**Figure 3.26** Critical damage region for standard compression  
(Deform 2D version 7.1)

The critical damage values of various criteria for standard compression specimens given in Table 3.2 are tabulated in Table 3.8.

**Table 3.8** Various criteria and their critical values at crack regions

Damage criteria	Damage values				
	S.Comp.1 (cracked)	S.Comp.2 (cracked)	S.Comp.3 (cracked)	S.Comp.4 (cracked)	S.Comp.5 (cracked)
Freudenthal (MPa)	822	826	918	911	943
C-L ((MPa)	458	509	512	459	575
C-L Normalized	0.464	0.517	0.502	0.463	0.577
Brozzo	0.502	0.555	0.541	0.495	0.611
Max.Effective stress/ UTS	1.68	1.69	1.70	1.71	1.71
Ayada	0.079	0.096	0.095	0.082	0.117
Rice&Tracey	0.406	0.455	0.455	0.399	0.523
McClintock	0.66	0.758	0.76	0.647	0.885

Cracked critical region for a flange compression specimen, for which the maximum value of damage is sought from the simulations, are shown in Figure 3.27.

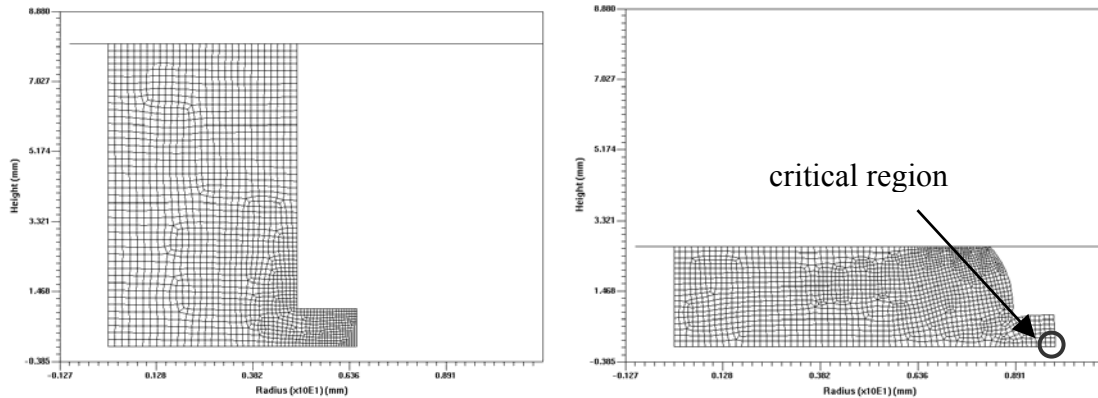


**Figure 3.27** Critical damage region for flange specimen (Deform 2D version 7.1)

The critical damage values of various criteria for standard compression specimens given in Table 3.3 are tabulated in Table 3.9.

Cracked critical region for a ring compression specimen, for which the maximum value of damage is sought from the simulations, are shown in Figure 3.28.

**Table 3.9** Various criteria and their critical values at crack regions

Damage criteria	Damage values	
	Flanged 1	Flanged 2
Freudenthal (MPa)	347	392
Cockroft-Latham (MPa)	364	400
C-L Normalized	0.44	0.488
Brozzo	0.443	0.475
Effective stress/ UTS	1.8	1.68
Ayada	0.045	0.117
Rice&Tracey	0.467	0.514
McClintock	0.922	0.99

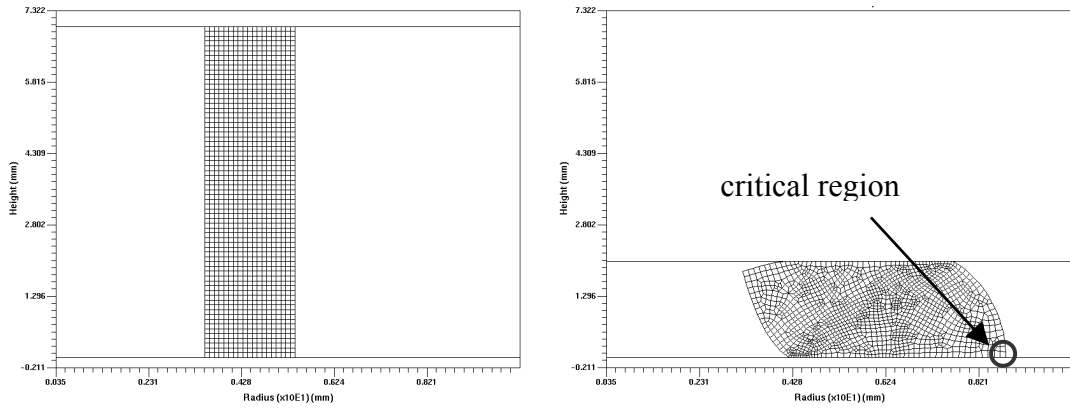


**Figure 3.28** Critical damage region for ring specimen (Deform 2D version 7.1)

The critical damage values of various criteria for ring specimens given in Table 3.4 are tabulated in Table 3.10.

**Table 3.10** Various criteria and their critical values at crack regions

Damage criteria	Damage values			
	Ring 1	Ring 2	Ring 3	Ring 4 (no crack)
Freudenthal (MPa)	468	368	517	389
Cockroft-Latham (MPa)	387	330	417	328
C-L Normalized	0.439	0.388	0.46	0.388
Brozzo	0.466	0.437	0.5	0.389
Effective stress/ UTS	2.13	1.52	1.61	1.52
Ayada	0.117	0.153	0.171	0.153
Rice&Tracey	0.404	0.371	0.426	0.358
McClintock	0.775	0.707	0.819	0.68

### The application of criterion by Oyane:

The criterion of Oyane, which was explained in Section 2.3.2, is applied here separately, as it requires the calculation of constant  $A$  of Eq. (2.23) experimentally.

Integral term  $\int_0^{\bar{\varepsilon}_f} \frac{\sigma_m}{\bar{\sigma}} d\bar{\varepsilon}$  of Eq. (2.24) is calculated and then plotted against  $\bar{\varepsilon}_f$  for

various specimens. This plot represents a linear relationship of  $y = mx + n$ .

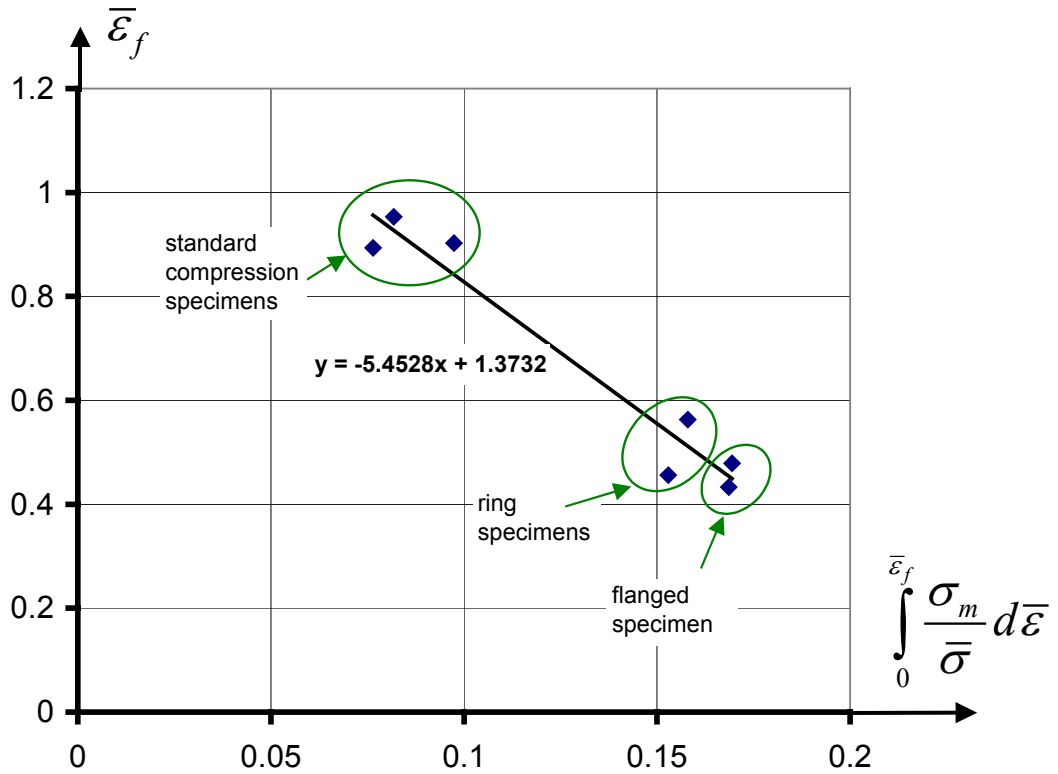


**Figure 3.29** Oyane criterion constant and critical value calculation

Therefore, material constant  $A$  can be obtained from the slope of the straight line,

$$A = -\frac{1}{m} = -\frac{1}{-5.4528} = 0.183$$

and material constant  $C$  from the intersection of the ordinate and this line,  $C = 1.3732$ .

Two cracked standard compression specimens, one cracked ring specimen and one non-cracked ring specimen are added to the Figure 3.29. It is seen that cracked part

stays over the trendline and the non-cracked specimen, for which lower effective strains than the critical effective strain is accumulated, stays below the trendline. (Figure 3.30)

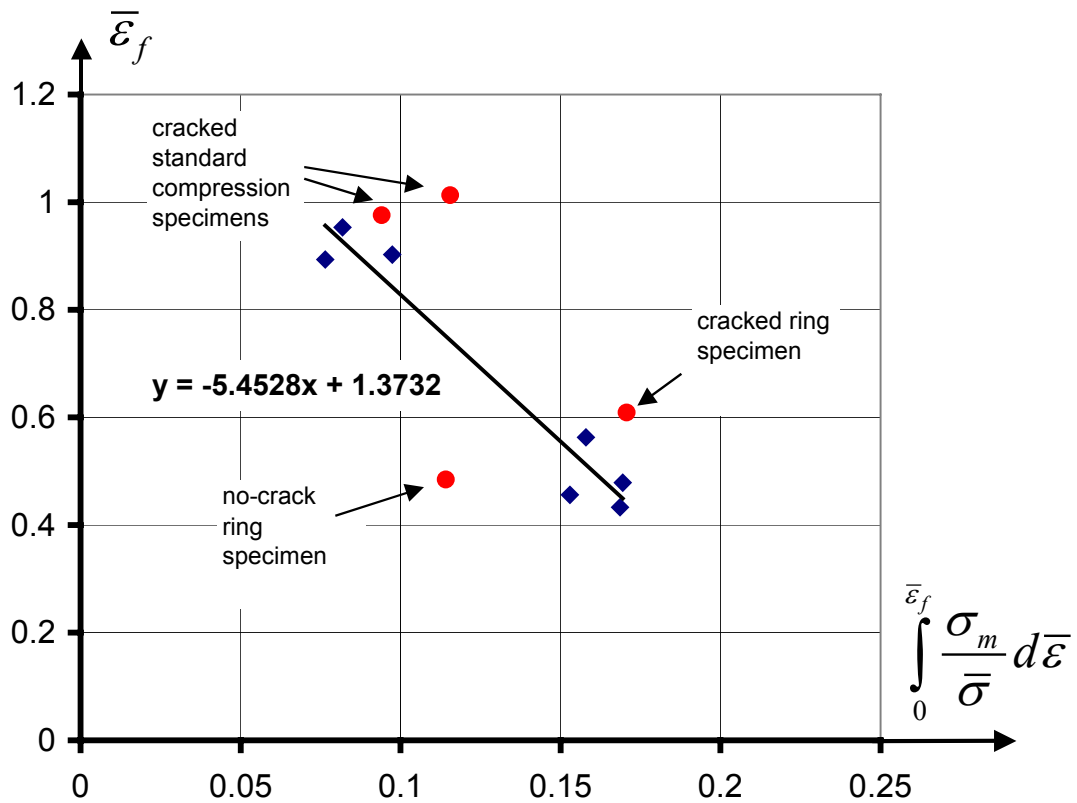


**Figure 3.30** Application for Oyane damage criteria

On the other hand, the trendline is a linear fit to the cracked specimens; some of the cracked specimens are left just below the trendline and some of them are left over the trendline. Therefore, it is critical to judge on a compressed specimen which is near to the trendline whether it will have cracks or not.

### 3.4.3 Stress Paths for Critical Regions

Stress paths followed by the critical points of tension and compression specimens are shown in Figure 3.31. The path for each curve starts at the origin and end points of the curves represent the stress state of corresponding cracked specimen.

For the critical point (equatorial point) of compression specimens,  $\sigma_2$  is the axial stress and  $\sigma_1$  is the circumferential stress, which is tensile.  $\sigma_2$  is compressive at the beginning for standard compression and ring compression specimens. When the barreling begins to be severe, axial compressive load is no longer carried by barreled surfaces and  $\sigma_2$  turns to be tensile accordingly.

For the tension specimens,  $\sigma_2$  is the circumferential stress and  $\sigma_1$  is the axial stress, which is tensile.  $\sigma_2$  is zero until the necking starts.

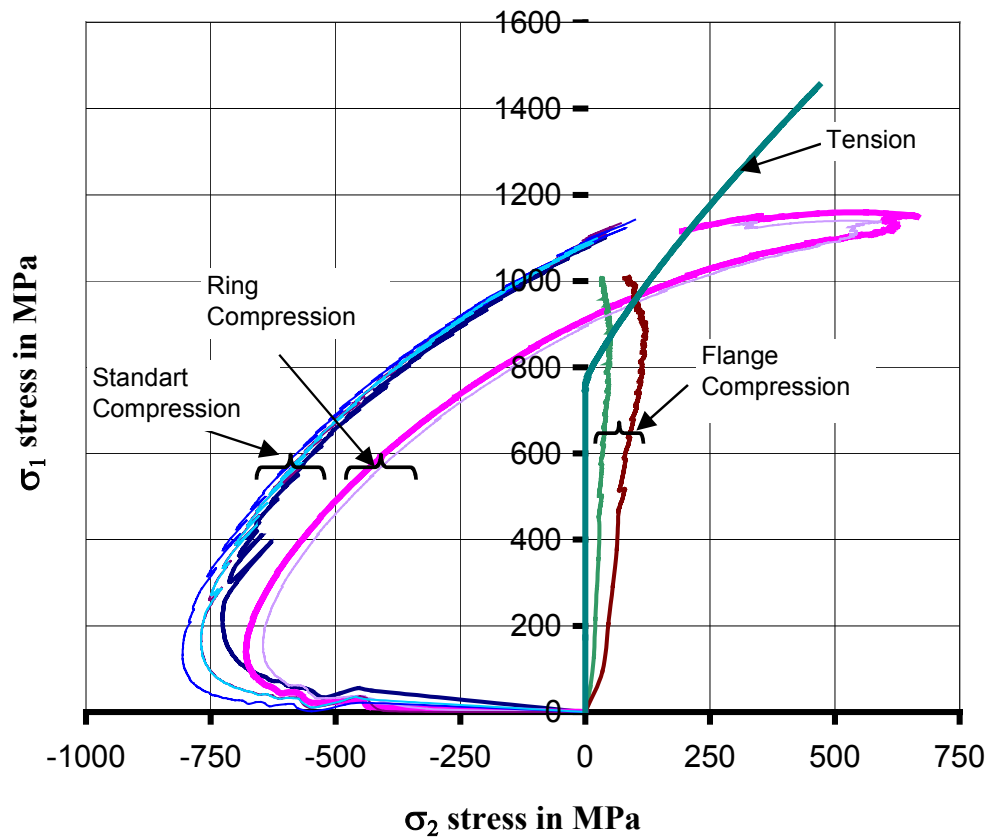


**Figure 3.31**  $\sigma_1$  vs.  $\sigma_2$  stress path for critical points

In the case of flange compression,  $\sigma_2$  is never compressive. Because the critical region, for which these stress path is drawn, is on the flange. Since the flange diameter is larger than the contact surface diameter, compressive axial stresses do not effect the flange region.

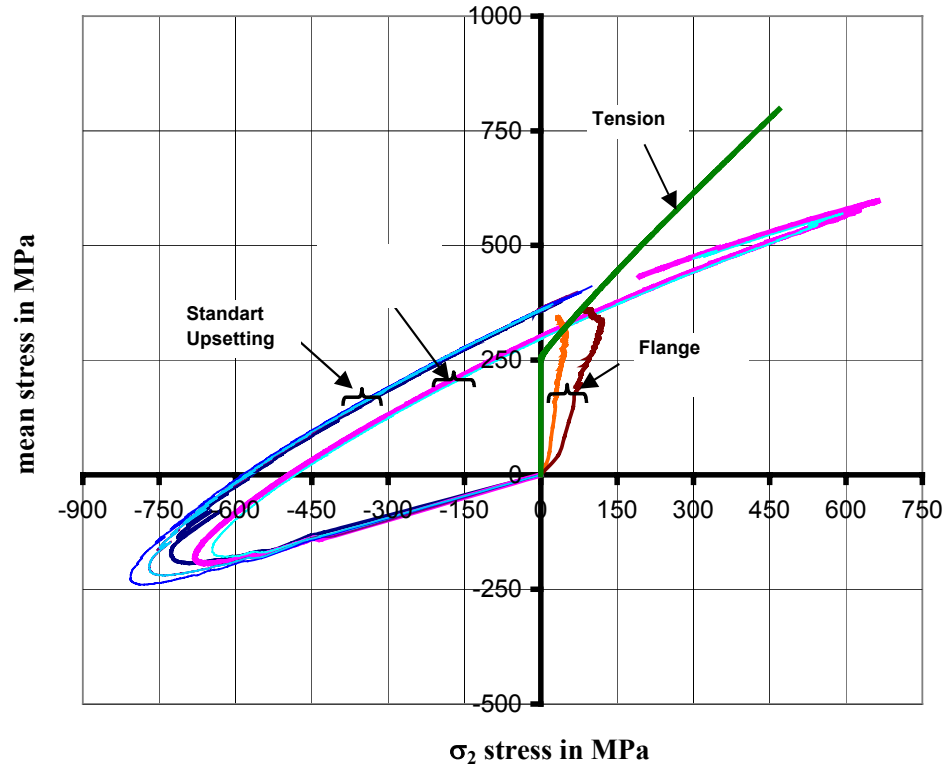


**Figure 3.32**  $\sigma_m$  vs.  $\sigma_2$  stress path for critical points

All the curves end when both stress components are positive. This shows the importance of tensile stress components on damage accumulation. Final  $\sigma_1$  is very similar when the ring and standard compression specimens are examined. Therefore the value of maximum effective stress may also be accepted as a critical value.

The paths of mean stress for the same specimens of Figure 3.31 are shown in Figure 3.32. Mean stress is negative at the beginning part for the ring and standard compression specimens. When the axial stress become more tensile, the mean stress turns to be positive for the critical points of these specimens.

It may be concluded that the distinction between the levels of the largest principal stress  $\sigma_1$  and that of the hydrostatic stress  $\sigma_m$  is not very important when characterizing free surface cracking because  $\sigma_1$  and  $\sigma_m$  usually increase or decrease together.

### 3.5 Discussions and Conclusions

The point where the damage value becomes maximum should be included in the region cracked in the experiment. Such a criterion is said to be successful for detecting the critical region.

All of the criteria used in damage calculations detect the critical central point of tension test specimens correctly. This is the same in compression specimens except the criterion of Freudenthal. This criterion detects an inner point as the most critical for compression specimens.

And the most successful criterion is the one that calculates same critical values for specimens, which have different geometries and create different stress-strain states.

When the Tables 3.7, 3.8, 3.9 are examined separately, the critical values in each row (the critical values of a single criterion for different compression specimens) seem to be similar, except the criteria of Ayada and Freudenthal, which supplies the greater variation.

When the Tables 3.7, 3.8, 3.9 are examined together, the critical values of a single criterion for standard, ring and flange compression specimens seem to be similar for the criteria of 'maximum effective stress / UTS', 'Brozzo', 'C&L Normalized' and 'Rice&Tracy'.

The critical damage values for tension specimens (Table 3.6) are above those of compression specimens (Tables 3.7, 3.8, 3.9) for all criteria. 'Maximum effective stress / UTS' criterion is the one that calculates most similar values among these criteria.

The Oyane criterion can also be used successfully for the processes where the primary stress is compressive.

## CHAPTER 4

### FORMABILITY ANALYSIS OF STAINLESS STEEL

#### 4.1 Introduction

In this chapter, the formability limits of austenitic stainless steel (X5CrNiMo1810) will be examined. First, the material flow curve is obtained. Then the results on failure experiments are given. The modeling of these experiments and an industrial case study are explained and the conclusions on the success of various failure criteria are presented.

#### 4.2 Obtaining Material Flow Curves

Tension and standard compression tests have been conducted in order to obtain the flow curve of stainless steel. These flow curves have been used in FEM simulations of the performed failure tests. The procedure and calculation methods for tension and compression tests are explained in Section 2.4.

##### 4.2.1 Tension Flow Curve

Tension test specimens (Figure 4.1) of 8 mm diameter and 40 mm gauge length have been tested at an average strain rate of  $1 \times 10^{-4} \text{ s}^{-1}$  using a 20-tons Zwick hydraulic testing machine.

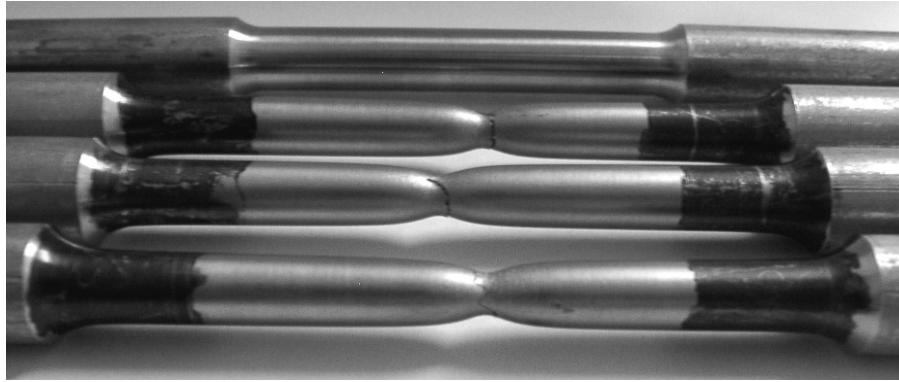


**Figure 4. 1** Stainless steel tension test specimens

Load displacement data, taken as a digital output from the press, has been converted to engineering stress – engineering strain data with the help of Eqs. (2.27), (2.28) and to true stress – true strain data with the help of Eqs. (2.32), (2.36).

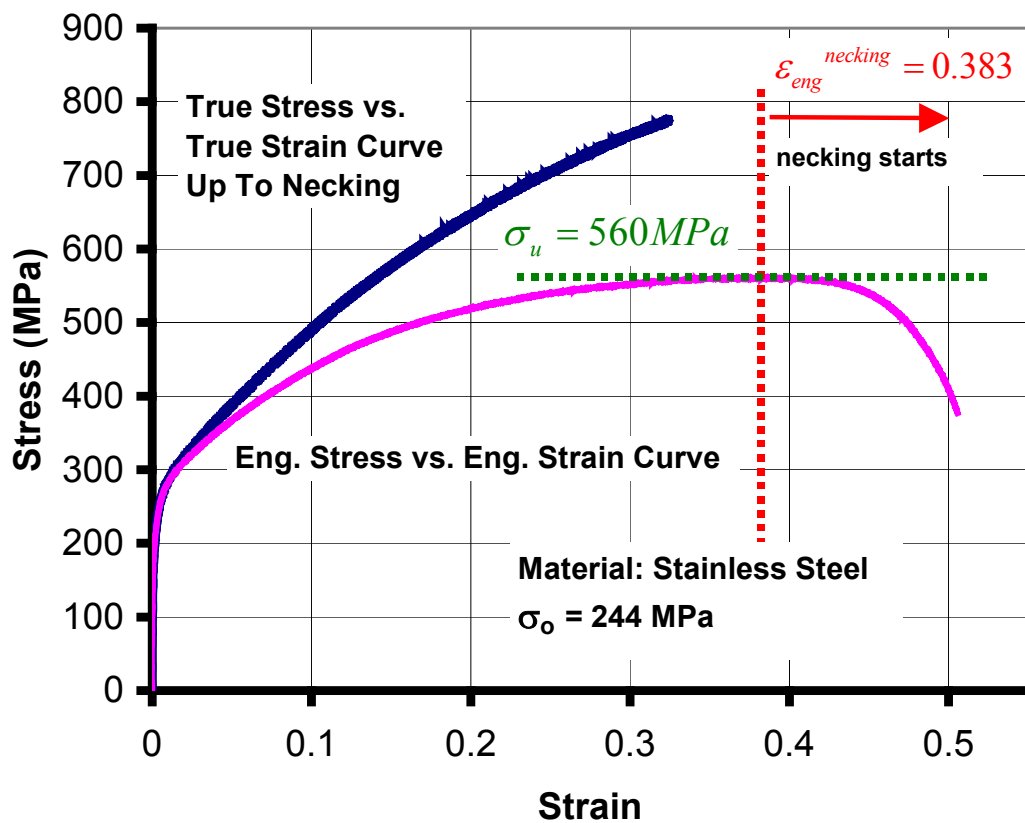


**Figure 4.2** Stress and strain curve of stainless steel obtained from tension test (Koçaker, 2003)

Maximum point on engineering stress – strain curve gives the point where the necking starts and the ultimate tensile strength,  $\sigma_u$  as shown in Figure 4.2. For the stainless steel specimen, ultimate tensile strength can be taken as  $\sigma_u = 560 \text{ MPa}$ , and necking strain as  $\varepsilon_{eng}^{necking} = 0.383$ .

From Figure 4.2 it can be seen that tension data is only available up to a total true strain value,  $\varepsilon_{true}$ , of 0.324. After this point, necking and therefore non-uniform elongation starts.

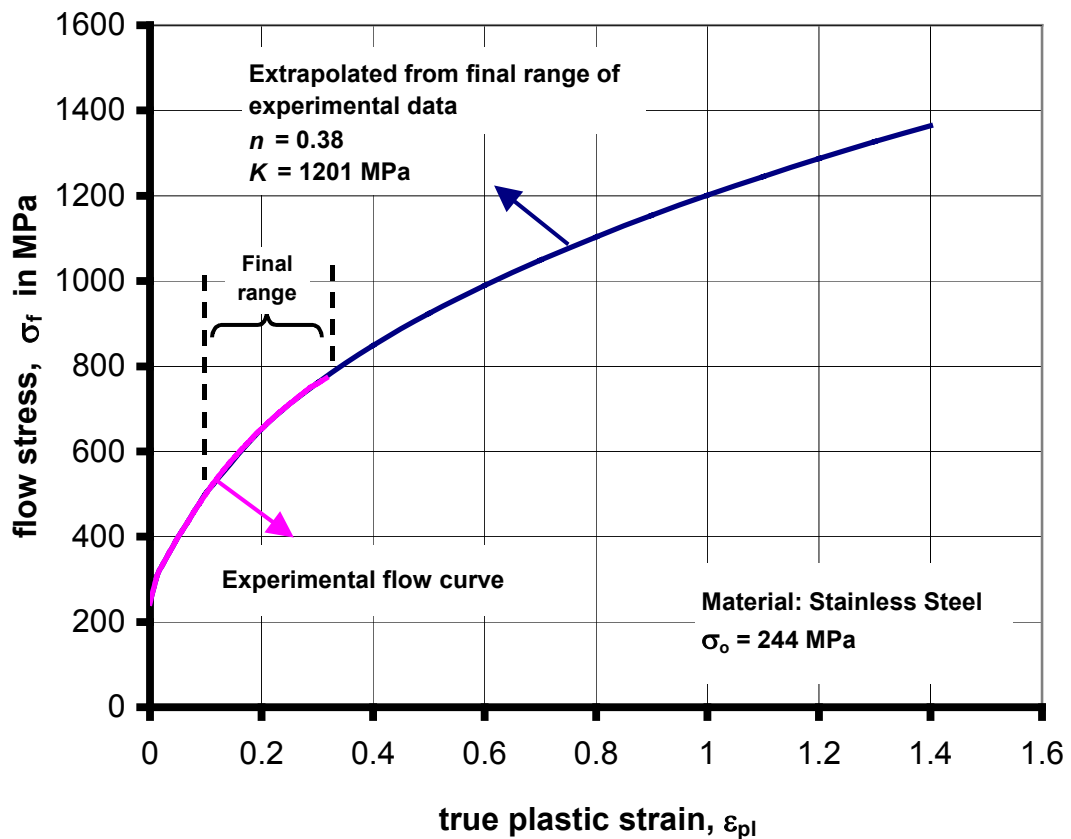


**Figure 4.3** Extrapolation for tension flow curve (Koçaker, 2003)

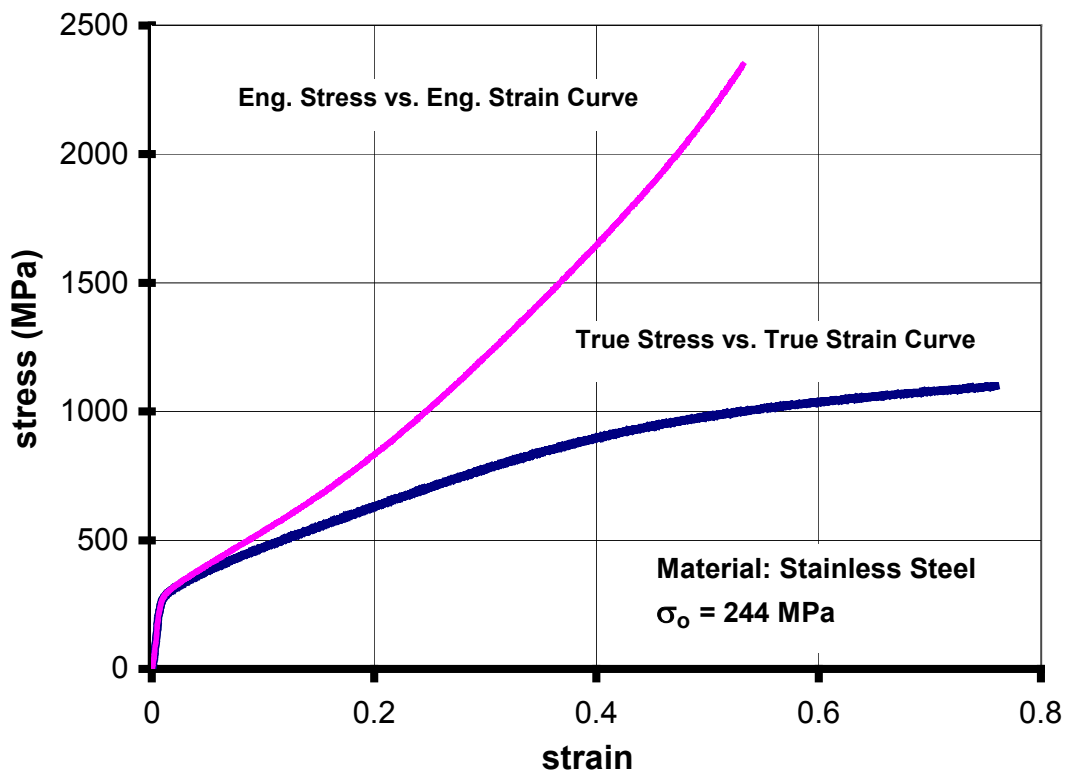
The flow curve can be obtained by plotting true stress values against corresponding equivalent true plastic strain values,  $\varepsilon_{pl}$ , determined by Eq. (3.1). The flow stress for higher strain values can be found by the extrapolation of the experimental flow curves by using Ludwik's law, given in Eq. (2.39) and Eqs. (3.3), (3.4).

Figure 4.3 shows the flow curve of stainless steel from tension test without any extrapolation and the Ludwik curve extrapolated with the specified  $n$  and  $K$  values.

The extrapolated flow curve with  $n$  and  $K$  values from the final region of the experimental flow curve represent the final region of experimental flow curve well. Final region is shown to be between total strain values of 0.07 and 0.31 in Figure 4.3. Therefore, the method to extrapolate the flow curve is to take the experimental flow curve and extrapolate the rest with  $n$  and  $K$  values obtained from the final range of flow data (Koçaker, 2003).

#### 4.2.2 Compression Flow Curve

Cylindrical specimens of 10 mm diameter and 15 mm height were compressed by using 20-tons Zwick hydraulic testing machine having an average strain rate of  $0.02 \text{ s}^{-1}$ .



**Figure 4.4** Stress and strain curve of stainless steel from standard compression test (Koçaker, 2003)

Load-displacement data can easily be converted to engineering stress – engineering strain data and to true stress – true strain data with the help of Eqs. (2.40), (2.42). These curves are represented in Figure 4.4. The yield stress is shown to be  $\sigma_0 = 244 \text{ MPa}$  (Figure 4.4).

It can be seen that compression data is available up to  $\varepsilon_{true} = 0.74$  due to the dimensions of the specimen used and the loading capacity of the hydraulic press.

Experimental compression flow curve includes the effect of friction and this effect can be subtracted by using iterative FEM method, for which detailed explanation is given in Section 2.4.2. Correction function of iterative FEM method is used to correct experimental flow curve up to maximum compression strain (about 0.74).

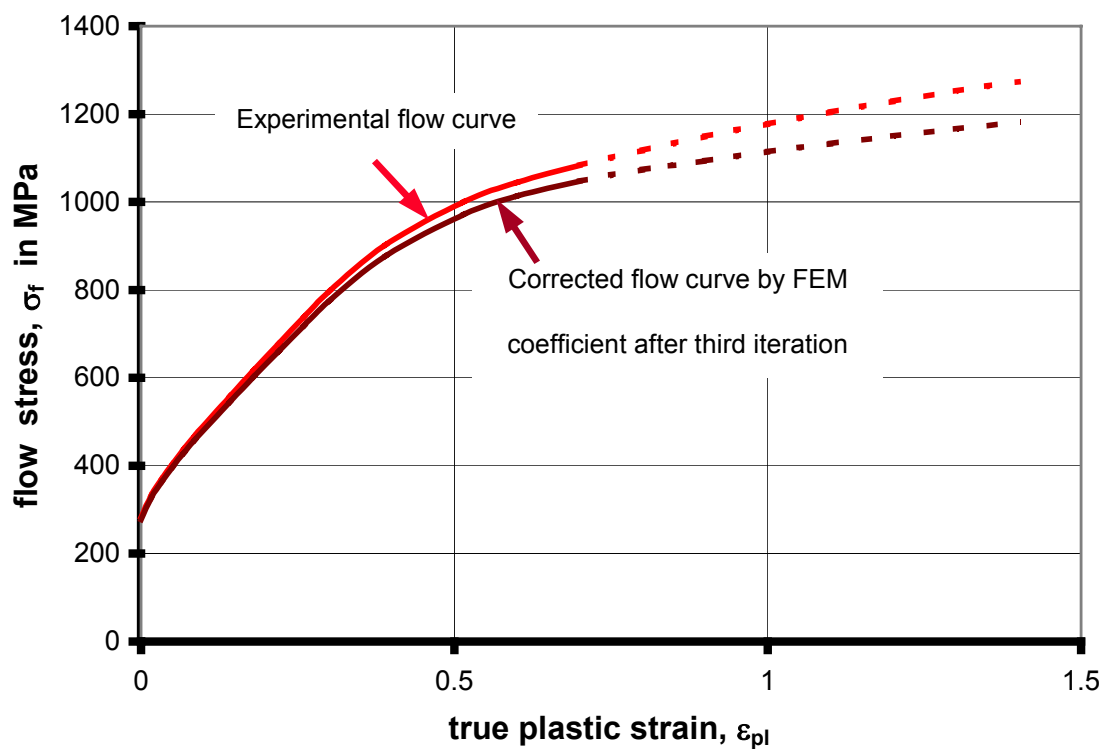


**Figure 4.5** Application of iterative FEM (correction factor) method for first and second iterations (Koçaker, 2003)

For this method, the knowledge on the value of friction coefficient is required. During the experiments for material flow curve characterization, upper and lower surfaces were polished and molybdenum disulfide (MoS<sub>2</sub>) was used as lubricant. Coulomb friction coefficient is accepted as  $\mu = 0.1$  from Section 4.4.1, in which ring experiments and FEM simulations are used to determine the friction coefficient.

The corrected flow curve is shown in Figure 4.5 and can be compared with the experimental flow curve. It is seen that there exists 5-10 % drop in flow stress when correction is completed. The dashed lines represent the Ludwik extrapolated region.

In order to make a comparison, flow curve from tension test is shown with corrected compression flow curve in Figure 4.6.

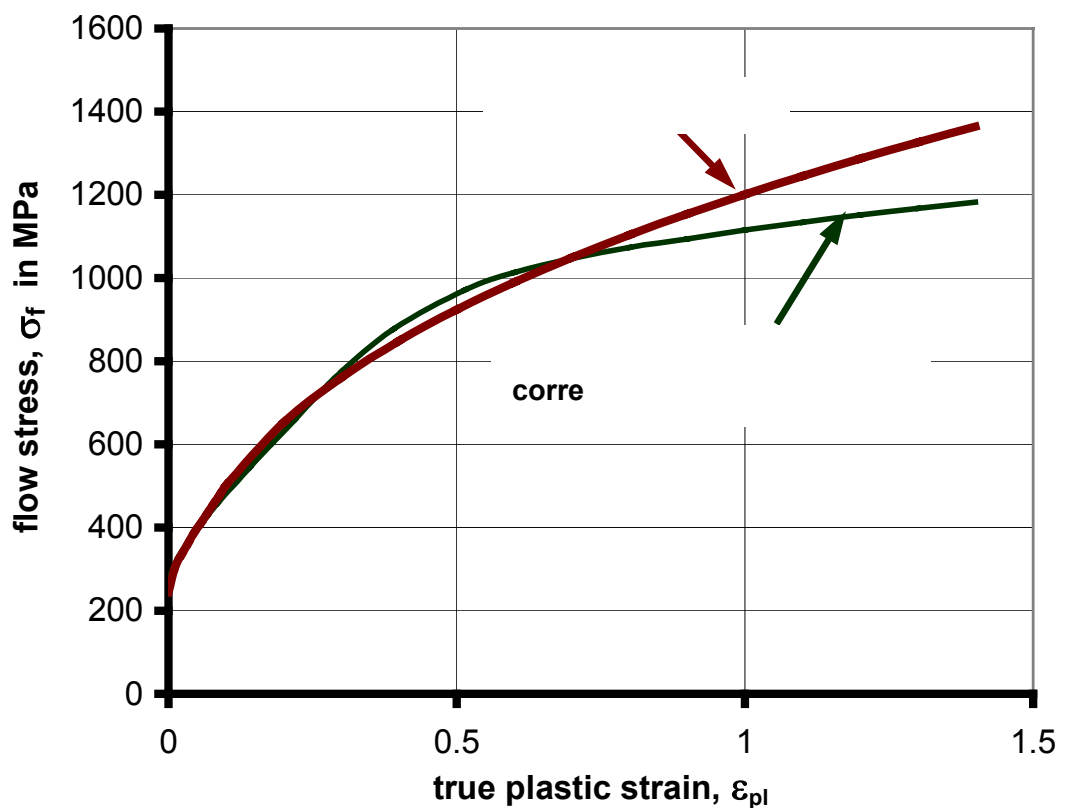


**Figure 4.6** Extrapolated flow curves of stainless steel obtained from tension and compression tests (Koçaker, 2003)

The reason of the difference in tensile and compressive flow curves may be the variation of material response to the loading in opposite directions. Another reason may be the extrapolation scheme used for both flow curves. The extrapolations are handled in a way to fit the slope of end parts of experimental flow curves, where the maximum total strains are reached in corresponding experiments. Therefore, the regions of experimental flow curves, that are used in the calculation of Ludwik extrapolation constants  $K$  and  $n$ , differ for tension and compression flow curves.

The tensile flow curve is used in tension test modeling, and the compressive flow curve is used in the modeling of various compression tests as an input for the material characterization.

### **4.3 Performed Failure Experiments**

Different forming processes create different stress paths in the workpiece. Loading type, workpiece and tooling dimensions, and other process parameters like the friction condition on the contact surfaces result differences on stress and strain path in the workpiece. The experiments must cover different load cases, ideally as much as possible. Tension and various compression tests are handled during the experimental study.

#### **4.3.1 Tensile Test**

Tension test specimens (Figure 4.1) of 8 mm diameter and 40 mm gauge length have been tested at an average strain rate of  $1 \times 10^{-4} \text{ s}^{-1}$ , using 200 kN Zwick hydraulic testing machine.

These results from the tension test are used both in obtaining tensile flow curve and in obtaining the minimum diameter of the neck region  $(d_{neck})_{min}$  when the specimen is fractured into two parts.

Designations for dimensions of initial and final geometries of a tension test specimen can be seen in Figures 3.1 and 3.14, where  $l_0$  is the initial gage length,  $d_0$  is the initial gage diameter,  $(d_{neck})_{min}$  is the minimum neck diameter at the fracture zone,  $l_f$  is the final gage length.

Related dimensions of tension test specimens are given in Table 4.1.

**Table 4.1** Dimensions of tension test specimens in mm

	Specimen 1	Specimen 2	Specimen 3
$d_0$	8	8	8
$l_0$	40	40	40
$l_f$	68	67	68
$\Delta l$	28	27	28
$(d_{neck})_{min}$	4.2	4.16	4.12

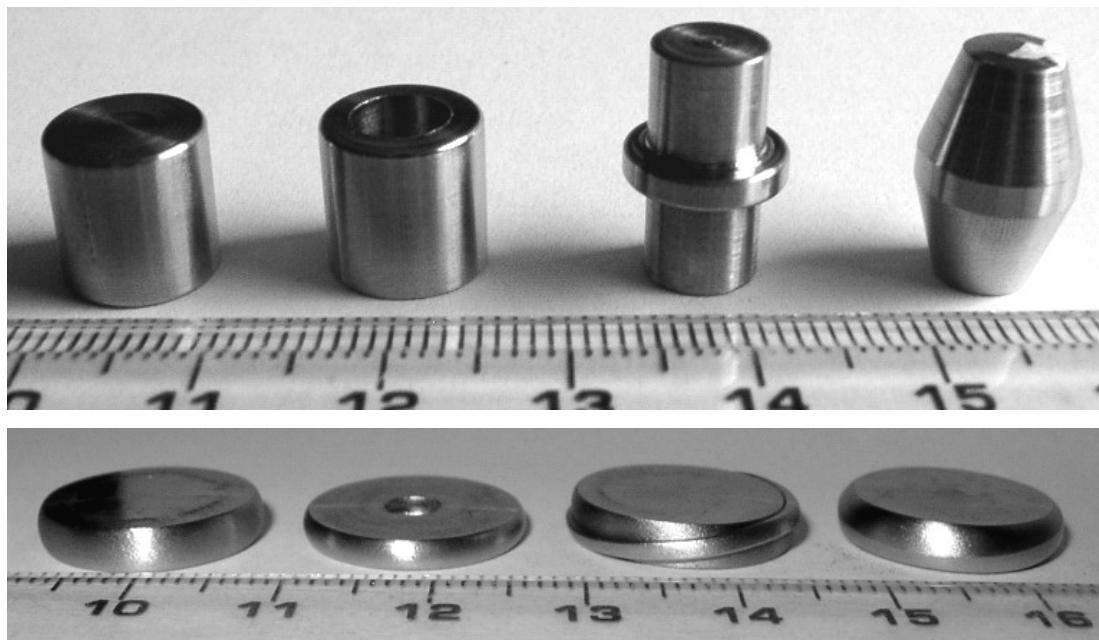
### 4.3.2 Various Compression Tests

Specimens having different geometries are used for compression tests in order to create different stress paths and hence states. Lubrication is not used in order to increase the barreling of the compressed specimens, so that the tensile stresses increase on the equator of the specimens, which accelerates the formation of surface cracks.

Cylindrical, flanged, ring and tapered specimens are compressed by using 40 tons Mohr&Federhaff hydraulic testing machine, having an approximate punch velocity of 0.05 mm/s and by using 200 kN Zwick hydraulic testing machine, having an approximate punch velocity of 0.2 mm/s. (Figure 4.7)

It is difficult to manufacture small tapered specimens (Figure 4.7), and therefore they are neither used in the formability analysis of bearing steel (Chapter 3) nor in the formability analysis of brass (Chapter 5).

Procedure for the compression of the specimens are explained in Section 3.3.2.



(a) standard                      (b) ring                      (c) flanged                      (d) tapered

**Figure 4.7** Stainless steel specimen geometries used in compression tests and examples of compressed specimens having no visible cracks

Crack initiation was not observed in these experiments, showing that the material has greater formability than the other two metals used in this study.

Designations for various dimensions of initial and final geometries of a standard compression test specimen is given in Figure 3.16, where  $h_0$  is the initial height,  $d_0$  is the initial diameter,  $h_f$  is the final height and  $d_f^{c.s.}$  is the final diameter of the specimen at die-workpiece contact surface. Related dimensions of standard compression specimens are given in Table 4.2.

**Table 4.2** Dimensions of standard compression specimens in mm

Using 40 tons Mohr & Federhaff hydraulic press	Specimens	$h_0$	$d_0$	$h_f$	$d_f^{c.s.}$
	Standard Comp. 1 (no crack)	10	10	3.58	16.0
	Standard Comp. 2 (no crack)	15	10	4.30	17.4
	Standard Comp. 3 (no crack)	15	10	4.48	17.3

Dimensions are selected according to the loading capacity of the hydraulic press used and the diameter of the annealed raw material used, which is about 11.5 mm.

Designations for various dimensions of initial and final geometries of a flanged test specimen is given in Figure 3.18, where  $h_0$  is the initial height,  $d_0$  is the initial diameter,  $d_0^{flange}$  is the initial flange diameter,  $t_0^{flange}$  is the initial flange thickness,  $h_f$  is the final height and  $d_f^{c.s.}$  is the final diameter of the specimen at die-workpiece contact surface. Related dimensions of flanged specimens are given in Table 4.3.

**Table 4.3** Dimensions of flanged specimens in mm

Hydraulic press used:	Mohr& Federhaff (40 tons)	Zwick (20 tons)		
Specimens:	Flanged 1	Flanged 2	Flanged 3	Flanged 4
$h_0$	15	15	15	15
$d_0$	8	8	8	8
$d_0^{flange}$	10	10	10	10
$t_0^{flange}$	2.1	2.1	2.1	2.1
$h_f$	3.58	5.08	5.26	5.2

The specimens are compressed by using either Mohr&Federhaff (40 tons) press at METU or Zwick (20 tons) press at Hilti. The initial experiments were handled by using Zwick and the surfaces of the press were lubricated. For the experiments on the Mohr&Federhaff hydraulic press, no lubrication is used.

The increased friction causes barreling and the stresses on the free equatorial surfaces become more tensile. Tensile stresses are known to increase damage at these points. Therefore the tendency of the free surfaces to crack initiation is increased.

For the modeling section of the current experiments (Section 4.4.2.2), two different Coulomb friction coefficients are used according to the press used for the modeled specimen. Corresponding friction coefficients are determined in Section 4.4.1.

Designations for various dimensions of initial and final geometries of a ring compression specimen is given in Figure 3.19, where  $h_0$  is the initial height,  $d_0^{out}$  is the initial outside diameter,  $d_0^{in}$  is the initial hole diameter and  $h_f$  is the final height.

Related dimensions of ring specimens are given in Table 4.4.

**Table 4.4** Dimensions of ring specimens in mm

Hydraulic press used:	Mohr&Federhaff (40 tons)			Zwick (20 tons)	
Specimen:	Ring 1	Ring 2	Ring 3	Ring 4	Ring 5
$h_0$	10	10	10	10	10
$d_0^{out.}$	10	10	10	10	10
$d_0^{in.}$	6	6	6	5	5
$h_f$	2.64	2.52	2.4	4.14	3.58
$(d_f^{out})^{c.s.}$	15.52	15.88	16.32	13.7	14.3

Designations for various dimensions of initial and final geometries of a tapered compression specimen is given in Figure 4.8, where  $h_0$  is the initial height,  $d_0^{contact}$  is

the initial contact surface diameter,  $d_0^{center}$  is the initial diameter at the equator of the specimen,  $t_0^{center}$  is the thickness of the center portion,  $d_f^{contact}$  is the final contact surface diameter and  $h_f$  is the final height.

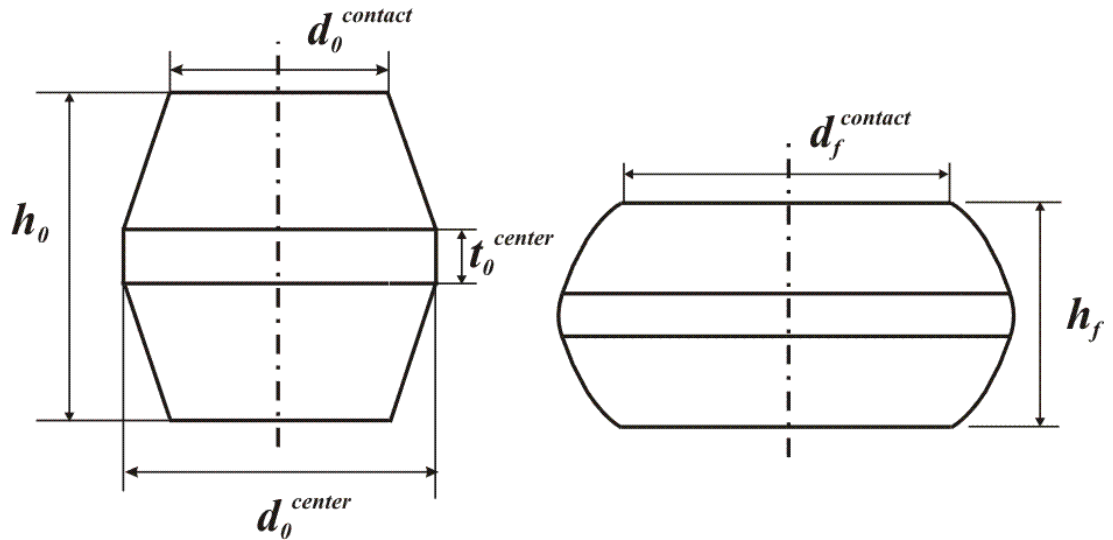


**Figure 4.8** Designations for dimensions of a tapered specimen

Related dimensions of tapered specimens are given in Table 4.5.

**Table 4.5** Dimensions of tapered specimens in mm

Hydraulic press used:	Mohr& Federhaff (40 tons)	Zwick (20 tons)	
Specimen:	Tapered 1	Tapered 2	Tapered 3
$h_0$	15	15	15
$d_0^{center}$	10	10	10
$d_0^{contact}$	6	6	6
$t_0^{center}$	2	2	2
$d_f^{contact}$	15.5	12.8	12.7
$h_f$	3.84	5.1	5.18

#### 4.4 Modeling of Experiments

Modeling of the experiments by using finite element analysis is performed as a next step after the experiments. Friction factor prediction, iterative correction of compression flow curve and calculation of damage values at the critical regions of failure experiments require the outputs of finite element analysis.

FEM simulation program Deform 2D version 7.1 has been used throughout the modeling of experiments, including failure and friction analysis.

Due to the geometry of specimens, axisymmetric analyses are performed in all simulations.

Figures 4.9, 4.10, 4.11 show the development of both maximum principle stress and mean stress with respect to the accumulated effective strain at the critical points of flanged, ring and tapered specimens, respectively.

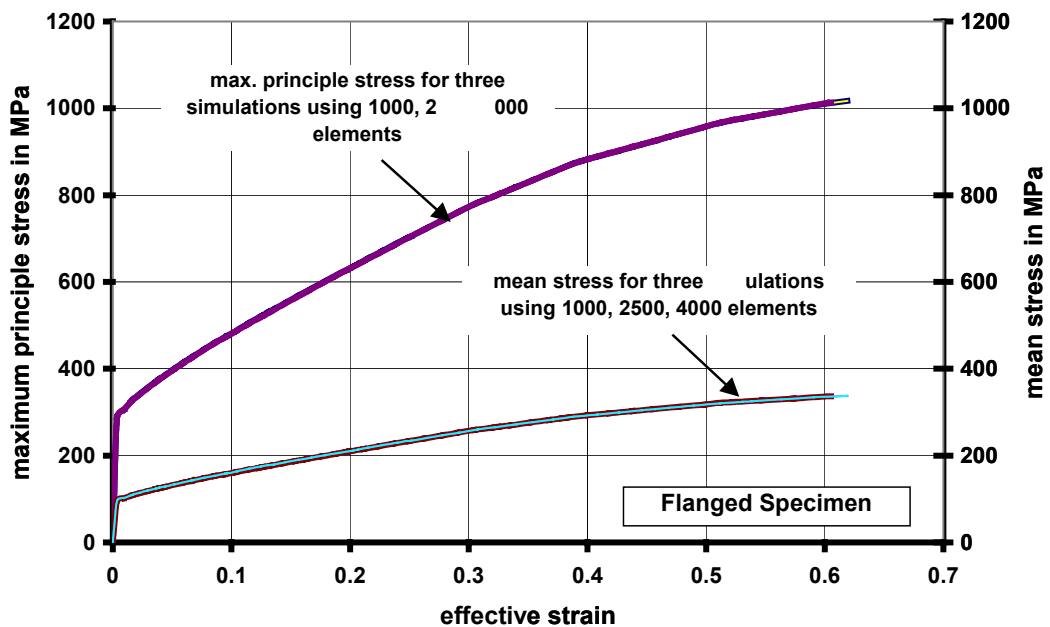


Figure 4.9 Convergence study (w.r.t. element number) in flanged specimen models

It is seen in this convergence study that, the FEM models using different number of elements (minimum 800 and maximum 4000 elements) supply very close stress-strain data for the calculation of damage values at the critical points.

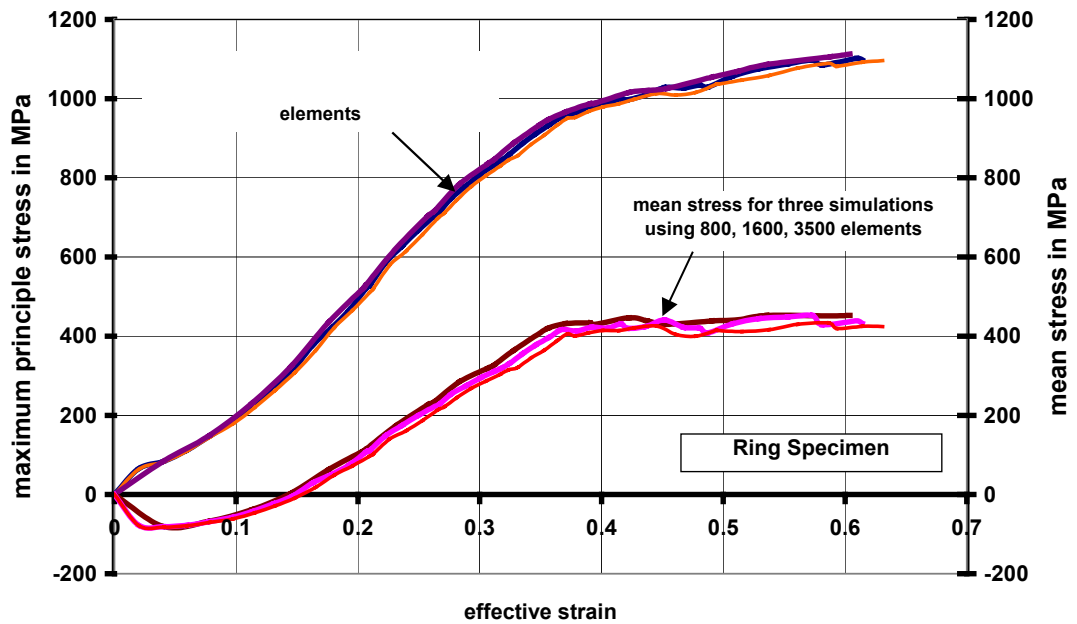


Figure 4.10 Convergence study (w.r.t. element number) in ring specimen models

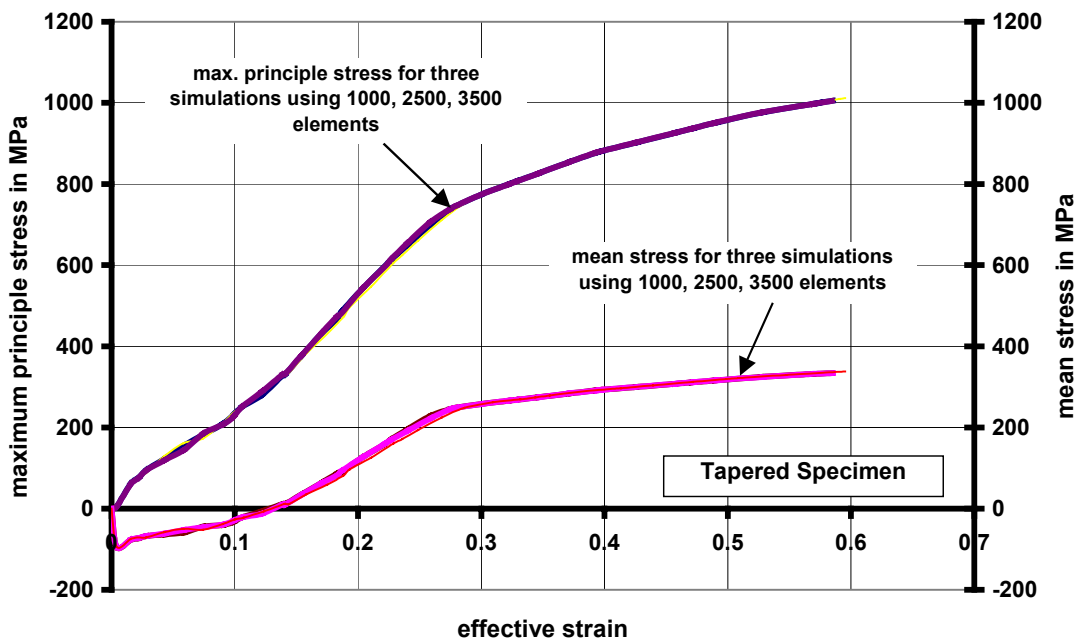


Figure 4.11 Convergence study (w.r.t. element number) in tapered specimen models

**Table 4.6** Parameters used in FEM simulations

<b>Stainless Steel</b>	<b>Analysis Options</b>	FEM Program		Deform 2D version 7.1	
		Iteration Method		Newton Raphson	
		Workpiece Material Type		Elastic-Plastic	
		Die Material Type		Rigid	
		Convergence Ratio		Force Error Limit: 0.01	
				Velocity Error Limit: 0.001	
		Penalty Factor		1e+12	
		Symmetry		Axisymmetric	
		Number of Elements		Tension	2000-3500
				Standard	1500-3500
				Flanged	1500-3500
				Ring	1000-2500
				Tapered	1500-2500
		Remeshing		Automatic & Performed when the distortion on an element is severe and also forced at each 20-30 steps	
		Number of Steps		100 – 500	
	Time per step		0.01-0.03 s		
	Punch velocity		1 mm/s		
	<b>Contact Control</b>	Friction Model		Coulomb	
		Friction Coefficient		0.1 (Zwick press)	
				0.21 (Mohr&Federhaff press)	
	Relative Sliding Velocity		Default		
	<b>Material</b>	Tension Test Modeling		Tension flow curve	
		Standard	}	Compression Modeling	Corrected (friction effect eliminated) compression flow curve
		Flanged			
		Ring			
		Tapered			
Modulus of Elasticity		210,000 MPa			
Poisson's Ratio		0.3			

The maximum principle stress and mean stress is investigated with respect to effective strain, since many failure criteria use these data in order to calculate damage values by taking integrals with respect to effective strain.

Parameters and details of FEM simulations are tabulated in Table 4.6.

#### 4.4.1 Friction Factor Prediction

The necessity and procedure for obtaining the friction coefficient are mentioned in Sections 2.5.3 and 3.4.1.

**Table 4.7** Dimensions of ring test specimens in mm

	Specimen 1	Specimen 2	Specimen 3
$h_0$	14.6	14.6	14.6
$d_0^{out.}$	10	10	10
$d_0^{in.}$	5	5	5
$h_f$	9.28	6.02	4.02
$(d_f^{in.})^{c.s.}$	4.96	4.90	4.29

In the present study, Coulomb friction coefficient, obtained from the ring test, is used to model the interface friction. In the ring test for the lubricant-free compressions (on the Mohr&Federhaff hydraulic press), three ring-shaped specimens having the same dimensions are compressed down to different reductions. (Table 4.7) Designations for ring specimens are given in Figure 3.19.

It can be seen in Figure 4.12 that the hole diameter of the specimen gets smaller with increasing height reduction, showing that friction at the die-specimen interface is severe.

FEM simulations are done, using the same geometry with the experiments and selecting different values of Coulomb friction coefficients in the program.

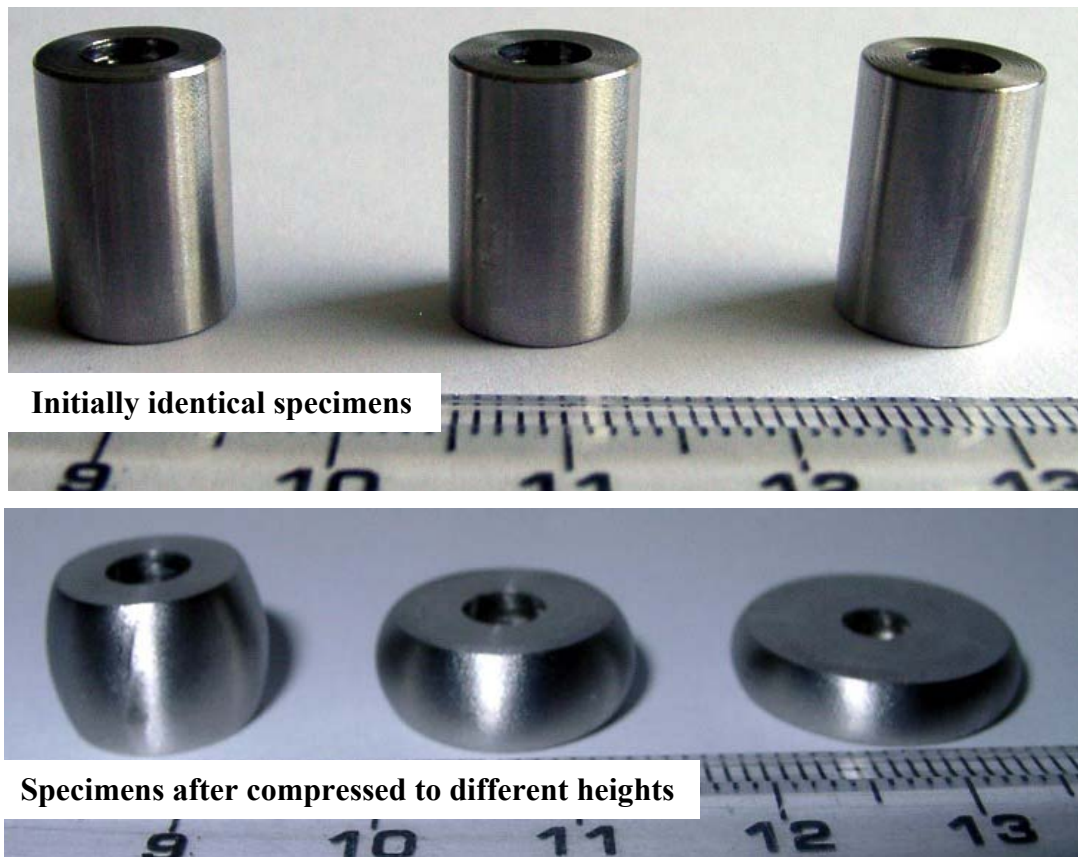


**Figure 4.12** Ring compression specimens used for friction factor estimation in lubricant-free compressions

FEM simulations with different Coulomb friction coefficients supply the calibration curves, showing the radial hole displacement with respect to the stroke of the punch (Figure 4.13). Three ring test specimens, given in Table 4.6, represent the three experimental points of Figure 4.13.

Hole diameters are measured by using toolmaker's microscope with 0.001 mm accuracy and specimen heights are measured by using calipers with 0.02 mm accuracy. Since the change in hole radius of the specimens is used in Figure 4.13, the error in measurements is decreased to half.

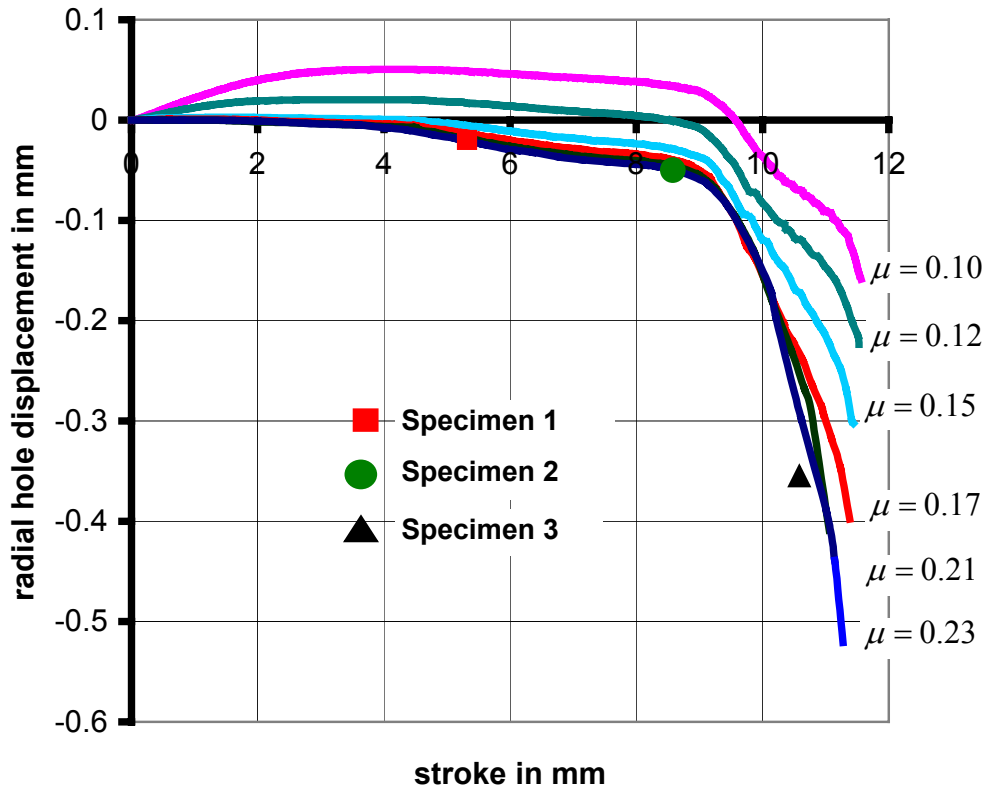


**Figure 4.13** Calibration curves for Table 4.6 specimens by using corrected flow curve

Although the measurements may be accepted as accurate enough, the variation of radial hole displacement is very close to each other after the Coulomb friction factor of 0.17. The friction coefficient is accepted to be  $\mu = 0.21$ .

For the case represented in Figure 4.13, radial hole displacement is always (throughout the applied stroke of the punch) negative for the Coulomb friction coefficients greater than  $\mu = 0.15$ . This means that the hole diameter is always getting smaller with the applied compression stroke and accelerates with increasing stroke (increasing contact pressure).

The same procedure is applied in order to find the friction condition for the compressions made on the Zwick press, the contact surfaces of which are lubricated

with molybdenite paste ( $\text{MoS}_2$ ) during the experiments (Figure 4.14). Material flow curve characterization tests have also been handled on this press and the effect of friction factor, which will be obtained now for the experiments of this press, must be eliminated from the experimental compression flow curve.

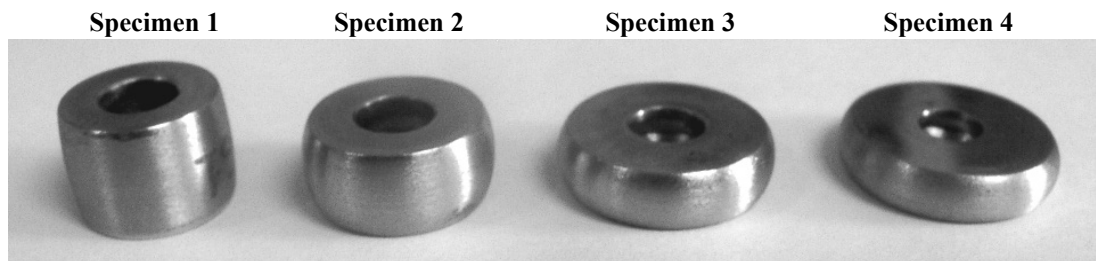


**Figure 4.14** Ring compression specimens used for friction factor estimation in lubricated compressions on the Zwick press

FEM simulations with different Coulomb friction coefficients supply the calibration curves, showing the radial hole displacement with respect to the stroke of the punch (Figure 4.15). Four ring test specimens of Figure 4.14 represent the four experimental points of Figure 4.15. They show similar characteristics with the calibration curve of  $\mu = 0.1$ .

For the case represented in Figure 4.15, radial hole displacement is positive for the Coulomb friction coefficient of  $\mu = 0.1$ . This means that the hole diameter is getting larger with the applied compression stroke. This enlargement is seen for specimens 1, 2 and 3 shown in Figures 4.14 and 4.15. The hole diameter of specimen 4 is smaller than the hole diameter of initial specimen shown in Figure 4.14, and by looking at the position of specimen 4, a friction coefficient greater than  $\mu = 0.1$  could have been found. But this situation cannot be generalized, as the increase in friction for the case of specimen 4 may be caused by the decrease of lubricant at corresponding height reduction and enlargement of die-specimen contact area.

Using this pre-guess value, FEM iteration method (correction factor method), which is explained in Section 2.4.2 and 3.2.2, was handled to obtain the friction-free compression curve (Koçaker, 2003).

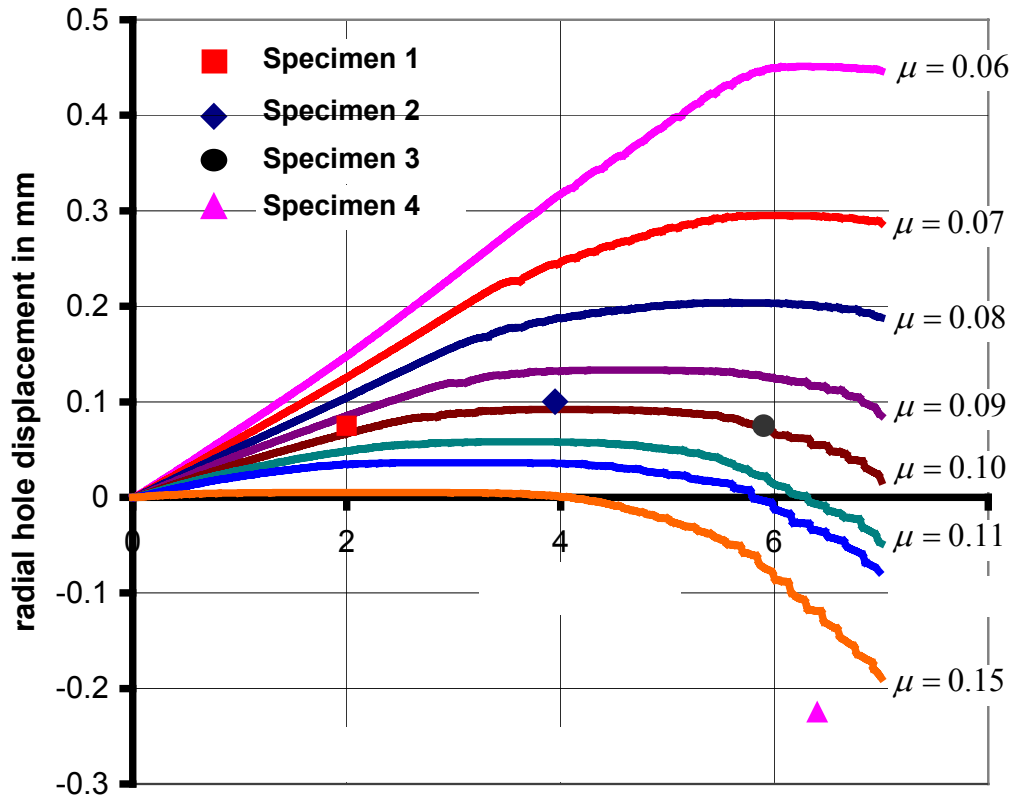


**Figure 4.15** Calibration curves by using experimental flow curve

Then using this friction-free (corrected) flow curve, the ring test simulations are repeated to obtain the new calibration curve for checking the pre-guessed value.

As the friction coefficient seems to be almost the same as the pre-guess value ( $\mu = 0.1$ ), this iteration method is accepted to be successful (Figure 4.16).

To sum up,  $\mu = 0.1$  will be used in the modeling of experiments made on Zwick press, and  $\mu = 0.21$  will be used in the modeling of experiments made on Mohr&Federhaff press.

In all compression models, the compression flow curve which was corrected by subtracting the effect of  $\mu = 0.1$  friction condition from the experimental compression flow curve is used.

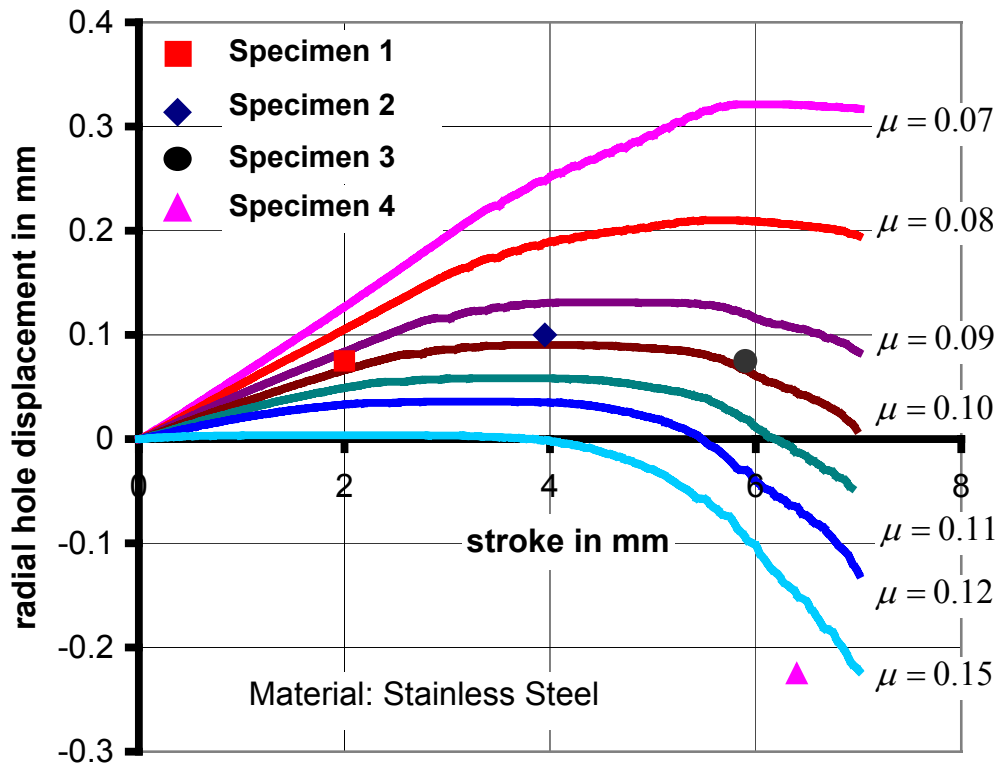


Figure 4.16 Calibration curves by using corrected flow curve

#### 4.4.2 Failure Experiments

In this section, FEM simulation results of failure experiments will be explained. Simulations are performed until the final dimensions of specimens in experiments are arrived. Several criteria, explained in Sections 2.3.1, 2.3.2, and 2.3.3 are used.

##### 4.4.2.1 Tension Test Modeling

The modeled part of the tension test specimens, which is the quarter of axial cross-section, is shown in Figure 3.22.

The simulation continues until the minimum neck diameter at the fracture zone, which was tabulated in Table 4.1, is reached. Crack initiation starts at the center of tension test specimens. This critical region, where the maximum damage values are sought, is also marked in Figure 3.23.

The point where the damage value becomes maximum should be included in the region cracked in the experiment. Such criteria are said to be successful for detecting the critical region. Tensile specimens are known to start breaking in the center. Each of the criteria calculates maximum damage at the center portion, where the crack initiates.

Damage calculations are done for all criteria used and the central critical damage values are noted in Table 4.8.

When the ‘maximum effective stress / ultimate tensile strength model’ was selected, the ultimate tensile strength has been defined as a constant, taken from the tensile engineering stress-strain data ( $\sigma_u = 560 \text{ MPa}$ ).

**Table 4.8** Various criteria and their critical values, which become maximum at the center of fracture diameter

Criteria	Damage	Criteria	Damage
Freudenthal (MPa)	1340	Rice-Tracey	1.56
Cockroft-Latham (MPa)	1560	McClintock	3.28
Normalized Cockroft-Latham	1.56	Max. effective stress/ UTS	3.34
Brozzo	1.54	Ayada	208

#### 4.4.2.2 Compression Test Modeling

Due to the symmetry axis and symmetry plane of the compressed specimens, quarter parts of cross-sections are modeled in FEM analysis. The modeled parts of standard

compression, ring and flanged specimens are shown in Figure 3.25, and the modeled part of tapered specimen is shown in Figure 4.17.

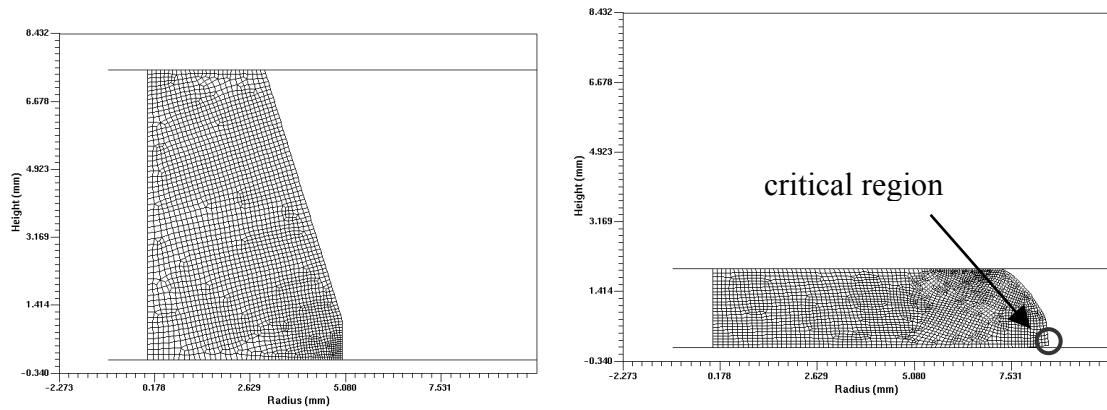


**Figure 4.17** Critical damage region for tapered specimen (Deform 2D Version 7.1)

Each specimen, whose dimensions are given in Tables 4.2, 4.3, 4.4 and 4.5, is modeled and the displacement of the punch is limited according to the change of height,  $(h_0 - h_f)$ , of that specimen.

The simulations are repeated for each damage criterion. The distribution of damage values, which are calculated according to the used criterion, can then be observed.

Since no cracks (except the fracture of the tension test specimens) are observed in experiments, the criteria are used to detect the locations of critical points and the possible upper bounds for safe damage values of each criterion. The specimen with similar loading conditions can be assumed to have no cracks below these safe damage values.

According to each criterion, critical region for a standard compression specimen, for which the maximum value of damage is detected in the simulations, is the same as the cracked critical region as shown in Figure 3.26.

The maximum damage values of various criteria of tested standard compression specimens given in Table 4.2 are tabulated in Table 4.9.

**Table 4.9** Various criteria and their critical values at critical regions of given standard compression specimens

Damage criteria	Using Mohr&Federhaff hydraulic press ( $\mu = 0.21$ )		
	Damage values		
	S.Comp.1 (no crack)	S.Comp.2 (no crack)	S.Comp.3 (no crack)
Freudenthal (MPa)	500	685	637
Cockroft-Latham (MPa)	323	433	385
C-L Normalized	0.37	0.44	0.40
Brozzo	0.42	0.49	0.44
Max. effective stress/ UTS	1.85	1.93	1.90
Ayada	0.07	0.10	0.08
Rice&Tracey	0.34	0.43	0.38
McClintock	0.52	0.70	0.61

According to each criterion, critical region for a flanged compression specimen, for which the maximum value of damage is detected in the simulations, is the same as the cracked critical region as shown in Figure 3.27.

The maximum damage values of various criteria of tested flanged compression specimens given in Table 4.3 are tabulated in Table 4.10.

In the selection of specimen dimensions of the various compression specimens, simulations are done for the different possible specimen dimensions. Limitations exist, like the annealed raw material initial diameter, maximum load capacity of the press, and maximum height to diameter ratio (aspect ratio) due to buckling of the specimen. The aspect ratio is kept below 2.3. The effect of two flanged specimen dimensions ( $h_0$  and  $d_0$ ) on damage values of Brozzo criterion and Cockroft & Latham criteria are shown in Figures 4.18 and 4.19 respectively.

**Table 4.10** Various criteria and their critical values at critical regions of given flanged specimens

Damage criteria	Damage values			
	Hydraulic press used:			
	Mohr&Federhaff ( $\mu = 0.21$ )	Zwick ( $\mu = 0.1$ )		
	Flanged 1	Flanged 2	Flanged 3	Flanged 4
Freudenthal (MPa)	455	101	97	99
Cockcroft-Latham (MPa)	484	112	108	110
C-L Normalized	0.66	0.232	0.226	0.229
Brozzo	0.67	0.235	0.228	0.230
Effective stress / UTS	1.82	1.15	1.14	1.15
Ayada	0.26	0.098	0.095	0.096
Rice&Tracey	0.73	0.256	0.249	0.252
McClintock	1.34	0.48	0.46	0.47

The diameter and thickness of the flanged region is taken as 10 mm and 2 mm, respectively as shown in Figures 4.18 and 4.19.

$\ln(h_0/h)$  represents the accumulated strain during compression process. It is clear that when  $d_0$  is equal to 8 mm, the slope is greater (the damage rate is greater). And when initial height,  $h_0$ , is 15 mm, the damage can increase to higher values. But this increase is also dependent on the loading capacity of the press. The required load increases as well, when the height reduction increases.

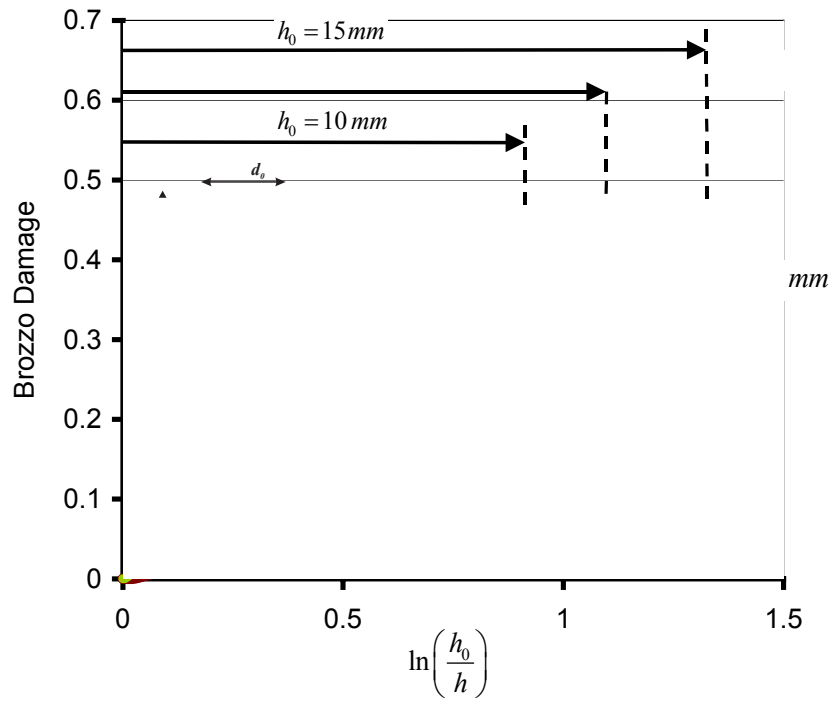


**Figure 4.18** The effect of flanged specimen dimensions on damage values of Brozzo criterion

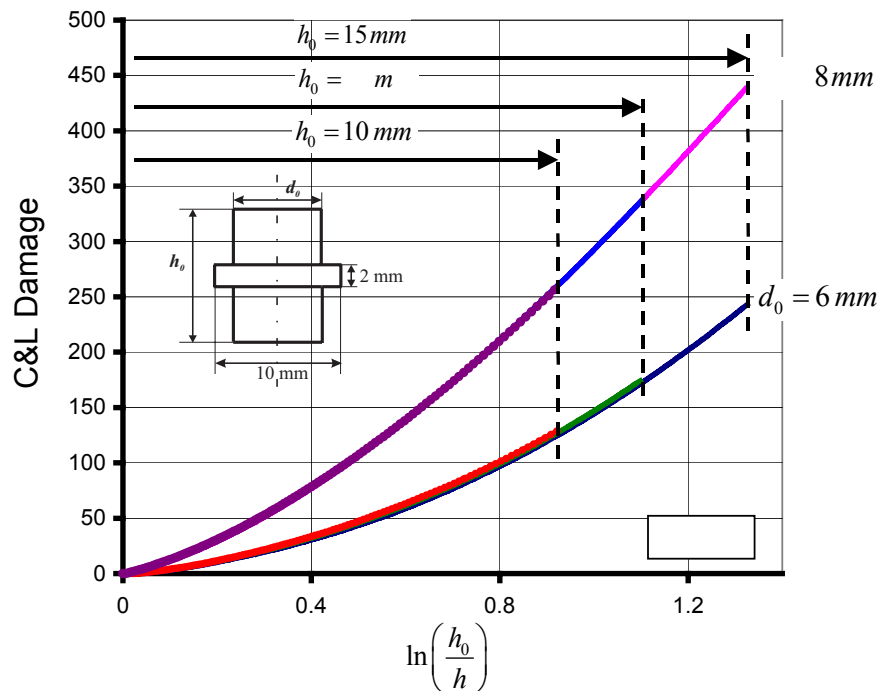


**Figure 4.19** The effect of flanged specimen dimensions on damage values of Cockcroft&Latham criterion

According to each criterion, critical region for a ring compression specimen, for which the maximum value of damage is detected in the simulations, is the same as the cracked critical region as shown in Figure 3.28.

The maximum damage values of various criteria of tested ring specimens given in Table 4.4 are tabulated in Table 4.11.

**Table 4.11** Various criteria and their critical values at critical regions of given ring specimens

Damage criteria	Damage values				
	Hydraulic press used:				
	Mohr&Federhaff ( $\mu = 0.21$ )			Zwick ( $\mu = 0.1$ )	
	Ring 1	Ring 2	Ring 3	Ring 4	Ring 5
Freudenthal (MPa)	410	418	451	346	408
Cockroft-Latham (MPa)	381	390	426	205	265
C-L Normalized	0.47	0.48	0.52	0.26	0.32
Brozzo	0.50	0.51	0.55	0.29	0.35
Effective stress/ UTS	1.79	1.80	1.82	1.72	1.78
Ayada	0.15	0.16	0.17	0.04	0.06
Rice&Tracey	0.50	0.51	0.54	0.23	0.31
McClintock	0.85	0.87	0.94	0.35	0.46

According to each criterion, critical region for a tapered compression specimen, for which the maximum value of damage is detected in the simulations, is the same as the cracked critical region as shown in Figure 4.17.

The maximum damage values of various criteria of tested tapered specimens given in Table 4.5 are tabulated in Table 4.12.

**Table 4.12** Various criteria and their critical values at critical regions of given tapered specimens

Hydraulic press used:	Mohr&Federhaff ( $\mu = 0.21$ )	Zwick ( $\mu = 0.1$ )	
Specimens:	Tapered 1	Tapered 2	Tapered 3
Freudenthal (MPa)	148	84	83
Cockroft-Latham (MPa)	131	40	39
C-L Normalized	0.152	0.082	0.080
Brozzo	0.155	0.1	0.097
Effective stress/ UTS	1.80	1.08	1.07
Ayada	0.05	0.0027	0.0023
Rice&Tracey	0.17	0.050	0.047
McClintock	0.87	0.063	0.059

In order to see the effect of geometrical modifications of specimens on damage accumulation, a parametric study has been done by using FEM simulations of stainless steel tapered specimen compressions. Designations for dimensions of tapered specimen are given in Figure A.1 of the Appendix-A. The FEM results can be seen in Tables A.1, A.2, and A.3. In these tables, Cockcroft & Latham, Brozzo and Freudenthal damage values for various specimens are tabulated respectively. Compressions are simulated to the final height,  $L_{final}$  of 2mm in each model. The effects of introducing a hole to the specimen and changing the Coulomb friction factor is also examined. Lower punch forces are obtained with increasing hole radius and decreasing friction. But the damage values are decreased by introducing the holes to the specimens. With increasing friction factor, the damage values also increases. However the damage values are not high enough to reach the damage value at the fracture of tension specimens.

The criterion of Oyane, which was explained in Section 2.3.2, cannot be applied in this chapter (for stainless steel), as this criterion requires the calculation of constant  $A$  of Eq. (2.23) experimentally from cracked specimens that have different initial geometries. And there is no cracked specimen for stainless steel.

In order to create greater damage values in the material, multiple processes may be applied to the material. The drawn stainless steel specimens with the diameter of 10.5 mm are used as a raw material. Tension test specimen is manufactured from drawn rod and tensioned up to the neck diameter,  $d_{neck}$  of 8.0 mm. (Figure 4.20)

Figure 4.21 shows the modeled Brozzo criterion damage values of tested flanged specimen during the compression process in the final. Drawing process, tension test and compression of the flanged specimen is modeled in sequence, and the damage history from the previous process is transferred into the new process. Therefore the damage curve does not start from the origin, it starts from the accumulated damage.

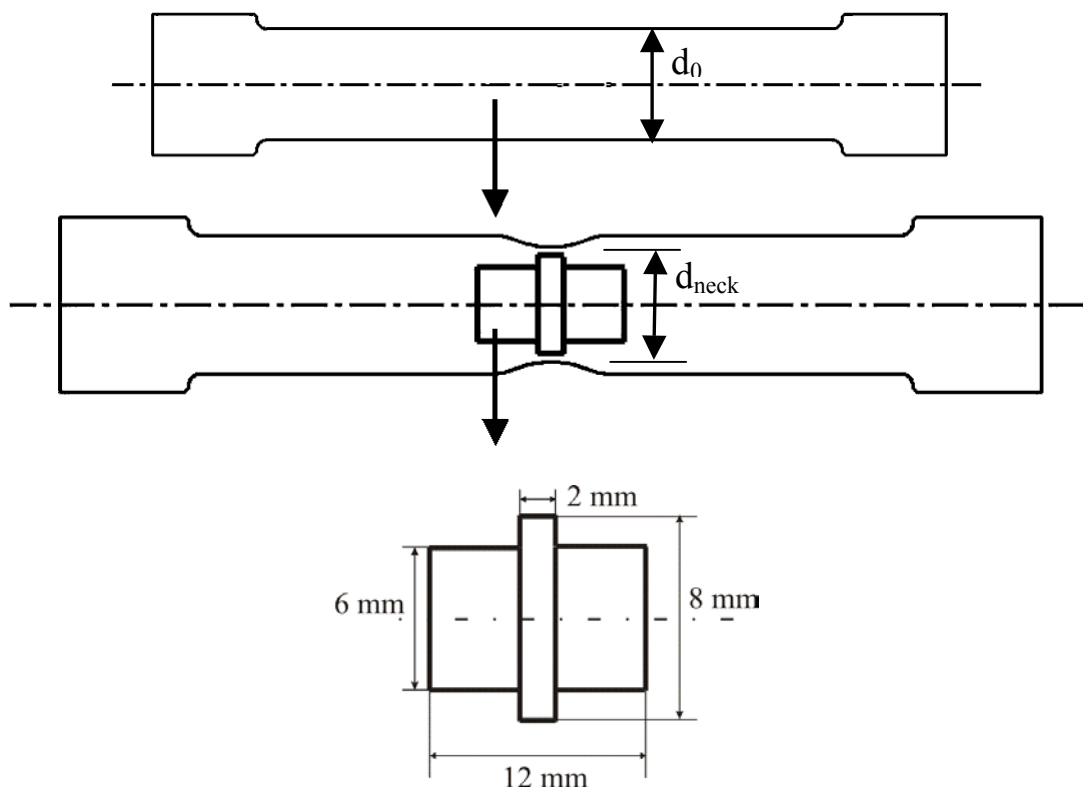


**Figure 4.20** Preparation of a flanged specimen from the necked region of a drawn tensile test specimen

Figure 4.21 also shows the damage curve if the manufactured specimen from the neck region were the ring specimen whose geometry is shown in the same figure.

The specimens are selected small in order to make the manufacturing feasible from the necked region. The final damage values for flanged specimen is greater than the ring specimen but it is still smaller than the value of damage, obtained in the tension test fracture. (Figure 4.21)

The dimensions of the flanged specimen produced for experiment is shown in Figure 4.20. The experiment is concluded with non-cracked specimen, final height of which is 2.7 mm. This multi-process experiment was unsuccessful in terms of showing any cracks.

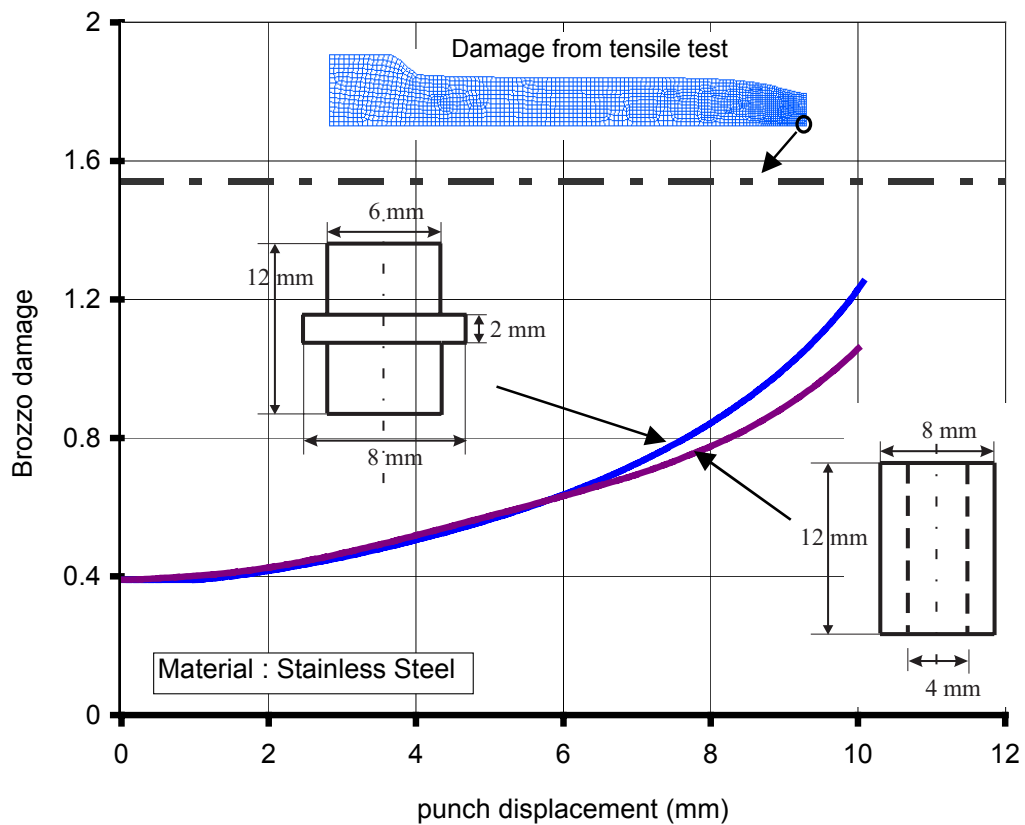


**Figure 4.21** Brozzo damage for the compression of flanged and ring specimens from necked region

#### 4.4.3 An Industrial Case Study

For an industrial case study, a process from HILTI Corporation is used. A surface crack has been observed in the stainless steel material as shown in Figure 4.22.

After supplying the finite element model for the mentioned process from HILTI, FEM analysis using different failure criteria are conducted.

Simulations are performed until the final dimensions of cracked specimen in heading process is arrived. Several criteria, explained in Sections 2.3.1, 2.3.2, 2.3.3 are used.



**Figure 4.22** Cracked material in a heading process (HILTI Corp., Liechtenstein)

The press set-up and corresponding FEM model, which is described on Figure 4.23, has been designed to perform a heading process, which was forcing the material to flow through the flash region between the steps (e) and (f) of Figure 4.23.

Headed geometry of the cracked specimen (Figure 4.22) is reached at the step (e) of Figure 4.23 (before the formation of flash). Therefore, the damage values that are maximum at critical (cracked) region are calculated up to step (e) and given in Table 4.13.

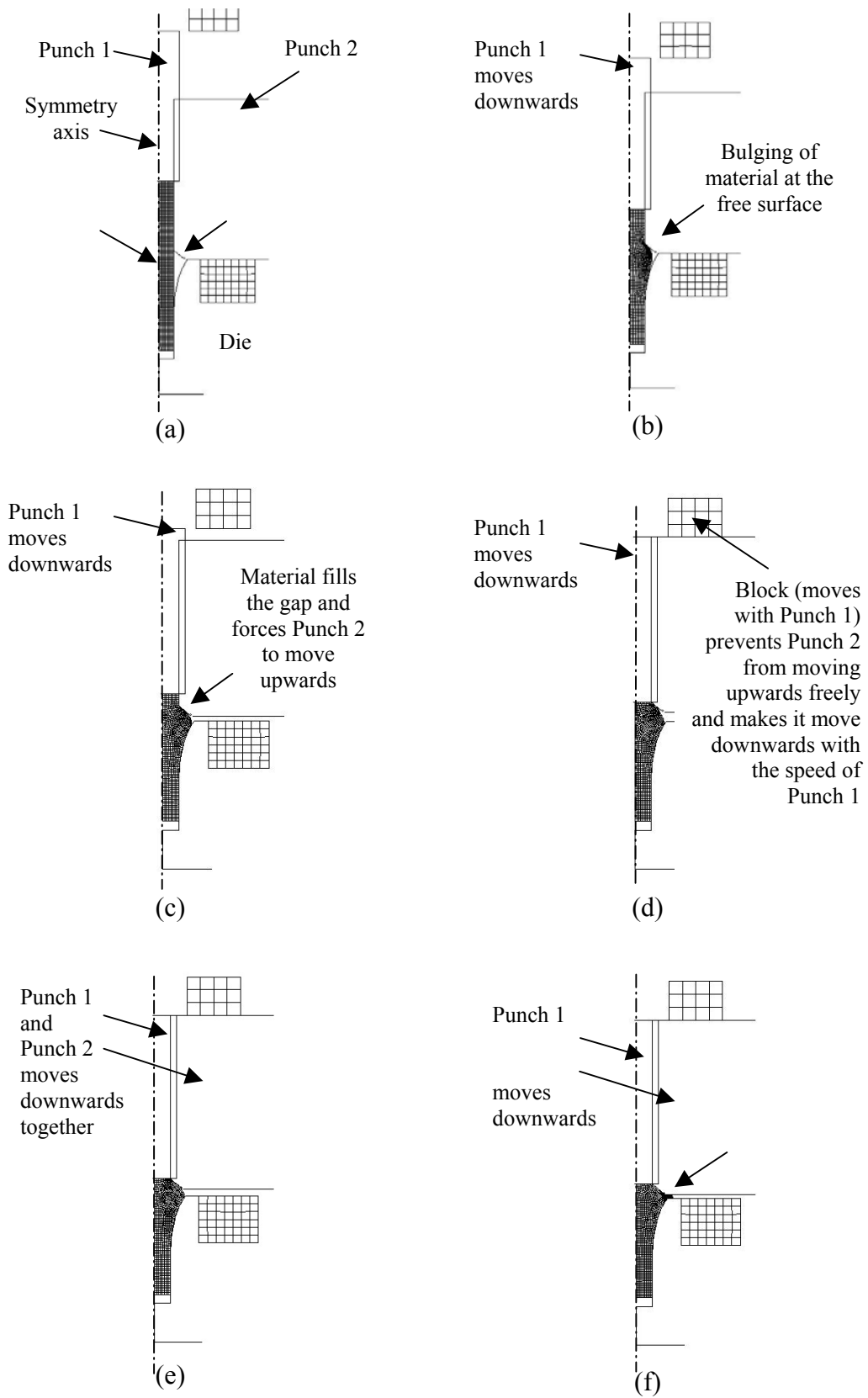


**Figure 4.23** Modeling of heading process (Deform 2D Version 7.1)

**Table 4.13** Various criteria and their critical values at crack regions

<b>Damage Criteria</b>	<b>Cracked Specimen in Heading Process</b>
Freudenthal (MPa)	1100
Cockroft-Latham (MPa)	405
Cockroft-Latham Normalized	0.376
Brozzo	0.422
Max. effective stress/ UTS	2.21
Ayada	0.039
Rice&Tracey	0.406
McClintock	0.403

Although the damage values of this cracked specimen at the critical region are also below the damage values of tension test (Table 4.7), they can be used as reference critical damage values where the primary stress is compressive.

#### **4.5 Discussions and Conclusions**

All of the criteria used in damage calculations detect the critical central point of tension test specimens correctly.

Since no cracks have been detected during the compression tests, it is difficult to comment on the success of a specific criterion in detecting correct critical points. The damage criteria may still be used to detect the locations of critical points and the possible upper bounds for safe damage values of each criterion. The specimen with similar loading conditions with the experiments can be assumed to have no cracks below these safe damage values.

The critical damage values for tension specimens (Table 4.7) are above those of compression specimens (Tables 4.8, 4.9, 4.10) for all criteria.

For an industrial case study, a process from HILTI Corporation is used. FEM model using different failure criteria for the mentioned process are conducted and damage values are shown in Table 4.12. The damage values of this cracked specimen at the critical region are also below the damage values of tension test (Table 4.7). This shows that, for stainless steel, it is not true to take the tension test fracture damage values as references for making comparisons with the damage values of compression specimens.

The Oyane criterion could not have been used for stainless steel, since the cracked compression specimens are required to calculate the material constant of this criterion.

## CHAPTER 5

### FORMABILITY ANALYSIS OF BRASS

#### 5.1 Introduction

In this chapter, the formability limits of brass (CuZn39) will be examined. First, the material flow curve is obtained. Then the results on failure experiments are given in detail. The modeling of these experiments are explained and the conclusions on the success of various failure criteria are presented.

#### 5.2 Obtaining Material Flow Curves

Tension and standard compression tests have been conducted in order to obtain the flow curve of brass. These flow curves have been used in FEM simulations of the performed failure tests. The procedure and calculation methods for tension and compression tests are explained in Section 2.4.

##### 5.2.1 Tension Flow Curve

Tension test specimens (Figure 5.1) of 10 mm gage diameter ( $d_0$ ) and 50 mm gauge length ( $l_0$ ) were tested using a Mohr&Federhaff hydraulic testing machine. This machine has an approximate punch velocity of 0.08 mm/sec and 40 tons of loading capacity. Experimental output has been taken as a load-displacement curve, drawn

by the testing machine on a graphic paper. This curve is calibrated to represent load (in N) and stroke (in mm) curve as explained in detail in Section 3.2.1.

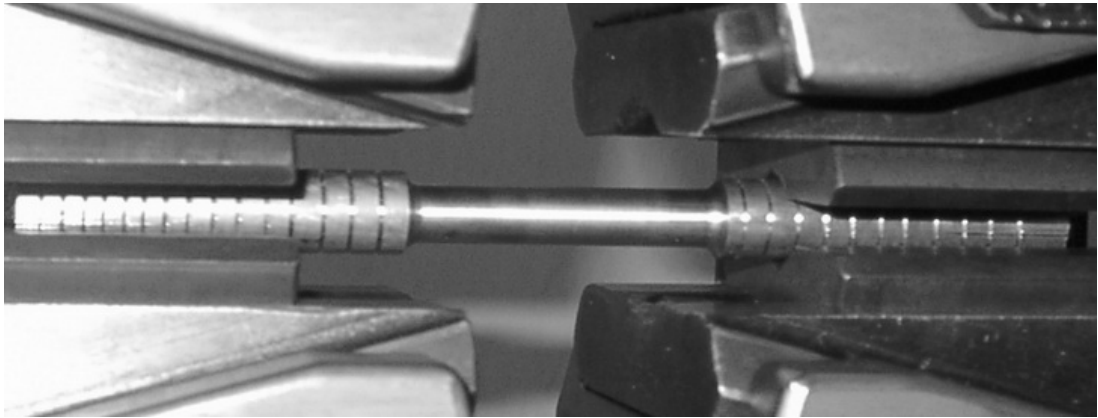


**Figure 5. 1** Tension test specimen, gripped by the press

Load displacement data can easily be converted to engineering stress – engineering strain data with the help of Eqs. (2.27), (2.28) and to true stress – true strain data with the help of Eqs. (2.32), (2.36).

The varying slope of engineering stress– engineering strain curve (at the region between the origin and yield point) does not represent the value of modulus of elasticity ( $E$ ), as the gripping (fastening) of the specimen at both ends is not perfect at the beginning of test and displacements include the sliding of the specimen without any elongation of the specimen.

Maximum point on engineering stress – strain curve gives the point where the necking starts and the ultimate tensile strength,  $\sigma_u$  as shown in Figure 5.2. For the brass specimen, ultimate tensile strength can be taken as  $\sigma_u = 481MPa$ , and necking strain as  $\varepsilon_{eng}^{necking} = 0.175$ .

Material response is not clear at the yielding region; but still the drop in the slope at possible yielding point is visible. It is shown to be  $\sigma_0 = 324MPa$  on Figure 5.2.

From Figure 5.2 it can be seen that tension data is only available up to true strain  $\epsilon_{true}$  of 0.16. After this point, necking and therefore non-uniform elongation starts.

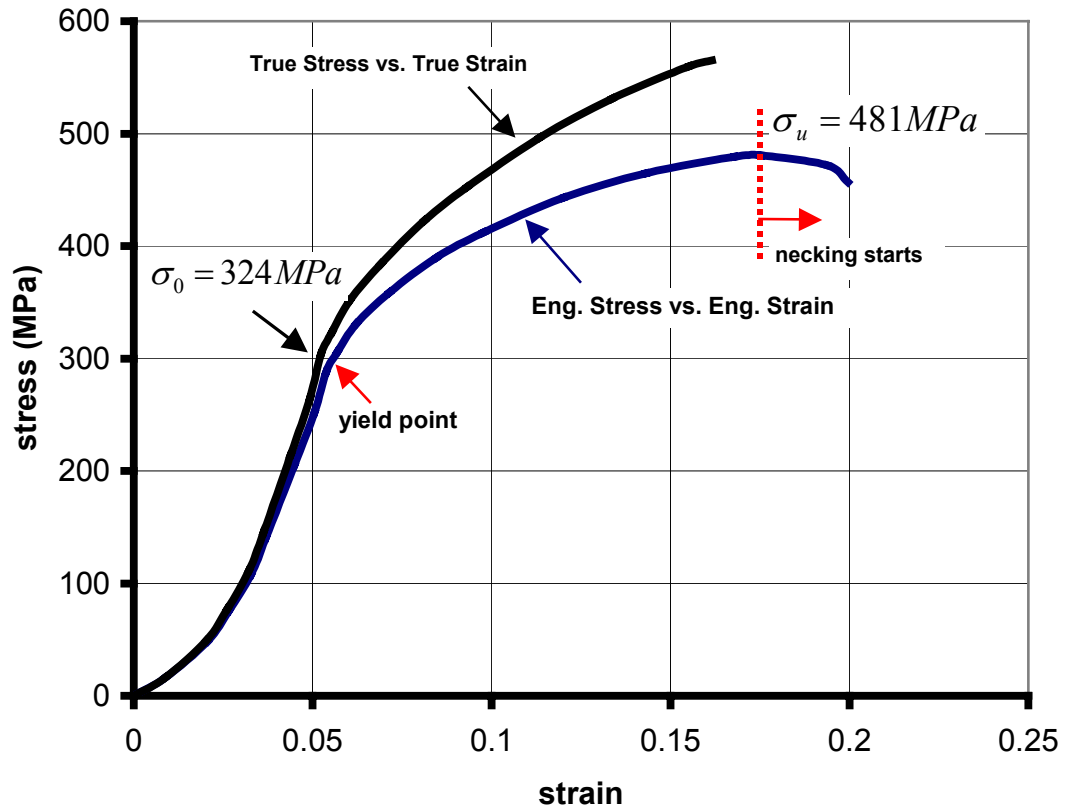


**Figure 5.2** Stress and strain curve of brass obtained from tension test

The flow curve can be obtained by plotting true stress values against corresponding equivalent true plastic strain values,  $\epsilon_{pl}$ , determined by Eq. (3.1). The flow stress for higher strain values can be obtained from the extrapolation of the experimental flow curves by using Ludwik's law, given in Eq. (2.39) and Eqs. (3.2), (3.3).

Equation of the trend line given in Figure 5.3 is used for calculating  $n$  and  $K$  values. *Log-log* curve for brass does not show a linear behavior. Two trendlines with their equations, one of which is fit to whole experimental flow curve and the other is fit to the end portion of flow data, are also shown in Figure 5.3.

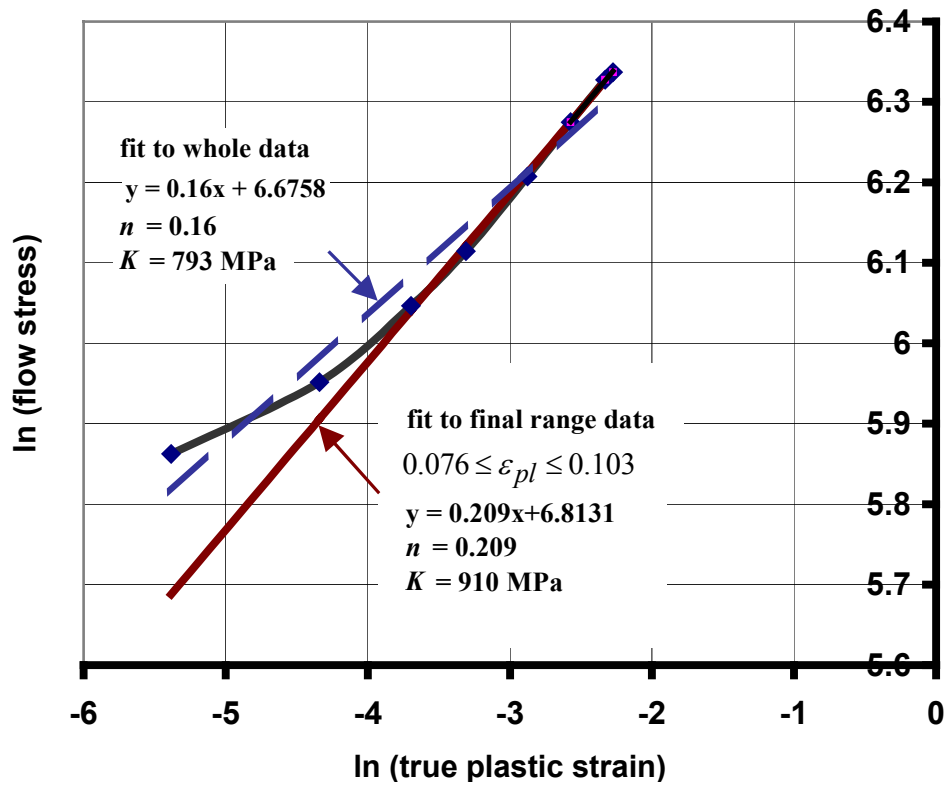


**Figure 5.3** Determination of  $n$  and  $K$  from *log-log* plot of tension flow data

Figure 5.4 shows the flow curve of brass obtained from tension test without any extrapolation, and the two Ludwik curves with different  $n$  and  $K$  values of Figure 5.3.

The flow curve with  $n$  and  $K$  values from the whole flow curve fits better to the starting part, but poorly represent the end part of experimental flow curve. Therefore, it is not suitable for extrapolating the flow curve. (Figure 5.4)

The flow curve with  $n$  and  $K$  values from the final range of flow curve fits very fine to the final region of experimental flow curve, although poorly represents the starting part of experimental flow curve. It is suitable only for extrapolating the flow curve. Therefore, the method to extrapolate the flow curve is to take the experimental flow curve and extrapolate the rest with  $n$  and  $K$  values obtained from the final range of flow data.

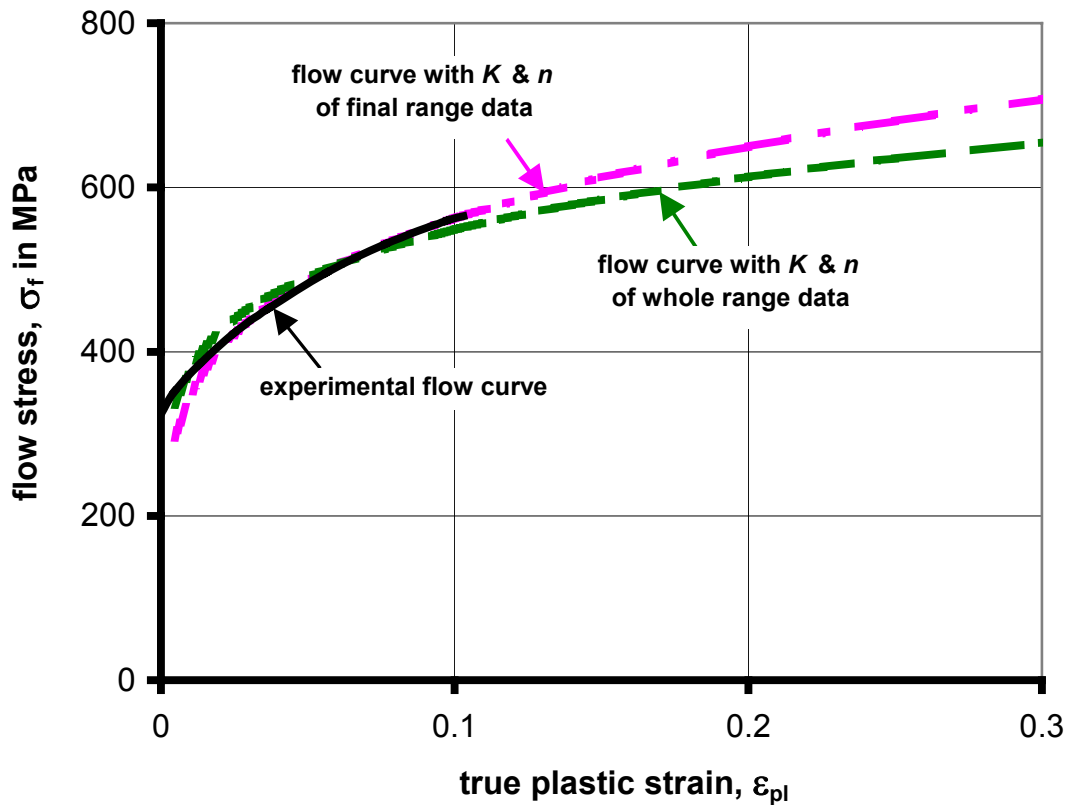


**Figure 5.4** Extrapolation for tension flow curve

### 5.2.2 Compression Flow Curve

Cylindrical specimens of 13 mm diameter and 13 mm height were compressed by using 40 tons Mohr&Federhaff hydraulic testing machine, having an approximate punch velocity of 0.05 mm/sec. Load-displacement curve of such a test is obtained by the same procedure mentioned in Section 3.2.1.

Load-displacement data can be converted to engineering stress – engineering strain data and to true stress – true strain data with the help of Eqs. (2.40), (2.42). These curves are represented in Figure 3.7.

The yield stress is shown to be  $\sigma_0 = 343 \text{ MPa}$  on Figure 5.5.

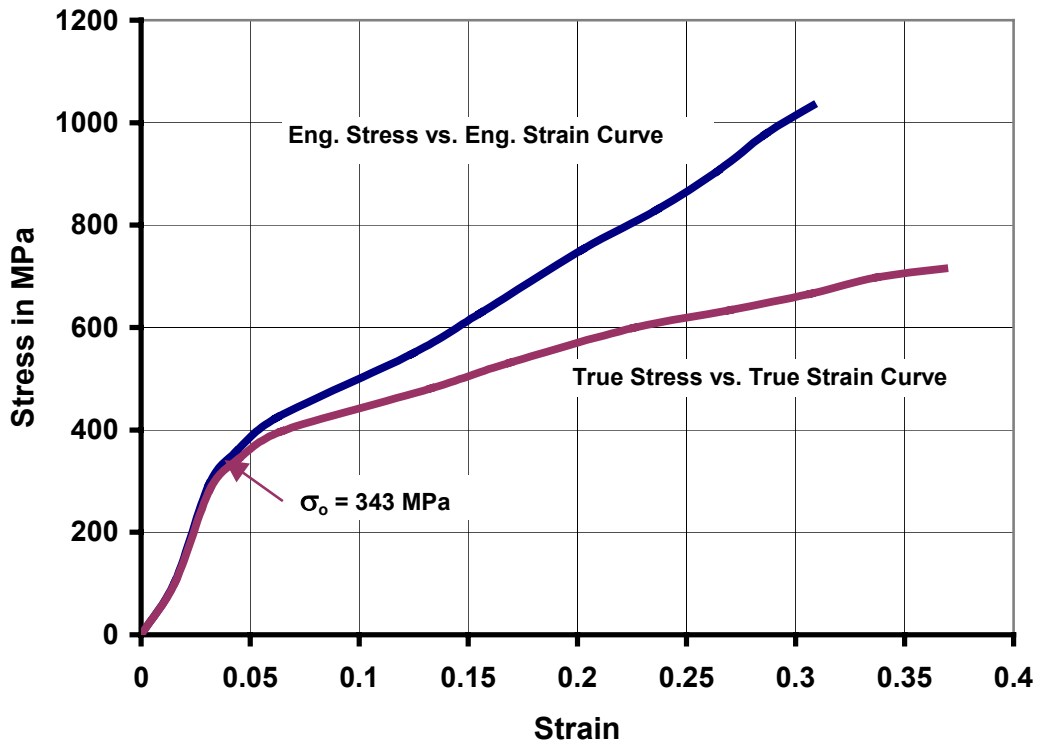


**Figure 5.5** Stress and strain curve of brass from standard compression test

From Figure 5.5 it can be seen that compression data is available up to  $\epsilon_{true} = 0.37$  due to the dimensions of the manufactured specimens and the loading capacity of the hydraulic press. Flow curve can be fitted to a polynomial equation, in order to represent a smooth flow curve, instead of the wavy appearance of experimental curve (Figure 5.6).

Experimental compression flow curve includes the effect of friction and this effect can be subtracted by using iterative FEM method, for which detailed explanation is given in Section 2.4.2. Correction function of iterative FEM method is used to correct experimental flow curve up to maximum compression strain (about 0.37).

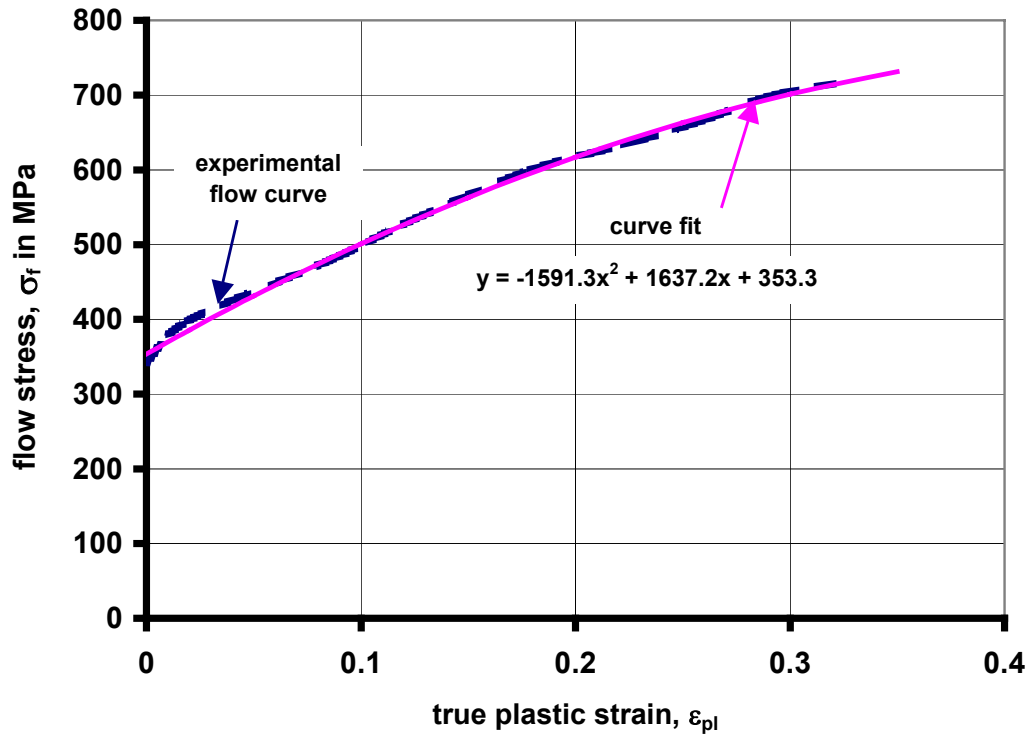


**Figure 5.6** Experimental flow curve of brass from standard compression test and smooth polynomial curve fit to it

For this method, the knowledge on the value of friction coefficient is required. Coulomb friction coefficient is accepted as  $\mu = 0.1$  from Section 5.4.1, in which ring experiments and FEM simulations are used to determine the friction coefficient.

The correction factors for two iterations and corresponding corrected flow curves are shown in Figure 5.7 with the curve fit to experimental flow curve. It can be seen that even one iteration may be enough to have the corrected flow curve, as the two iterations result in very similar flow curves.

The flow stresses for the higher strain values can be obtained from the extrapolation of the corrected flow curve again by using Ludwik's equation, Eq. 2.39.

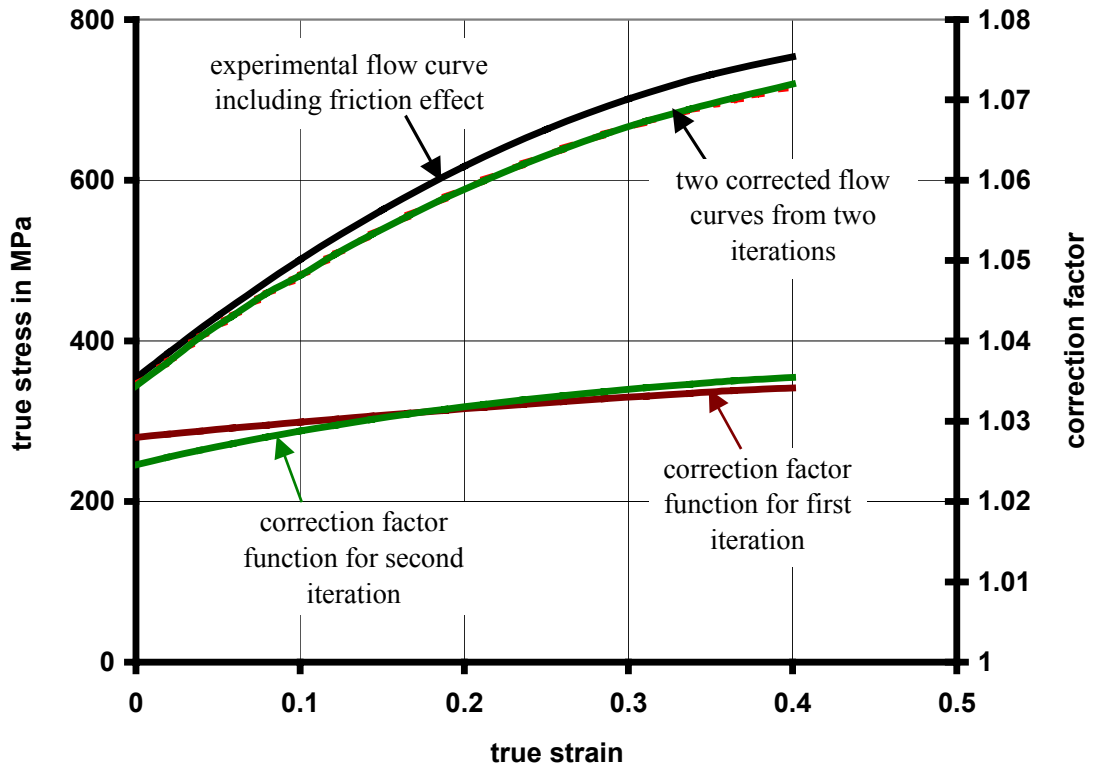


**Figure 5.7** Application of iterative FEM (correction factor) method for first and second iterations

By fitting this equation both in the whole range of flow data and in the final region ( $0.28 \leq \varepsilon_{pl} \leq 0.36$ ) of corrected flow curve,  $K$  and  $n$  values can be found as shown in Figure 5.8.

These two trendlines are very similar due to the shape of the *log-log* curve.  $K$  and  $n$  values from final region can be used to extrapolate the flow curve. The experimental flow curve can be taken directly and extrapolated with  $n$  and  $K$  values of final range for higher strain values.

Corrected and extrapolated flow curve is shown in Figure 5.9 and can be compared with the experimental flow curve. It is seen that there exists approximately 5 % drop in flow stress when the correction is completed.

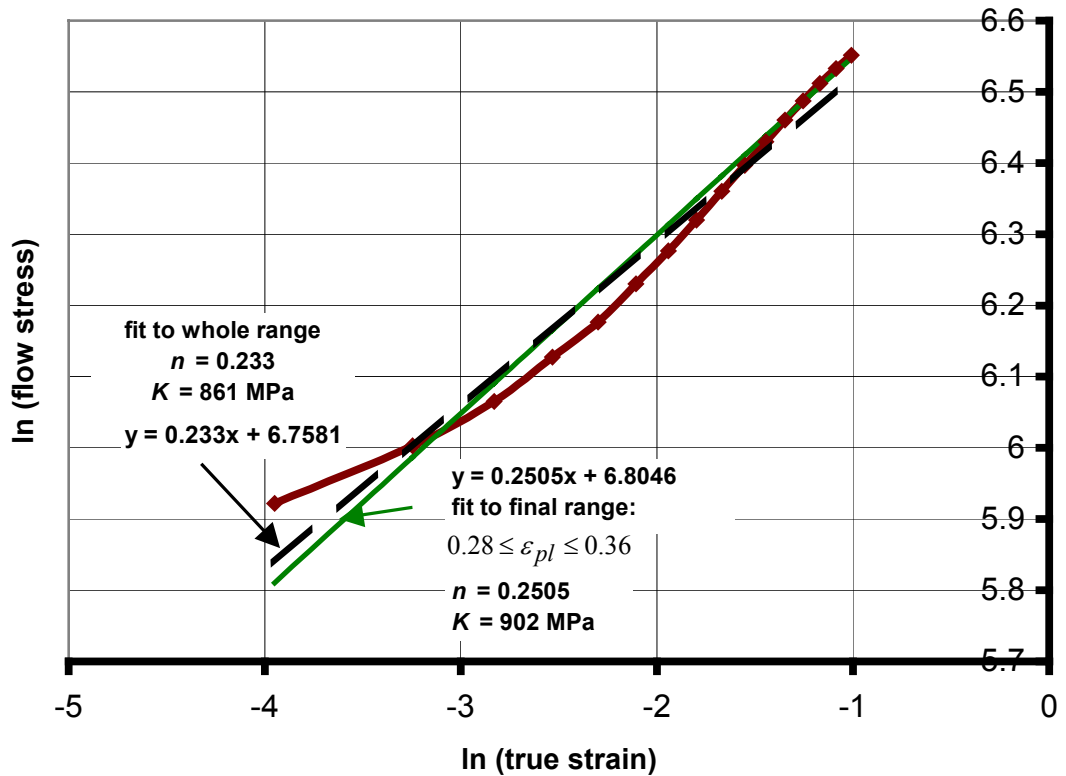


**Figure 5.8** Determination of  $n$  and  $K$  from the log-log plot of compressive flow curve

In order to make a comparison, flow curve from tension test is also shown in Figure 5.9.

The reason of the difference in tensile and compressive flow curves may be the variation of material response to the loading in opposite directions.

The tensile flow curve is used in tension test modeling, and the compressive flow curve is used in the modeling of various compression tests.

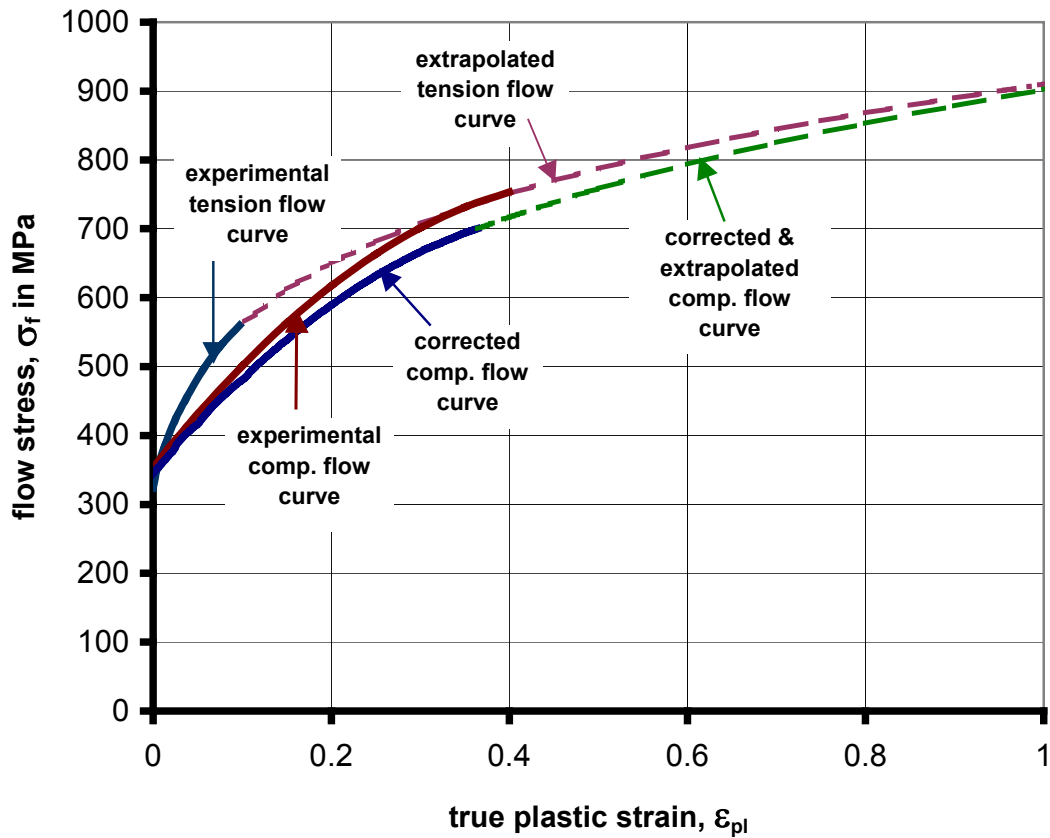


**Figure 5.9** Extrapolated flow curves of brass obtained from tension and compression tests

### 5.3 Performed Failure Experiments

Different forming processes create different stress states on the workpiece. Loading style, workpiece and tooling dimensions, and other process parameters like the friction condition on the contact surfaces result differences on stress and strain path of the workpiece. The experiments must cover different load cases, ideally as much as possible. Tension and various compression tests are handled during the experimental study.

### 5.3.1 Tensile Test

Tension tests specimens of 10 mm diameter and 50 mm gauge length were tested, using the 40 tons Mohr&Federhaff hydraulic testing machine having an approximate punch velocity of 0.08 mm/sec.

These results from the tension test are used both in obtaining tensile flow curve and in obtaining the minimum diameter of the neck region  $(d_{neck})_{min}$  when the specimen is fractured into two parts.

Designations for dimensions of initial and final geometries of a tension test specimen can be seen in Figures 3.1 and 3.14, where  $l_0$  is the initial gage length,  $d_0$  is the initial gage diameter,  $(d_{neck})_{min}$  is the minimum neck diameter at the fracture zone,  $l_f$  is the final gage length.

Related dimensions of tension test specimens are given in Table 5.1. Because of the lack of raw material, tension test is repeated two times only.

**Table 5.1** Dimensions of tension test specimens in mm

	Specimen 1	Specimen 2
$d_0$	9.85	10.15
$l_0$	50.1	50.9
$l_f$	60.1	60.4
$\Delta l$	10.0	9.5
$(d_{neck})_{min}$	7.7	8.1

### 5.3.2 Various Compression Tests

Specimens having different geometries are used for compression tests in order to create different stress states. Lubrication is not used in order to increase the barreling of the compressed specimens, so that the tensile stresses increase on the equator of the specimens, which accelerates the formation of surface cracks.

Cylindrical, flanged and ring specimens are compressed by using 40 tons Mohr&Federhaff hydraulic testing machine, having an approximate punch velocity of 0.05 mm/sec.

Procedure for the compression of the specimens are explained in Section 3.3.2.

Initial dimensions of the specimens of each geometry (cylindrical, flanged and ring geometries) are selected to be different in order to have cracks after following various stress paths and after different height reductions.

Designations for various dimensions of initial and final geometries of a standard compression test specimen is given in Figure 3.16, where  $h_0$  is the initial height,  $d_0$  is the initial diameter,  $h_f$  is the final height for both cracked and non-cracked specimens and  $d_f^{c.s.}$  is the final diameter of the specimen at die-workpiece contact surface. Related dimensions of standard compression specimens are given in Table 5.2.

**Table 5.2** Dimensions of standard compression specimens in mm

Specimens	$h_0$	$d_0$	$h_f$	$d_f^{c.s.}$
Standard Comp. 1 (no crack)	13.15	13.35	9.08	15.50
Standard Comp. 2 (cracked)	19.50	13.62	13.94	15.42
Standard Comp. 3 (cracked)	14.38	9.98	9.36	11.88
Standard Comp. 4 (cracked)	9.98	12.82	5.66	15.50

**Table 5.2** Continued

Specimens	$h_0$	$d_0$	$h_f$	$d_f^{c.s.}$
Standard Comp. 5 (cracked)	15.00	7.82	9.72	9.28
Standard Comp. 6 (cracked)	17.58	11.80	12.16	13.60
Standard Comp. 7 (cracked)	12.12	8.96	12.76	10.68

Designations for various dimensions of initial and final geometries of a flanged test specimen is given in Figure 3.18, where  $h_0$  is the initial height,  $d_0$  is the initial diameter,  $d_0^{flange}$  is the initial flange diameter,  $t_0^{flange}$  is the initial flange thickness,  $h_f$  is the final height and  $d_f^{c.s.}$  is the final diameter of the specimen at die-workpiece contact surface. Related dimensions of flanged specimens are given in Table 5.3.

**Table 5.3** Dimensions of flanged specimens in mm

Specimens:	Flanged 1	Flanged 2	Flanged 3	Flanged 4	Flanged 5
$h_0$	17.96	17.16	14.94	15.04	16.00
$d_0$	9.97	9.96	10.00	10.00	8.90
$d_0^{flange}$	13.53	13.47	13.04	12.10	13.00
$t_0^{flange}$	4.05	4.01	3.06	5.08	3.94
$h_f$	14.60	14.92	11.52	10.65	10.80
$d_f^{c.s.}$	11.00	11.00	11.06	10.52	10.52

Designations for various dimensions of initial and final geometries of a ring compression specimen is given in Figure 3.19, where  $h_0$  is the initial height,  $d_0^{out}$  is the initial outside diameter,  $d_0^{in}$  is the initial hole diameter,  $h_f$  is the final height and  $(d_f^{out})^{c.s.}$  is the final outside diameter of the specimen at die-workpiece contact surface.

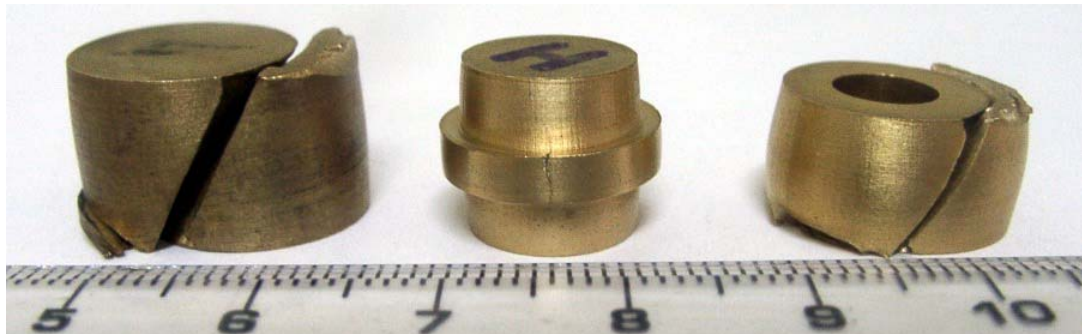
Related dimensions of ring specimens are given in Table 5.4. Initial dimensions of the specimens are selected to be different in order to have cracks initiated after following various stress paths and after different height reductions.

Dimensions are selected according to the loading capacity of the hydraulic press used. Specimen dimensions are decreased whenever more deformation is needed in order to observe a possible crack formation. (Figure 5.10)

**Table 5.4** Dimensions of ring specimens in mm

Specimen:	Ring 1	Ring 2	Ring 3
$h_0$	13.94	13.92	10.00
$d_0^{out.}$	13.00	13.00	13.00
$d_0^{in.}$	7.00	5.00	5.00
$h_f$	10.22	10.10	7.30
$(d_f^{out})^{c.s.}$	14.00	14.44	14.42

Crack initiation for standard compression and ring specimens was sudden and result with the breaking of the specimens into two parts as shown in Figure 5.10. The fracture plane makes an approximate angle of  $45^0$  to the symmetry axis of the specimens as in the case of shear type of cracks.



(a) standard compression

(b) flanged

(c) ring

**Figure 5.10** Free surface crack examples from experiments

#### **5.4 Modeling of Experiments**

Friction factor prediction, iterative correction of compression flow curve and calculation of damage values at the critical regions of failure experiments require the usage of finite element analysis. Modeling of the experiments by using finite element analysis is performed as a next step after the experiments.

Throughout the modeling of experiments, FEM simulation program Deform 2D version 7.1 has been used for Friction factor prediction, iterative correction of compression flow curve and calculation of damage values and another FEM program MSC Marc Mentat has been used to examine the maximum shear stresses on the path of the cracks.

Due to the geometry of specimens, axisymmetric analyses are performed in all simulations.

Parameters and details of FEM simulations are tabulated in Table 5.5.

**Table 5.5** Parameters used in FEM simulations

<b>Brass</b>	<b>Analysis Options</b>	FEM Program	Deform 2D version 7.1		
		Iteration Method	Newton Raphson		
		Workpiece Material Type	Elastic-Plastic		
		Die Material Type	Rigid		
		Convergence Ratio	Force Error Limit: 0.01		
			Velocity Error Limit: 0.001		
		Penalty Factor	1e+12		
		Symmetry	Axisymmetric		
		Number of Elements	Tension	2000-3500	
			Standard	1500-3500	
			Flanged	1500-3500	
			Ring	1000-2500	
		Remeshing	Automatic & Performed when the distortion on an element is severe and also forced at each 20-30 steps		
		Number of Steps	100 – 500		
	Time per step	0.01-0.03 s			
	Punch velocity	1 mm/s			
	<b>Contact Control</b>	Friction Model	Coulomb		
		Friction Coefficient	0.1 (Mohr&Federhaff press)		
		Relative Sliding Velocity	Default		
	<b>Material</b>	Tension Test Modeling	Tension flow curve		
		Standard Flanged Ring	}	Compression Modeling	Corrected (friction effect eliminated) compression flow curve
Modulus of Elasticity		105,000 MPa			
Poisson's Ratio		0.3			

### 5.4.1 Friction Factor Prediction

In the present study, the Coulomb friction coefficient, obtained from the ring test, is used to model the interface friction. In the ring test, ring-shaped specimens having the same dimensions are compressed down to different reductions (Table 5.6). Designations for ring specimens are given in Figure 3.19.

Then, FEM simulations are done, using the same geometry with the experiments and selecting different values of Coulomb friction coefficients in the program.

**Table 5.6** Dimensions of ring test specimens in mm

	Specimen 1	Specimen 2	Specimen 3
$h_0$	14.05	14.05	14.05
$d_0^{out.}$	13.00	13.00	13.00
$d_0^{in.}$	7.00	7.00	7.00
$h_f$	12.7	11.90	10.98
$(d_f^{in.})^{c.s.}$	7.03	7.04	7.04

The necessity and procedure for obtaining the friction coefficient are mentioned in Sections 2.5.3 and 3.4.1.

FEM simulations with different Coulomb friction coefficients supply the calibration curves, showing the radial hole displacement with respect to the stroke of the punch (Figure 5.11). Three ring test specimens, given in Table 5.6, represent the three experimental points of Figure 5.11. They show similar characteristics with the calibration curve of  $\mu = 0.1$ .

Using this pre-guess value, FEM iteration method (correction factor method), which is explained in Section 2.4.2 and 3.2.2, is handled to obtain the friction-free compression curve. Then using this friction-free (corrected) flow curve, the ring test simulations are repeated to obtain the new calibration curve.

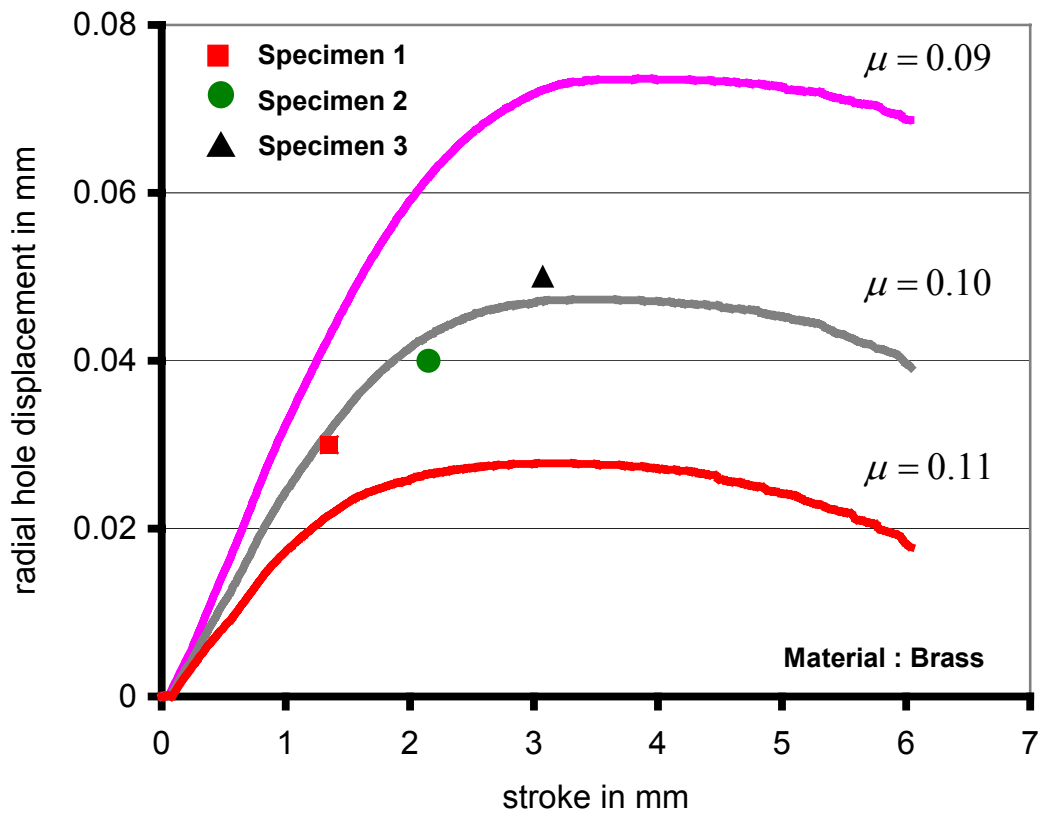


**Figure 5.11** Calibration curves by using experimental flow curve

As the friction coefficient seems to be almost the same as the pre-guess value, this iteration method is accepted to be successful (Figure 5.12).

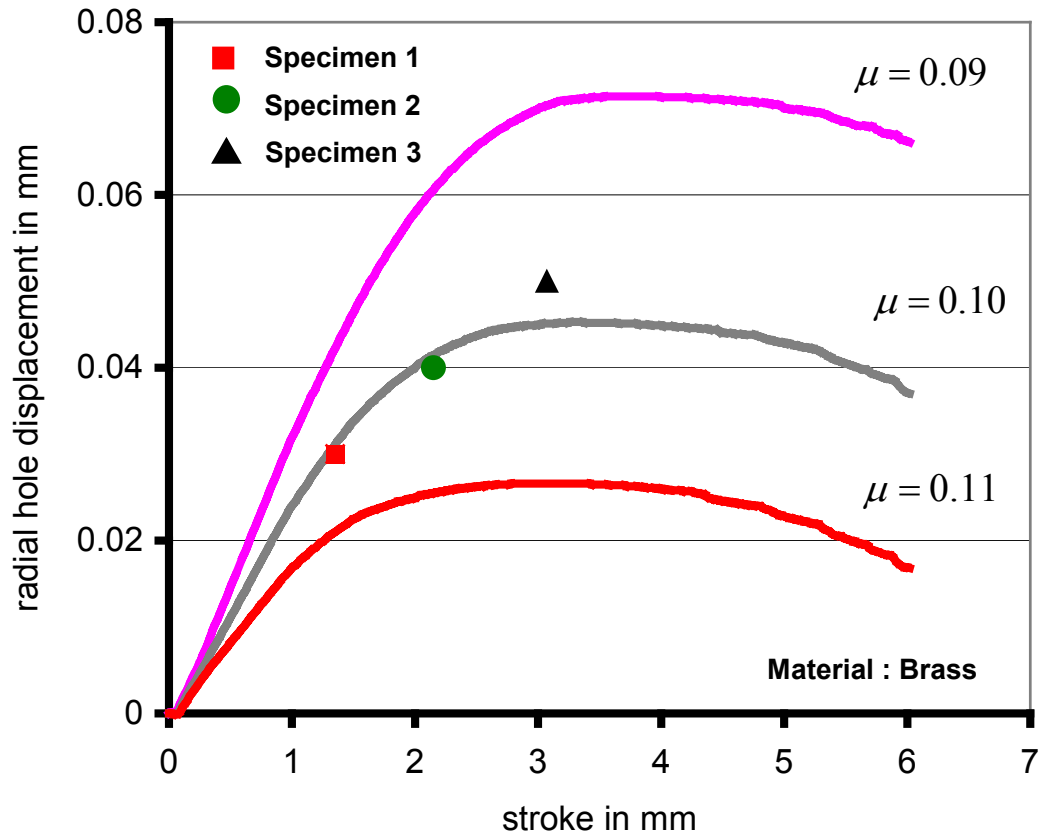


Figure 5.12 Calibration curves by using corrected flow curve

#### 5.4.2 Failure Experiments

In this section, FEM simulation results of failure experiments will be explained. Simulations are performed until the final dimensions of cracked or non-cracked specimens in experiments are arrived. Several criteria, explained in Sections 2.3.1, 2.3.2, 2.3.3 are used.

The correct prediction of the location and the first formation of a measurable crack are sought in the calculated results of the used criterion.

### 5.4.2.1 Tension Test Modeling

The modeled part of the tension test specimens, which is the quarter of axial cross-section, is shown in Figure 3.22.

The simulations, handled on Deform 2D, continues until the minimum neck diameter at the fracture zone, which was tabulated in Table 5.1, is reached. Crack initiation starts at the center of tension test specimens. This critical region, where the maximum damage values are sought, is also marked in Figure 3.23.

The point where the damage value becomes maximum should be included in the region cracked in the experiment. Such criteria are said to be successful for detecting the critical region. Tensile specimens are known to start breaking in the center. Each of the criteria criticizes the center portion, where the crack initiates.

Damage calculations are done for all criteria used and the central critical damage values are noted in Table 5.7.

When the ‘maximum effective stress / ultimate tensile strength model’ was selected, the ultimate tensile strength has been defined as a constant, taken from the tensile engineering stress-strain data as  $\sigma_u = 481$  MPa.

**Table 5.7** Various criteria and their critical damage values, which become maximum at the center of fracture diameter

Criteria	Damage	Criteria	Damage
Freudenthal (MPa)	327	Rice-Tracey	0.56
Cockcroft-Latham (MPa)	344	McClintock	1.1
Normalized Cockcroft-Latham	0.52	Max. effective stress/ UTS	1.88
Brozzo	0.52	Ayada	0.189

### 5.4.2.2 Compression Test Modeling

Due to the symmetry axis and symmetry plane of the compressed specimens, quarter parts of cross-sections are modeled in Deform 2D. The modeled parts of standard compression, ring and flanged specimens are shown in Figure 3.25.

Each specimen, whose dimensions are given in Table 5.2, Table 5.3 and Table 5.4, is modeled and the displacement of the punch is limited according to the change of height,  $(h_0 - h_f)$ , of that specimen.

Cracked critical region for a standard compression specimen, for which the maximum values of damage are obtained from the simulations, is shown in Figure 3.26.

The simulations are repeated for each damage criterion. The distribution of damage values, which are calculated according to the used criterion, can then be observed. The critical damage values of various criteria for standard compression specimens given in Table 5.2 are tabulated in Table 5.8.

**Table 5.8** Various criteria and their critical values at crack regions of given standard compression specimens

Damage criteria	Damage values		
	S.Comp.1 (no crack)	S.Comp.2 (cracked)	S.Comp.3 (cracked)
Freudenthal (MPa)	182	180	231
Cockcroft-Latham (MPa)	29	17.5	29.4
C-L Normalized	0.051	0.03	0.0468
Brozzo	0.075	0.0515	0.0765
Effective stress/ UTS	1.42	1.48	1.49
Ayada	0	0	0
Rice&Tracey	0	0	0
McClintock	0	0	0

**Table 5.8 (Continued)**

<b>Damage Criteria</b>	<b>S.Comp.4 (cracked)</b>	<b>S.Comp.5 (cracked)</b>	<b>S.Comp.6 (cracked)</b>	<b>S.Comp.7 (cracked)</b>
Freudenthal (MPa)	242	253	213	238
Cockcroft-Latham (MPa)	49.4	15.9	23.1	34.1
C-L Normalized	0.0805	0.0234	0.037	0.055
Brozzo	0.124	0.04	0.062	0.088
Effective stress/ UTS	1.55	1.52	1.47	1.51
Ayada	0	0	0	0
Rice&Tracey	0	0	0	0
McClintock	0	0	0	0

Ayada, Rice&Tracey and McClintock criteria calculate zero damage, since the mean stresses for the standard compression specimens stay negative at the critical point during the compression. Therefore, these criteria are not compared with other criteria for the brass material.

For the remaining five criteria, an average damage value of the cracked seven standard compression specimens is found and the percent deviation of the individual damage values of seven specimens from the average damage value of the criterion is shown in Figure 5.13.

The deviations may be acceptable only for the Freudenthal and Effective stress/UTS criteria. But for the other criteria, the deviations are too much, which means that the criteria does not calculate similar maximum values at the equatorial point of cracked specimen (Figure 3.26). It shows that these criteria are not capable of calculating maximum damage values at the true critical region of brass standard compression specimens. The criticized points by these criteria do not appear on the 45<sup>0</sup>-cracking path of the brass standard compression specimens.

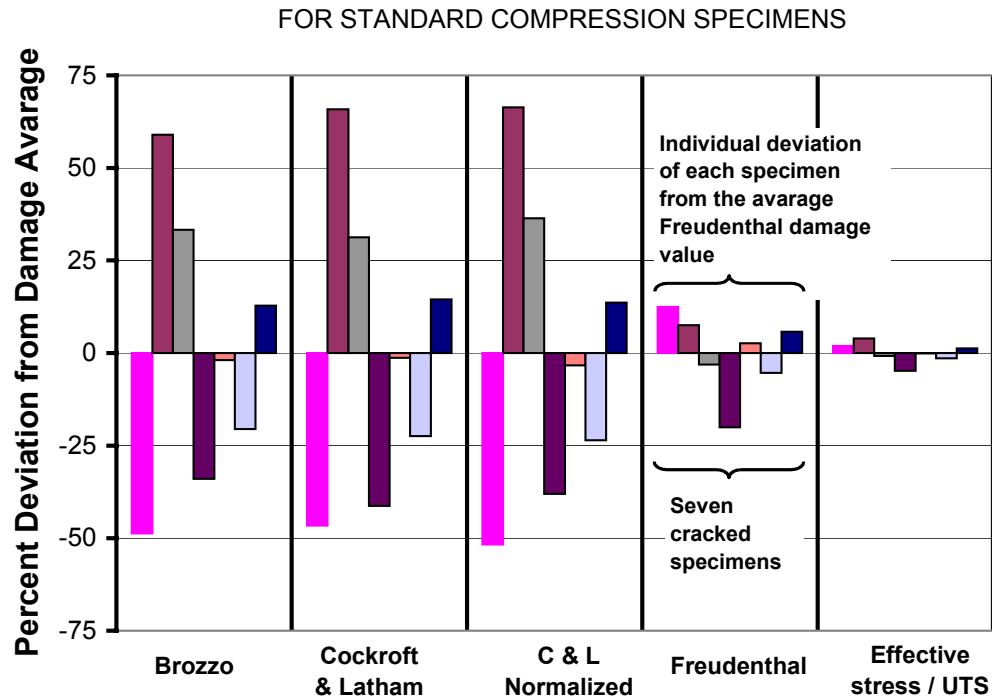


**Figure 5.13** Standard compression specimens deviations

Cracked critical region for a flange compression specimen, for which the maximum value of damage is sought from the simulations, are shown in Figure 3.27. This equatorial point is in the cracked critical region of flanged specimens of brass.

The critical damage values of various criteria for flanged specimens given in Table 5.3 are tabulated in Table 5.9.

An average damage value of the cracked five flanged compression specimens is found and the percent deviation of the individual damage values of five specimens from the average damage value of the criterion is shown in Figure 5.14.

The deviations of flange specimens from the average damage values are big again as in the case of standard compression specimens, and this is not expected as the criteria detect the true critical region (cracked region) for flanged specimens of brass.

**Table 5.9** Various criteria and their critical values at crack regions of given flanged specimens

Damage criteria	Damage values				
	Flanged 1 (cracked)	Flanged 2 (cracked)	Flanged 3 (cracked)	Flanged 4 (cracked)	Flanged 5 (cracked)
Freudenthal (MPa)	22.1	14.3	36.5	73.3	47.9
Cockcroft-Latham (MPa)	24.1	15.5	39.8	64	52.9
C-L Normalized	0.062	0.0413	0.097	0.139	0.124
Brozzo	0.061	0.0423	0.097	0.142	0.124
Effective stress / UTS	0.89	0.84	0.98	1.15	1.03
Ayada	0.025	0.016	0.04	0.034	0.053
Rice&Tracey	0.06	0.04	0.097	0.158	0.123
McClintock	0.12	0.08	0.19	0.24	0.24

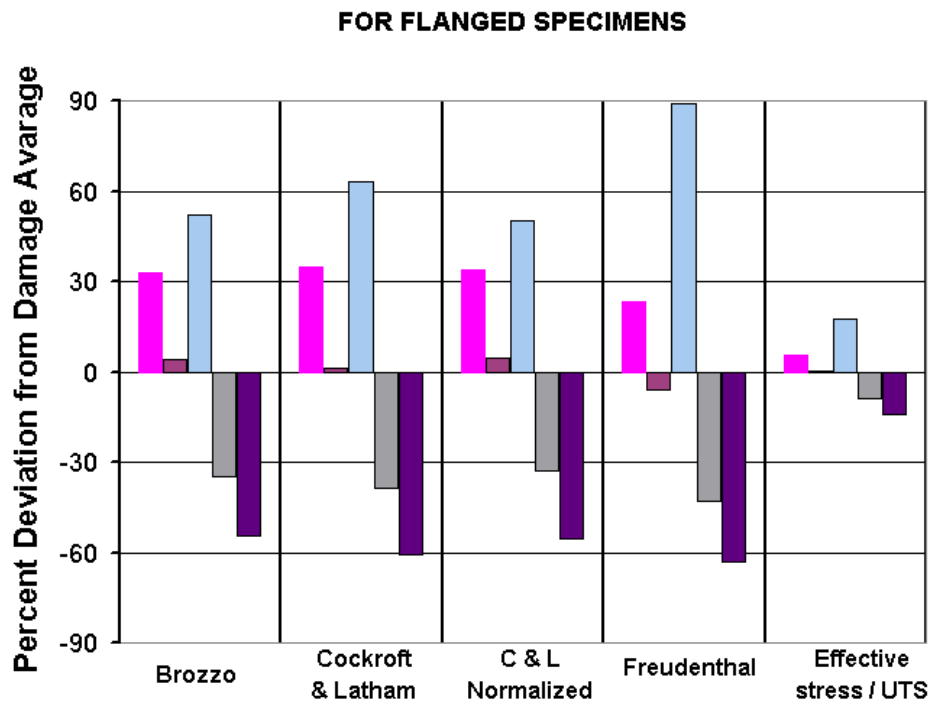


**Figure 5.14** Flanged specimens deviations

Cracked critical region for a ring compression specimen, for which the maximum value of damage is sought from the simulations, are shown in Figure 3.28.

The critical damage values of various criteria for standard compression specimens given in Table 5.4 are tabulated in Table 5.10.

**Table 5.10** Various criteria and their critical values at crack regions of given ring specimens

Damage Criteria	Damage Values		
	Ring 1 (cracked)	Ring 2 (cracked)	Ring 3 (cracked)
Freudenthal (MPa)	122	136	132
Cockcroft-Latham (MPa)	49.2	31.9	21.5
C-L Normalized	0.091	0.059	0.042
Brozzo	0.112	0.088	0.067
Max. effective stress/ UTS	1.31	1.34	1.33
Ayada	0.0034	0	0
Rice&Tracey	0.05	0	0
McClintock	0.06	0	0

The Freudenthal and maximum effective stress / UTS criteria can calculate similar critical damage values for the ring specimens of brass.

#### **The application of criterion by Oyane:**

The criterion of Oyane, which was explained in Section 2.3.2, is applied here separately, as it requires the calculation of constant  $A$  of Eq. (2.23) experimentally

Integral term  $\int_0^{\bar{\epsilon}_f} \frac{\sigma_m}{\bar{\sigma}} d\bar{\epsilon}$  of Eq. (2.24) is calculated and then plotted against  $\bar{\epsilon}_f$  for

various cracked specimens. This plot represents a linear relationship of  $y = mx + n$ .

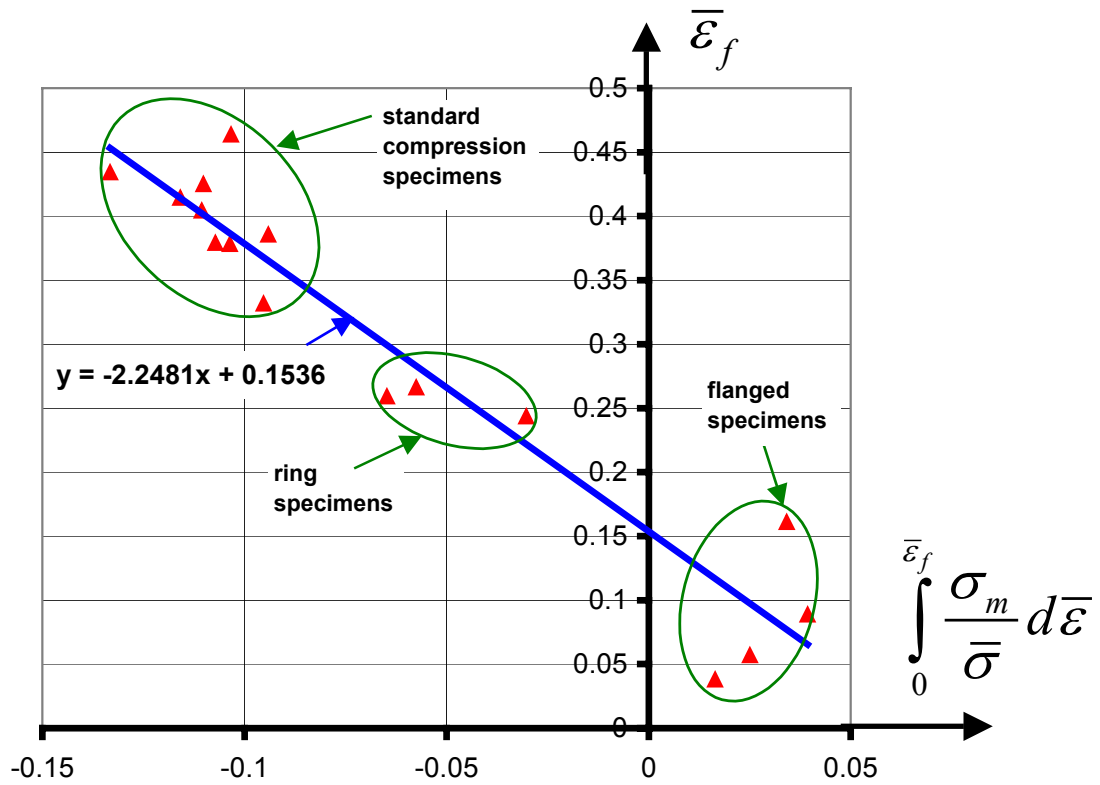


**Figure 5.15** Oyane criterion constant and critical value calculation

Therefore, material constant  $A$  can be obtained from the slope of the straight line,

$$A = -\frac{1}{m} = -\frac{1}{-2.2481} = 0.44$$

and material constant  $C$  from the intersection of the ordinate and this line,  $C = 0.153$ .

Two cracked standard compression specimens; one cracked flange specimen and one non-cracked standard compression specimen are added to the Figure 5.15. It is seen that cracked part stays over the trendline and the non-cracked specimen, for which lower effective strains than the critical effective strain is accumulated, stays below the trendline. (Figure 5.16)

On the other hand, the trendline is a linear fit to the cracked specimens; some of the cracked specimens are left just below the trendline and some of them are left over

the trendline. Therefore, it is critical to judge on a compressed specimen which is near to the trendline whether it will have cracks or not.

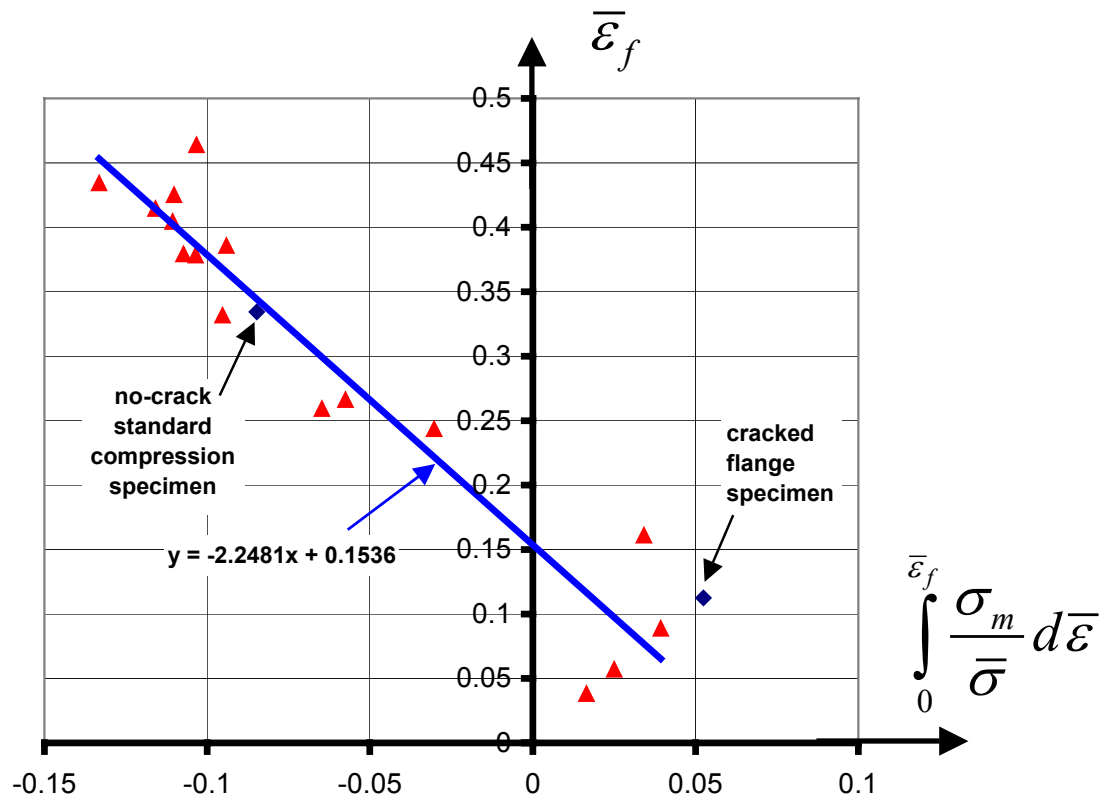


Figure 5.16 Application for Oyane damage criteria

### 5.4.3 Stress Paths for Critical Regions

Stress paths followed by the critical points of tension and compression specimens are shown in Figure 5.17. The path for each curve starts at the origin and end points of the curves represent the stress state of corresponding cracked specimen.

For the critical point (equatorial point) of compression specimens,  $\sigma_2$  is the axial stress and  $\sigma_1$  is the circumferential stress, which is tensile.  $\sigma_2$  is compressive at the beginning for standard compression and ring compression specimens. If the barreling were severe,  $\sigma_2$  might turn to be tensile as in the case of Figure 3.31. But the

cracking occurs at a relatively small compression for brass and barreling is not severe.

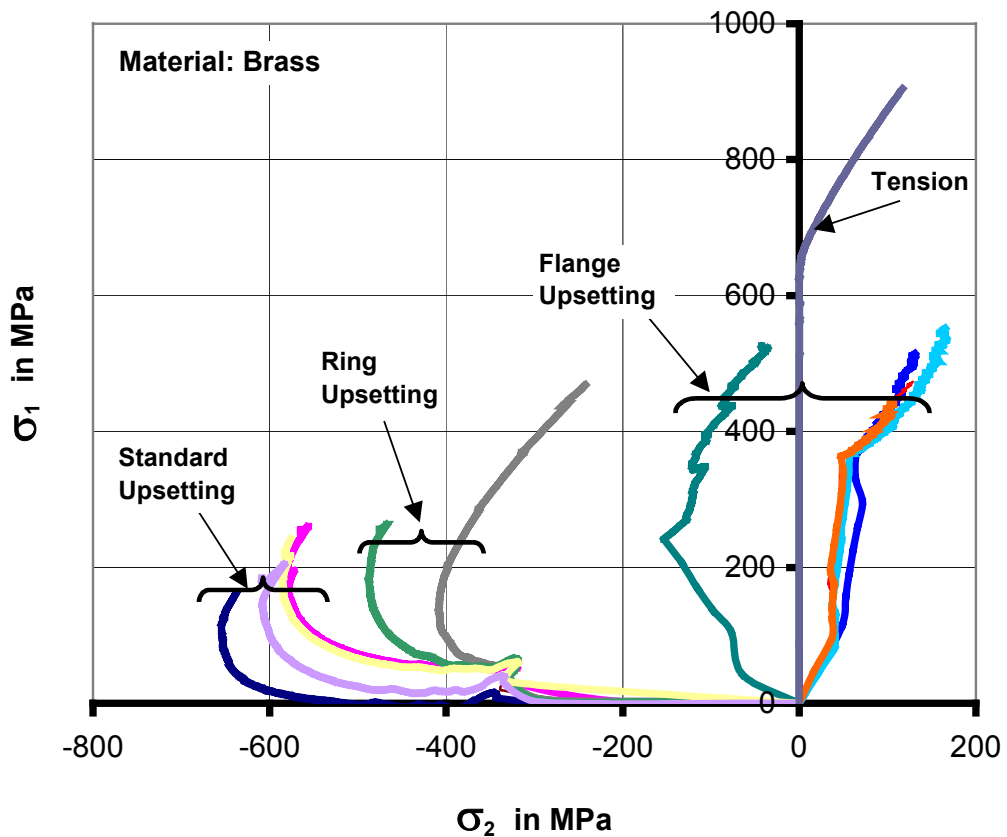


**Figure 5.17**  $\sigma_1$  vs.  $\sigma_2$  stress path for critical points (each curve represents a different specimen)

For the critical point (center point) of tension specimens,  $\sigma_2$  is the circumferential stress and  $\sigma_1$  is the axial stress, which is tensile.  $\sigma_2$  is zero until the necking starts.

In the case of flange compression,  $\sigma_2$  is compressive for one specimen, since the flange diameter is close to the contact surface diameter. For the other flanged specimens  $\sigma_2$  is never compressive, as the flange diameter is larger than the contact surface diameter and the compressive axial force applied to the specimen does not effect the flange region.

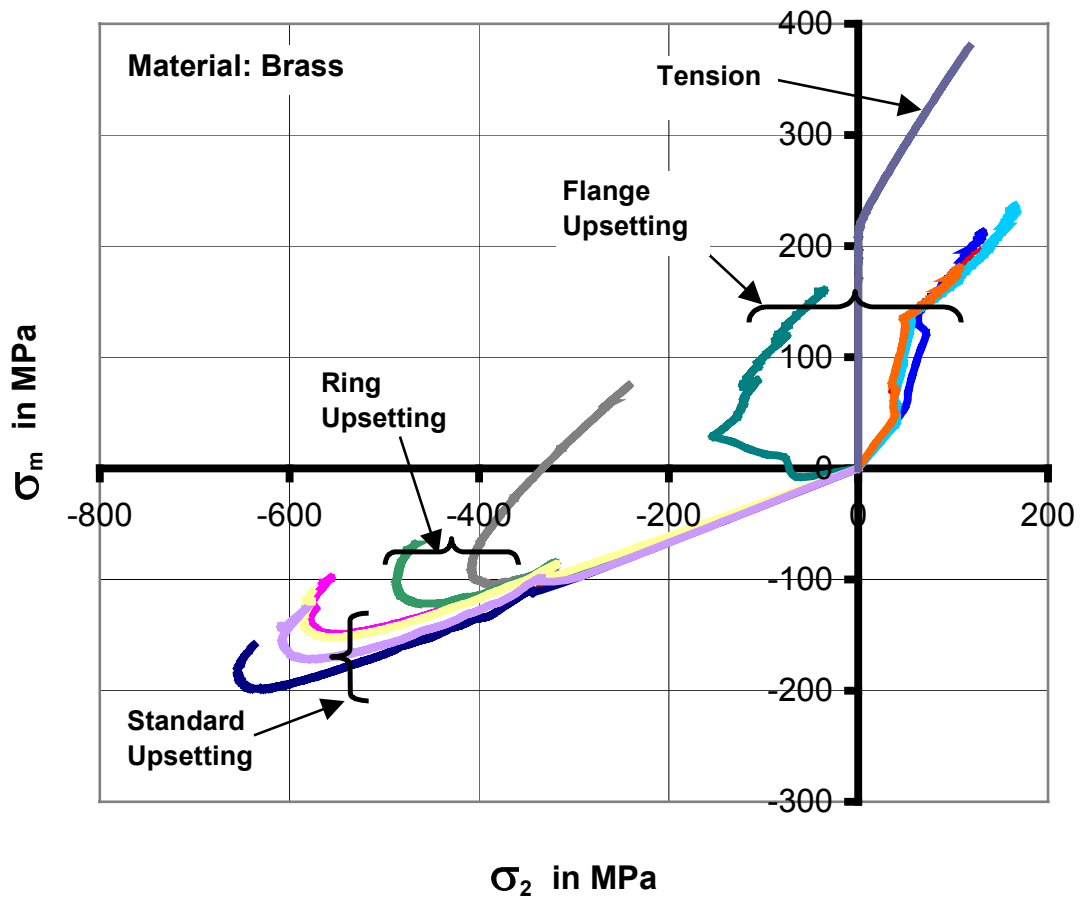


**Figure 5.18**  $\sigma_m$  vs.  $\sigma_2$  stress path for critical points (each curve represents a different specimen)

The paths of mean stress for the same specimens of Figure 5.16 are shown in Figure 5.18. Mean stress is always negative for brass standard compression specimens.

The standard compression and ring specimens have shear type of cracks, which make an angle of  $45^\circ$  to the symmetry axis.

The designations of the certain dimensions that will be used in shear stress analysis of Figure 5.20, 5.21, 5.22 are shown in Figure 5.19.

In Figure 5.19,  $h_f^*$  is the half (due to the symmetry plane used in simulations) of the final height of the cracked brass specimen and  $h^*$  is the height of the specimen at which the maximum shear stress is plotted radially in Figures 5.20, 5.21, 5.22. It is also shown in Figure 5.19 that  $r_f$  is the radius of the cracked specimen at the height of  $h^*$  and  $r$  is the variable in the direction of  $r_f$  ( $0 \leq r \leq r_f$ ) at which the maximum shear stress is plotted.

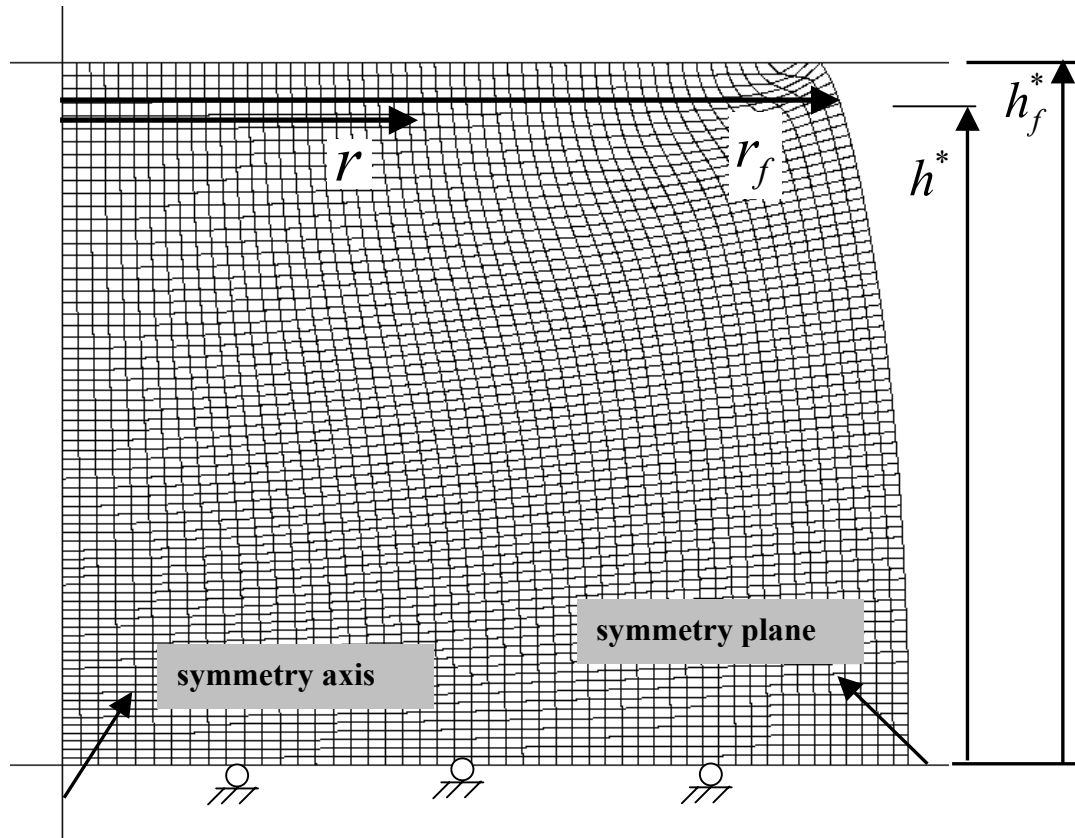


**Figure 5.19** Designations of certain dimensions to be used in Figures 5.20, 5.21, 5.22

Figures 5.20, 5.21, 5.22 show the radial change (from the symmetry axis to the free surface of the specimen) of maximum shear stress values for a standard compression, a ring and a flanged specimen, respectively. Different curves on these figures represent the radial distribution of maximum shear stress at different heights,  $h^*$ . The curves are selected close to the contact surface, where the maximum shear stress at this region is greater.

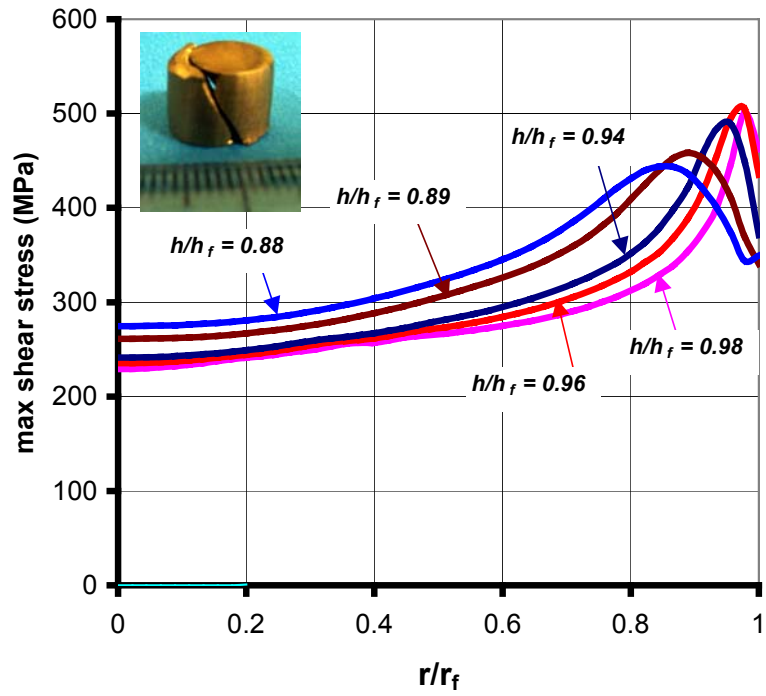


Figure 5.20 Maximum shear stress analysis for the 'standard compression 6' specimen

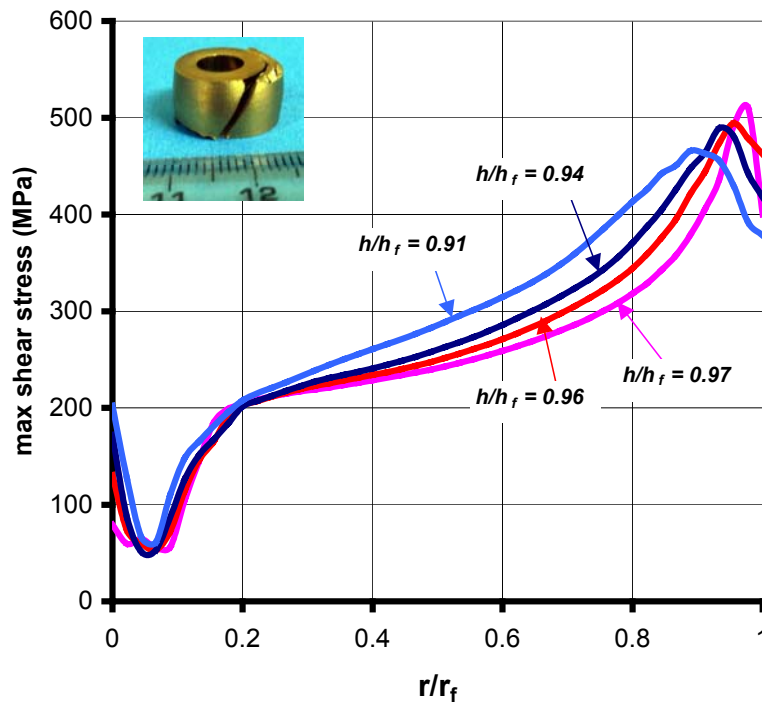
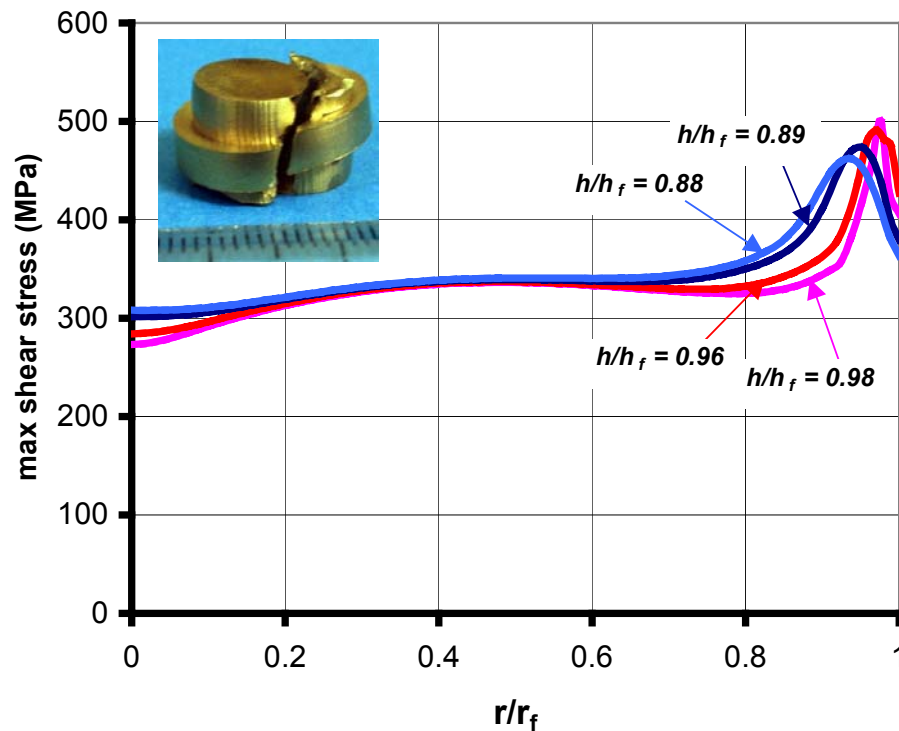


Figure 5.21 Maximum shear stress analysis for the 'Ring 3' specimen

The peak value of maximum shear stresses are shown very close to the contact region and it is approximately 500 MPa for standard, ring and flanged compression specimens.

On the other hand, when the peak values of individual curves is examined (at different  $h/h_f$ ), they make an angle similar to the cracking path of the specimens.



**Figure 5.22** Maximum shear stress analysis for the 'Flanged 5' specimen

## 5.5 Discussions and Conclusions

All of the criteria used in damage calculations detect the critical central point of tension test specimens correctly.

Ayada, Rice&Tracey and McClintock criteria calculate zero damage, since the mean stresses for the standard compression specimens stay negative at the critical point

during the compression and the integration results with zero damage value. This shows that they are not applicable for the damage detection of brass compression specimens.

For the remaining criteria, an average damage value of the cracked specimens is found and the percent deviation of the individual damage values of each specimen from the average damage value of the criterion is shown in Figures 5.13 and 5.14, for standard compression and flanged compression specimens, respectively. The deviations from the average value are too much, which means that the criteria do not calculate similar maximum values at the equatorial point of cracked specimens (Figure 3.26). In addition, these criteria are not capable of calculating maximum damage values at the true critical region of standard compression and ring compression specimens. The criticized points by these criteria do not appear on the 45<sup>0</sup>-cracking path of the standard compression and ring specimens.

The critical damage values for tension specimens (Table 5.7) are above those of compression specimens (Tables 5.8, 5.9, 5.10) for all criteria.

The Oyane criterion can also be used successfully for the processes where the primary stress is compressive.

Maximum shear stress is investigated in specimens having 45<sup>0</sup> shear type of cracks and the critical value of 500 MPa for the maximum shear stress is shown (Figures 5.20, 5.21, 5.22). Maximum shear stress exists on the cracking path of these specimens and they are near to the contact surface.

## **CHAPTER 6**

### **DISCUSSIONS AND CONCLUSIONS**

The aim of this study was to investigate the applicability of damage models to the cold forging of metals, by performing tension tests and various compression tests until cracks become visible. Materials bearing steel, stainless steel and brass are used in analysis.

After obtaining the tensile and compressive flow curves of material and the Coulomb friction coefficient between the material and the dies of the hydraulic press used in experiments, the failure experiments have been modeled by the commercial finite element analysis program Deform.

Several criteria, which had been implemented in Deform, have been used to calculate the corresponding damage values of cracked specimens. In FEM simulations, the points from which the critical (maximum) damage values are taken from must coincide with the experimentally cracked regions. Then the used criterion is said to be successful in correctly detecting the cracked region.

Since different geometries of specimens create different stress-strain paths in the material, the experiments have been conducted with cylindrical, flanged, ring and tapered geometries. Dimensions of specimens belonging to each geometry group are also different to increase variation. The critical damage values from FEM are tabulated for each geometry of a material.

The critical damage values of a criterion for different geometries are desired to be similar in order to say that this specific criterion is independent of geometric parameters. Therefore, such a criterion may cover different process parameters in detecting the crack initiation conditions successfully.

All of the criteria used in damage calculations detect the critical central point of tension test specimens correctly. This is generally the same in compression specimens. A few criteria have detected inner points to be the most critical for some compression specimens. These types of possible inner cracks could not be checked in this study, since complicated methods like non-destructive testing were necessary for checking the inner cracks.

Each material used in this study has the critical damage values for tension specimens that are above those of compression specimens for all criteria. This shows that it is not true to take the tension test fracture damage values as references for making comparisons with the damage values of compression specimens.

In the formability analysis of bearing steel 100Cr6 (Chapter 3), the cracks have been observed on the middle of free surfaces (on the equator) of the specimens and the experiments are modeled to obtain the damage values, represented in Tables 3.7, 3.8, 3.9 for standard compression, flanged and ring geometries, respectively.

When each table is examined separately, the critical values in each row (the critical values of a single criterion for different compression specimens) seem to be similar, except the criterion of Ayada, which supplies the greater variation. These similarities in damage values are not surprising, as the criteria are consistent in calculating similar damage values at critical regions of specimens having slightly different dimensions (similar stress paths). Nevertheless, this shows that the critical points, at which the maximum damage values are calculated in simulations, coincide with the region that the crack initiates.

When the Tables 3.7, 3.8, 3.9 and 3.10 are examined together, the critical values of a single criterion for standard, ring and flange compression specimens can be compared in Figure 6.1.

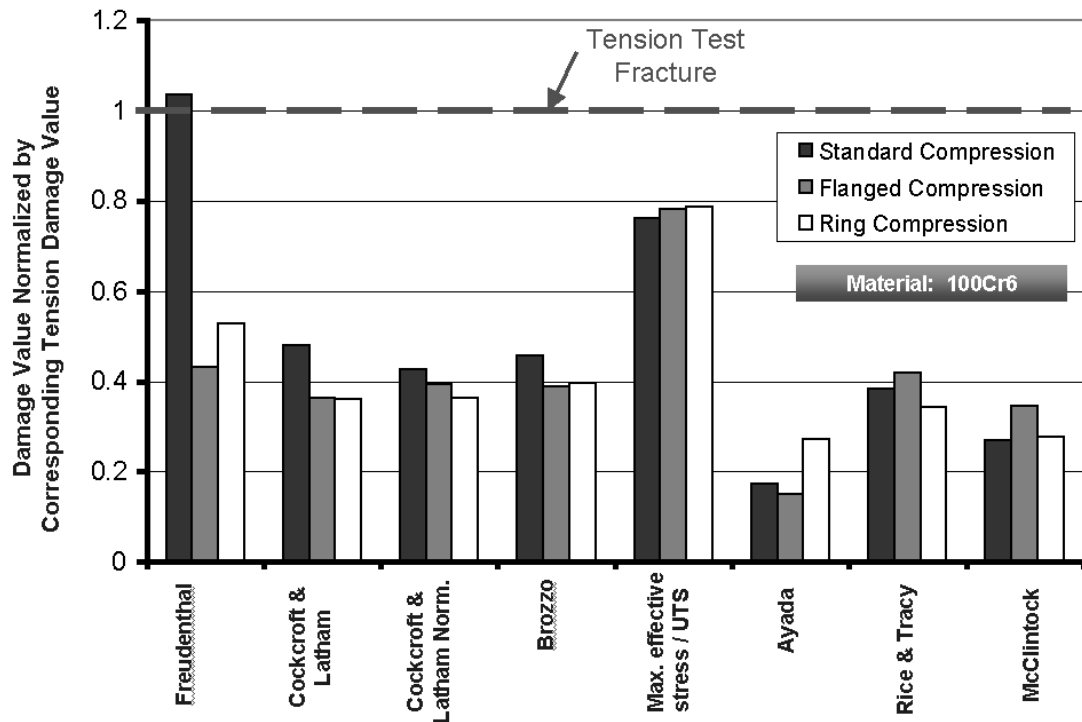


**Figure 6.1** Repeatability of damage values among specimens of different geometries

Since the order of magnitude of damage values from different criteria are different, the damage values are normalized by the corresponding tensile fracture damage value (Each damage value is divided by the tensile fracture damage value of the same criterion). Therefore it is also possible to make a comparison between compressive damages and tensile fracture damage in the same figure (Figure 6.1).

Damage values of three different compression geometries seem to be similar for most of the criteria, including the criteria of ‘maximum effective stress / UTS’, ‘Brozzo’, ‘C&L Normalized’ and ‘Rice&Tracy’. These criteria may be used successfully for various geometries of compression processes. As mentioned before, the tensile fracture damage values are above the compression damage values. The

tensile test critical damage values can still be used as a reference when investigating formability of processes in which the primary stress is tensile.

Critical values from different geometries are compared for each criteria and acceptable repeatability is found except criterion of Freudenthal (Figure 6.1). The average values of damages from different geometries are given in Table 6.1.

**Table 6.1** Average critical damage values of material 100Cr6

<b>Damage Criteria</b>	<b>Average Damage Value of Various Compression Geometries</b>
Cockroft&Latham (MPa)	420
C&L Normalized	0.47
Brozzo	0.49
Max.Effective stress/ UTS	1.73
Ayada	0.11
Rice&Tracey	0.45
McClintock	0.82

The Oyane criterion can also be used for the processes where the primary stress is compressive. The specimens may be accepted to be safe, when they stay below the trendline (Figure 3.30).

Stainless steel (X5CrNiMo1810) has the greatest strength and formability among the materials investigated in this study.

Since no cracks have been detected during the compression tests, it is difficult to comment on the success of a specific criterion in detecting correct critical points. The damage criteria may still be used to detect the locations of critical points and the possible upper bounds for safe damage values of each criterion. The specimen with similar loading conditions with the experiments can be assumed to have no cracks below these safe damage values.

For an industrial case study, a process from HILTI Corporation is used. FEM model using different failure criteria for the mentioned process are conducted and damage values are shown in Table 4.12. For stainless steel, the damage values of this cracked specimen can be used as a reference where the primary stress is compressive. Since the only cracked specimen is from the heading process, Figure 6.2 shows the comparison of critical damage values of heading process with the damage values of different geometries of 100Cr6 (Figure 6.1).

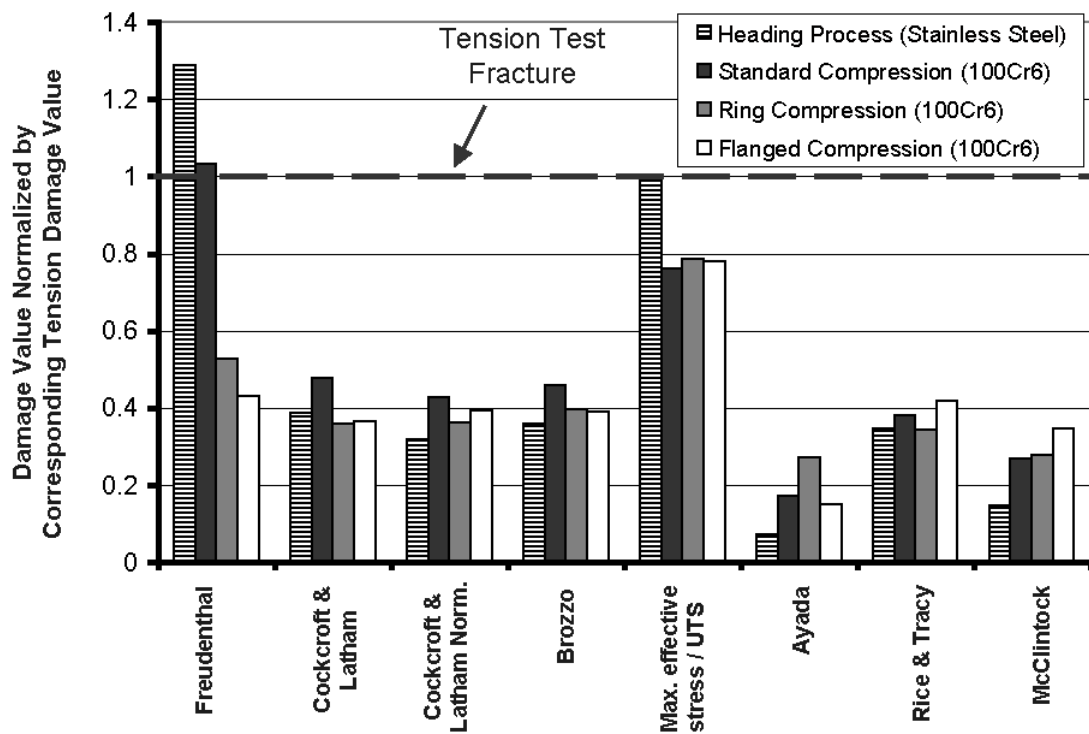


**Figure 6.2** Comparison between 100Cr6 and stainless steel critical damage values

Critical values of stainless steel heading process are compared with those of different geometries of 100Cr6 for each criteria and a similarity can be seen for the criteria of Cockcroft & Latham, Cockcroft & Latham Normalized, Brozzo and Rice Tracy (Figure 6.2).

The critical damage values of stainless steel from heading process are given in Table 6.2.

**Table 6.2** Critical damage values of stainless steel

Damage Criteria	Heading Process Damage Value
Cockroft & Latham (MPa)	405
C&L Normalized	0.38
Brozzo	0.42
Max.Effective stress/ UTS	2.21
Rice&Tracey	0.41
McClintock	0.40

The Oyane criterion could not have been used for stainless steel, since the cracked compression specimens are required to calculate the material constant of this criterion.

In the formability analysis of brass (Chapter 5), the cracks making approximately 45° angles with the symmetry axis have been observed for the standard and ring compression specimens.

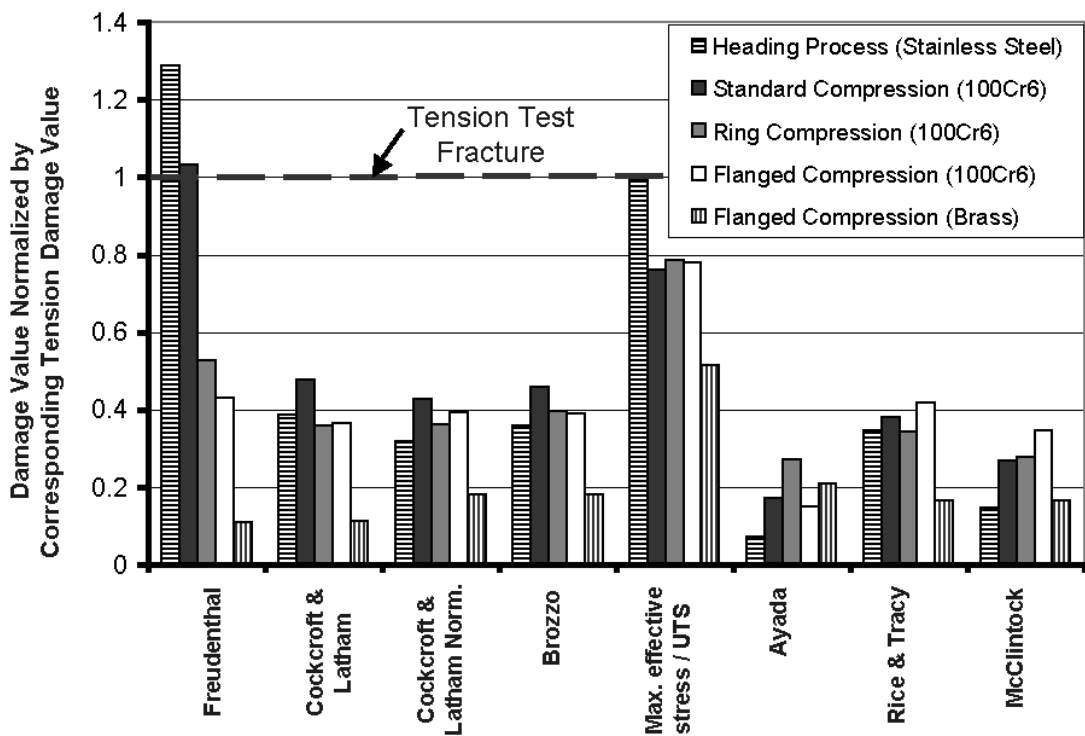


**Figure 6.3** Comparison between brass, 100Cr6 and stainless steel damage values

The flanged specimens are usually cracked at the flanged region and the crack type is similar to the cracks of material 100Cr6. Therefore, only flanged brass specimens are compared with damage values of other materials (Figure 6.3).

The damage values from flanged compression normalized by tension damage values are not in agreement with those of 100Cr6 and stainless steel (Figure 6.3). The reason may be the less ductile behavior of brass.

The critical damage values of brass for flanged compression specimens are given in Table 6.3.

**Table 6.3** Critical damage values of brass flanged specimens

Damage Criteria	Flanged Compression
Freudenthal (MPa)	36
Cockroft & Latham (MPa)	38.93
C&L Normalized	0.09
Brozzo	0.09
Max.Effective stress/ UTS	0.97
Ayada	0.04
Rice&Tracey	0.09
McClintock	0.18

Maximum shear stress analysis is shown to be successful for the crack type of brass. Maximum shear stress exists on the cracking path of these specimens and near to the contact surface. The critical value can be accepted as 500 MPa for the maximum shear stress.

The Oyane criterion can be used successfully for the processes where the primary stress is compressive for brass.

A general theoretical means of ductile fracture criteria cannot be suggested in this study. The critical damage values and suggested criteria differ according to the process and material used.

However, the damage criteria can be used safely in two different methods, as mentioned earlier:

1) For a process in which the material is known to fracture, or in analyzing a process where ductile fracture is known to be a risk, several alternatives can be analyzed. The alternative with the lowest critical damage value, obtained from a single or various fracture criteria, is the best alternative for minimizing the initiation of fracture.

2) Critical damage values, created by a process in a workpiece, can be estimated from prior experience with a given material on a part that is known to fracture. Analyzing a process known to cause cracking in the part will give an upper bound value. And analyzing a part made of the same material that is known not to crack will give a lower bound value. If the peak damage value from the analysis corresponds with the fracture point on the part, this will give a good estimate of the critical value. Designs with a damage value below this value (10% to 20% or more) should be safe from fracture, if material and annealing conditions are the same.

Geometrical modifications of the forming punches and dies should be examined, but also annealing operations or the use of alternative materials can be considered to extend the forming limit in the critical areas.

## **CHAPTER 7**

### **FURTHER RECOMMENDATIONS**

In this last chapter, further recommendations are suggested about the study.

The detections of possible inner cracks have not been checked in this study, since complicated methods like non-destructive testing were necessary for checking the inner cracks. The scope of analysis may be enlarged to take the inner cracks into account.

Since no cracks have been detected during the compression tests of stainless steel, processes causing cracks may be searched from the industry and used in damage analysis. As an example, in the case study represented in Section 4.4.3, a workpiece that was cracked during heading process was modeled to investigate damage.

The compression experiments have been conducted with cylindrical, flanged, ring and tapered geometries using flat dies. Other geometries of specimen and geometrical modifications of the forming punches and dies may be examined for compression in order to create greater damages. The geometry of the punch that is shown in Figure 7.1 may be an example to geometrical modifications, although the manufacturing of a punch may be difficult in the experimental study of such a modification.

The workpiece dimensions and geometry may also be changed. As an example, a hole in a flanged or tapered specimen can be introduced in order to decrease the punch load and increase the stroke capacity of the press used in experiments.

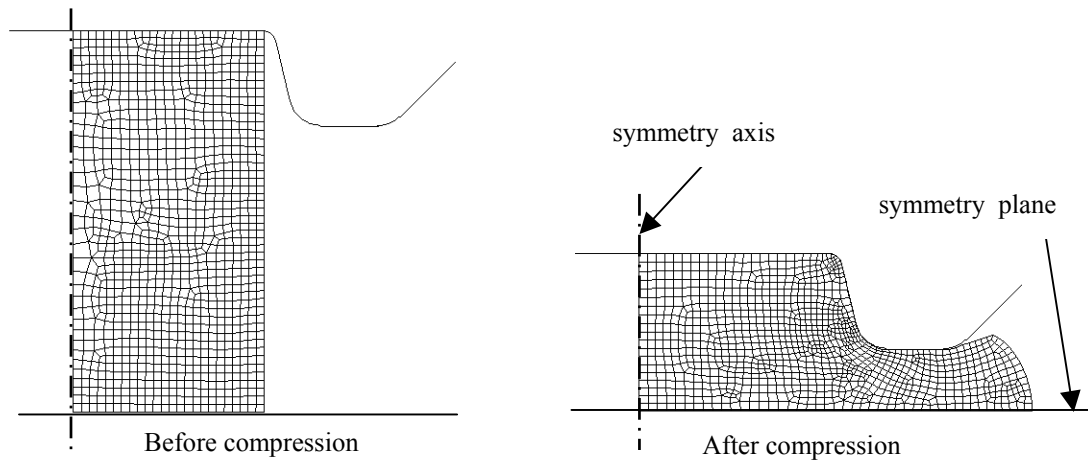


**Figure 7.1** An example for the geometry of punch that may increase damage  
(Deform 2D version 7.1)

The effect of temperature and strain rate on formability is not investigated in this study as the experiments are performed at room temperature (cold forming temperature for the used materials). The effect of temperature and strain rate may also be searched.

Metallurgical investigations like the grain size effect on formability may also be examined for these materials.

## REFERENCES

- Abdel-Rahman M., 1995, Determination of Workability Curves Using Two Mechanical Tests
- Arentoft M., Wanheim T. 1995, The Basis for a Design Support System to Prevent Defects in Forging
- Avitzur B., 1983, Handbook of Metal-Forming Processes, John Wiley & Sons
- Bethlehem, Prevention of Central Bursting in Cold Extrusions, Booklet 2913
- Behrens A., Just H., 2002, Verification of damage model of effective stresses in cold and warm forging operations by experimental testing and FE simulations, Journals of Material Processing Technology 125-126 (2002) 295-301
- Bridgman, P.W, 1944, The Stress Distribution at the Neck of a Tension Specimen, Transactions of American Society for Metals, Vol. 32, 1944, p. 553.
- Brooks C. R., Choudhury A., 1993, Failure Analysis of Engineering Materials, McGraw-Hill
- Cockcroft M.G., Latham D.J., 1968, Ductility and the Workability of Metals, Journal of the Institute of Metals
- DEFORM Users Manual, 2000, Scientific Forming Technologies Corporation, Version 7.1

Dodd B., Konieczny A.A., 1995, Limiting Phenomena in Cold Forging

Ettouney O., Hardt D.E., 1983, A method for In-Process Failure Prediction in Cold Upset Forging

Gardini C., Ceretti E., Maccarini G., 1995, Formability in Extrusion Forging: the Influence of Die Geometry and Friction Conditions, Journal of Materials Processing Technology, 54, pp. 302-308

Gouveia B.P.P.A., Rodrigues J.M.C., Martins P.A.F., 1998, Ductile fracture in metalworking: experimental and theoretical research

Ko D., Kim B., 1998, The Prediction of Central Burst Defects in Extrusion and Wire Drawing

Koçaker, B., 2003, Product Properties Prediction After Forming Process Sequence, METU, ANKARA

Lange K., 1985, Handbook of Metal Forming, McGraw-Hill

Lee E.H., McMeeking R.M., 1977, On a Theory of Central Burst or Chevroning Defect in Drawing and Extrusion

Lemiatre J., 1998, A Course on Damage Mechanics, Springer Verlag

Male A.T., Cockcroft M.G., 1965, A method for the determination of the coefficient of friction of metals under condition of bulk plastic deformation

N.N., Defects in Cold Forging, ICFG SUBGROUP, 1996, Final Report, Materials and Defects

Oh Hung-Kuk, 1998, A note on a proposed general criterion for brittle and ductile fracture in material and structures

Oyane M., Sato T., Okimoto K., Shima S., 1980, Criteria for Ductile Fracture and Their Applications, Journal of Mechanical Working Technology, 4, pp. 65-81

Park J.J., 1981, Internal Cracking in Symmetrically Opposed Extrusion, Annals of the CIRP, Vol. 30/1

Parteder E., Bünten R., 1998, Determination of Flow Curves by Means of a Compression Test under Sticking Friction Conditions Using an Iterative Finite-Element Procedure, Journal of Materials Processing Technology, 74 (1998), pp. 227-223.

Rice J.R., Tracey D.M., 1969, On the Ductile Enlargement of Voids in Triaxial Stress Fields, Journal of Mech. Phys. Solids, Vol.17, pp. 201-217

Shabara M.A., El-Domiaty A.A., Kandil A., 1996, Validity Assessment of Ductile Fracture Criteria in Cold Forming

Sofuoglu H., Rasty J., 1999, On the measurement of friction coefficient utilizing the ring compression test, Tribology International 32 (1999) 327–335

Sowerby R., Chandrasekaran N., Dung N.L., Mahrenholtz O., 1985, The Prediction of Damage Accumulation During Upsetting Tests Based on McClintock's Model

Takuda H., Mori K., Hatta N., 1998, The Application of Some Criteria for Ductile Fracture to the Prediction of the Forming Limit of Sheet Metals

## APPENDIX A

**Table A.1** Cockcroft & Latham damage values and maximum punch force at the simulated compressions (to final height of 2mm) of stainless steel tapered specimens at various initial dimensions (Deform 2D version 7.1)

Dimensions of specimen of Figure A.1 in mm					Coulomb friction factor	compression to $L_{final}=2$ mm	
$L$	$R_i$	$R_o$	$R_{hole}$	$t$		Cockcroft & Latham damage	maximum punch force (tons)
15	3	5	0	2	0.05	725.62	76.94
15	4	5	0	2	0.05	806.39	99.9
15	5	5	0	2	0.05	578.59	118.95
15	3	5	0	2	0.2	769.15	139.6
15	4	5	0	2	0.2	845.37	183.4
15	5	5	0	2	0.2	879.36	249.59
15	3	5	0	2	0.3	784.41	165.16
15	4	5	0	2	0.3	848.91	200.28
15	5	5	0	2	0.3	890.76	275.73
15	3	5	1	2	0.05	709.09	73.77
15	4	5	1	2	0.05	765.16	91.67
15	5	5	1	2	0.05	575.77	111.74
15	3	5	1	2	0.2	738.82	128.91
15	4	5	1	2	0.2	822.32	173.99
15	5	5	1	2	0.2	840.17	232.04
15	3	5	1	2	0.3	750.09	149.89
15	4	5	1	2	0.3	833.34	202.3
15	5	5	1	2	0.3	826	234.5
15	3	5	2	2	0.05	622.04	58.64
15	4	5	2	2	0.05	720.15	76.84
15	5	5	2	2	0.05	664.88	99.39
15	3	5	2	2	0.2	634.45	94.29
15	4	5	2	2	0.2	745.63	139.9
15	5	5	2	2	0.2	825.48	191.93
15	3	5	2	2	0.3	629.5	109.45
15	4	5	2	2	0.3	753.26	162.77
15	5	5	2	2	0.3	804	213.3

**Table A.2** Brozzo damage values and maximum punch force at the simulated compressions (to final height of 2mm) of stainless steel tapered specimens at various initial dimensions (Deform 2D version 7.1)

Dimensions of specimen of Figure A.1 in mm					Coulomb friction factor	compression to $L_{final}=2$ mm	
$L$	$R_i$	$R_o$	$R_{hole}$	$t$		Brozzo damage	maximum punch force (tons)
15	3	5	0	2	0.05	0.8062	77.5
15	4	5	0	2	0.05	0.8188	99.1
15	5	5	0	2	0.05	0.5862	129.2
15	3	5	0	2	0.2	0.8573	139.7
15	4	5	0	2	0.2	0.8816	185.71
15	5	5	0	2	0.2	0.8447	249.5
15	3	5	0	2	0.3	0.8733	165.24
15	4	5	0	2	0.3	0.9045	218.66
15	5	5	0	2	0.3	0.8608	275.7
15	3	5	1	2	0.05	0.7931	73.6
15	4	5	1	2	0.05	0.8049	91.67
15	5	5	1	2	0.05	0.5703	110.87
15	3	5	1	2	0.2	0.831	128.9
15	4	5	1	2	0.2	0.8627	170.07
15	5	5	1	2	0.2	0.8181	233.2
15	3	5	1	2	0.3	0.8471	150.03
15	4	5	1	2	0.3	0.8734	202.94
15	3	5	2	2	0.05	0.7217	57.4
15	4	5	2	2	0.05	0.7772	76.84
15	5	5	2	2	0.05	0.6574	98.2
15	3	5	2	2	0.2	0.7335	92.67
15	4	5	2	2	0.2	0.8043	135.4
15	5	5	2	2	0.2	0.8013	191.44
15	3	5	2	2	0.3	0.739	108.7
15	4	5	2	2	0.3	0.8196	162.78
15	5	5	2	2	0.3	0.8236	234.16

**Table A.3** Freudenthal damage values and maximum punch force at the simulated compressions (to final height of 2mm) of stainless steel tapered specimens at various initial dimensions (Deform 2D version 7.1)

Dimensions of specimen of A.1 in mm					Figure	compression to L=2 mm	
$L$	$R_i$	$R_o$	$R_{hole}$	$t$	Coulomb friction factor	Freudenthal damage	maximum punch force (tons)
15	3	5	0	2	0.05	773.18	76.94
15	4	5	0	2	0.05	979.58	99.9
15	5	5	0	2	0.05	1485.6	118.95
15	3	5	0	2	0.2	774.6	139.6
15	4	5	0	2	0.2	929.04	183.4
15	5	5	0	2	0.2	1164.9	249.59
15	3	5	0	2	0.3	781.2	165.16
15	4	5	0	2	0.3	928.78	200.28
15	5	5	0	2	0.3	1148	275.73
15	3	5	1	2	0.05	741.29	73.77
15	4	5	1	2	0.05	911.06	91.67
15	5	5	1	2	0.05	1416.7	111.74
15	3	5	1	2	0.2	740.62	128.91
15	4	5	1	2	0.2	892.49	173.99
15	5	5	1	2	0.2	1111.8	232.04
15	3	5	1	2	0.3	744.18	149.89
15	4	5	1	2	0.3	889.8	202.3
15	5	5	1	2	0.3	915	234.5
15	3	5	2	2	0.05	655.65	58.64
15	4	5	2	2	0.05	803.09	76.84
15	5	5	2	2	0.05	1162	99.39
15	3	5	2	2	0.2	646.76	94.29
15	4	5	2	2	0.2	796.28	139.9
15	5	5	2	2	0.2	981.65	191.93
15	3	5	2	2	0.3	642.42	109.45
15	4	5	2	2	0.3	799.06	162.77
15	5	5	2	2	0.3	774	213.3

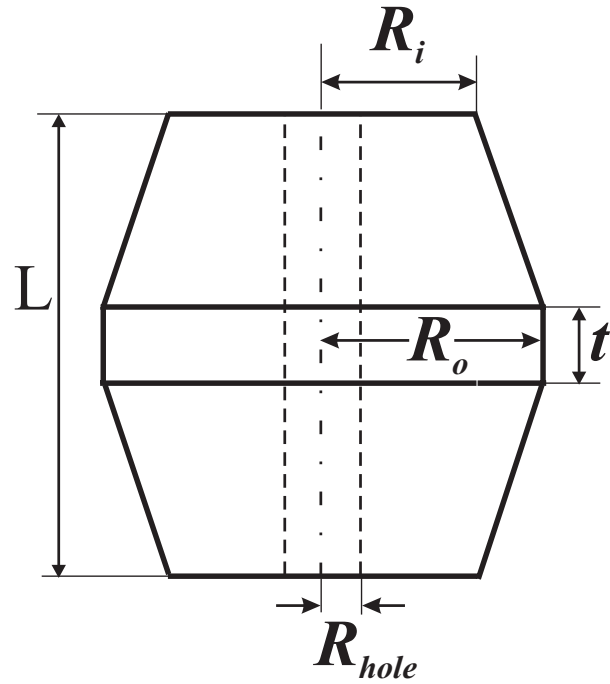


**Figure A.1** Designations of tapered specimen used in the parameter study represented in Tables A.1, A.2, A.3